Modelling the marine biogeochemical implications of aeolian, sedimentary and riverine iron supply

Dissertation
zur Erlangung des Doktorgrades
der Mathematisch-Naturwissenschaftlichen Fakultät
der Christian-Albrechts-Universität
zu Kiel

vorgelegt von
Levin Nickelsen

Kiel
2015

Erster Gutachter:	Prof. Dr. Andreas Oschlies
Zweiter Gutachter:	Prof. Dr. Klaus Wallmann
Tag der mündlichen Prüfung:	03.06.2015
Zum Druck genehmigt:	03.06.2015

gez. Prof. Dr. Wolfgang J. Duschl, Dekan

Contents

Summary

Iron is an important nutrient for marine phytoplankton and low concentrations of iron limit phytoplankton growth in around 40% of the surface area of the ocean. Due to the low solubility of iron in the sea, the concentrations of iron are largely dependent on external sources such as atmospheric deposition of iron-containing dust derived from arid areas on land. However, also release of iron from the sediment and the supply of iron from rivers are important external sources of iron to the ocean. In this thesis the role of these external sources in influencing marine biogeochemistry is studied.

In a first step, an existing ocean biogeochemical model is used to study the sensitivity of oceanic CO_2 uptake to dust deposition. The so-called iron hypothesis suggests that enhanced atmospheric dust deposition to the Southern Ocean during the Last Glacial Maximum around 20,000 years decreased atmospheric CO_2 concentrations by increasing phytoplankton growth and export of organically bound carbon to the deep ocean. The first part of the thesis shows that the sensitivity of organic matter export and oceanic CO_2 uptake to dust deposition is increased significantly if the impact of iron bioavailability on light harvesting capabilities is explicitly considered. These results also indicate that there is still uncertainty in the biogeochemical response to dust deposition.

In the second part of the thesis, a model of the oceanic iron cycle is developed and implemented in the University of Victoria Earth System Climate Model (UVic). This implementation allows iron cycling sensitivity studies in the framework of an earth system model of intermediate complexity. The results show that a precise description of the depth of the sedimentary iron release is necessary to simulate the iron supply from the sediment to the euphotic zone. Scaling the sedimentary iron release with temperature leads to a better agreement of simulated iron concentrations with observations, indicating a possible influence of temperature on the sediment release on the global scale. A test simulation regarding the atmospheric dust deposition shows that neglecting the variability in the solubility of iron in atmospheric dust does not significantly alter iron limitation patterns. However, the assumed global concentration of iron-binding ligands regulates the response to changes in sedimentary release of iron and dust deposition strongly and thus reveals a further major uncertainty in the interaction of the iron cycle with ocean biogeochemistry.

In the third part of this thesis, literature data on benthic dissolved iron fluxes, bottom water oxygen concentrations and sedimentary carbon oxidation rates are assembled. The data are analyzed with a diagenetic iron model to derive an empirical transfer function

for predicting benthic iron fluxes in dependence on oxygen concentrations and carbon oxidation rates. Employing the empirical function to the UVic-model from the previous chapter leads to a factor of two higher globally averaged iron concentrations in surface waters. Iron fluxes from the sediment could therefore be much larger than previously thought.

In the fourth part of this thesis, the empirical transfer function developed in the previous chapter is further tested in the UVic-model. The results show that a riverine supply of iron is necessary as a source of reactive iron to the sediment to balance the release of dissolved iron from the sediment on a global scale. A sensitivity test reveals that export production and oxygen concentrations are highly sensitive to the riverine iron source. This strong sensitivity could play an important role in determining primary production and the extent of low oxygen waters under climate change.

Overall, this thesis emphasizes the importance of the external sources of iron to the ocean. Dust deposition, sedimentary iron release and riverine iron supply strongly control the dissolved iron concentrations in the ocean. Changes in these external sources can have strong implications for marine biogeochemistry and oceanic CO_2 uptake.

Zusammenfassung

Eisen ist ein wichtiger Nährstoff für Phytoplankton. Niedrige Eisenkonzentrationen begrenzen das Wachstum von Phytoplankton in etwa 40% der Oberfläche des Ozeans. Aufgrund der geringen Löslichkeit von Eisen im Meer ist die Konzentration von Eisen weitgehend von externen Quellen abhängig. Eine dieser Quellen ist beispielsweise die atmosphärische Deposition von eisenhaltigem Staub, der aus ariden Gebieten an Land stammt. Aber auch die Eisenfreisetzung aus dem Sediment des Ozeans und der Eintrag von Eisen aus Flüssen in den Ozean sind wichtige externe Eisenquellen für den Ozean. In der vorliegenden Arbeit wird die Rolle dieser externen Quellen von Eisen und deren Wechselwirkung mit der marinen Biogeochemie untersucht.

In einem ersten Schritt wird ein bestehendes biogeochemisches Ozeanmodell verwendet, um die Sensitivität der ozeanischen CO_2-Aufnahme auf Staubablagerungen zu studieren. Die so genannte *iron hypothesis* sagt aus, dass erhöhte atmosphärische Staubablagerung in den Südlichen Ozean während des letzten glazialen Maximums vor rund 20.000 Jahren zu einem verstärktem Wachstum von Phytoplankton und Export von organisch gebundenem Kohlenstoff in die Tiefsee führte. Dadurch sei der atmosphärische CO_2-Gehalt verringert worden. Die Ergebnisse des ersten Teils der Arbeit zeigen, dass die Sensitivität des Exports von organischem Material in die Tiefsee und auch der ozeanischen CO_2-Aufnahme bezüglich des atmosphärischen Staubeintrags deutlich erhöht wird, wenn die Auswirkungen der Bioverfügbarkeit von Eisen auf Lichtsammelfähigkeiten explizit berücksichtigt werden. Diese Ergebnisse zeigen damit auch, dass es noch viele Unsicherheiten in der biogeochemischen Reaktion auf veränderte Staubeinträge gibt.

Im zweiten Teil der Arbeit wird ein Modell des ozeanischen Eisenkreislaufs entwickelt und in das *University of Victoria Earth System Climate Model* (UVic) implementiert. Dies ermöglicht die Durchführung von Sensitivitätsstudien bezüglich des Eisenkreislaufs im Rahmen eines Erdsystem-Modells mittlerer Komplexität. Die Ergebnisse zeigen, dass eine genaue Beschreibung der Tiefe der Freisetzung von Eisen aus dem Sediment notwendig ist, um die Zufuhr von Eisen aus dem Sediment in die euphotische Zone zu simulieren. Eine Skalierung des Eisenflusses aus dem Sediment mit der Wassertemperatur führt zu einer besseren Übereinstimmung zwischen simulierten Eisenkonzentrationen und Beobachtungen, was auf einen möglichen Einfluss der Temperatur auf den sedimentären Eisenfluss auf globaler Ebene hinweist. Eine Testsimulation in Bezug auf den atmosphärischen Eiseneintrag zeigt, dass sich die Verteilung der eisenlimitierten Areale im Ozean kaum verändert, wenn man im Modell berücksichtigt, dass die Löslichkeit von Eisen im at-

mosphärischen Staub stark variiert. Allerdings beeinflusst die globale Konzentration von Liganden, die Eisen gelöst halten, stark die simulierten Reaktionen der Ozeanbiogeochemie auf Veränderungen im Sedimentfluss und Staubeintrag von Eisen und zeigt damit eine weitere Unsicherheit in der Wechselwirkung des Eisenkreislaufs mit der Ozeanbiogeochemie auf.

Im dritten Teil dieser Arbeit werden Daten über benthische Eisenflüsse, Bodenwasser-Sauerstoffkonzentrationen und sedimentäre Kohlenstoff-Oxidationsraten zusammengestellt. Diese Daten werden mit einem diagenetischen Eisenmodell analysiert, um eine empirische Transferfunktion für die Beschreibung von benthischen Eisenflüssen in Abhängigkeit von Sauerstoffkonzentrationen und Kohlenstoff-Oxidationsraten abzuleiten. Die Verwendung der empirischen Funktion in der Konfiguration des UVic-Modells aus dem vorigen Abschnitt führt zu einer um den Faktor zwei höheren global gemittelte Eisenkonzentration im Oberflächenwasser. Eisenflüsse aus dem Sediment könnten somit viel größer sein als zuvor angenommen.

Im vierten Teil der Arbeit wird die empirische Übertragungsfunktion aus dem vorherigen Kapitel weiter im UVic-Modell getestet. Die Ergebnisse zeigen, dass ein Flusseintrag von Eisen notwendig ist, um reaktives Eisen in das Sediment einzutragen und die Freisetzung von gelöstem Eisen aus dem Sediment auf globaler Ebene auszugleichen. Eine Sensitivitätsstudie zeigt eine starke Sensitivität der Exportproduktion und von Sauerstoffkonzentrationen zu der Größe des Flusseintrags von Eisen. Diese starke Sensitivität könnte beispielsweise während des Klimwandels eine wichtige Rolle für die Primärproduktion und die Ausbreitung von Ozeanwassern mit niedrigen Sauerstoffkonzentrationen spielen.

Diese Arbeit unterstreicht die Bedeutung der externen Quellen von Eisen für den Ozean. Staubeintrag, sedimentärer Eisenfluss und Flusseinträge steuern auf starke Weise den gelösten Eisengehalt im Meer. Änderungen in diesen externen Quellen können starke Auswirkungen auf die marine Biogeochemie und die ozeanische CO_2-Aufnahme haben.

1 Introduction

1.1 Motivation and objectives

The Earth's climate affects the circumstances humans live in via temperature, precipitation patterns and sea level. The emission of CO_2 to the atmosphere from fossil fuel burning and changes to the land surface such as deforestation induce an anthropogenically caused climate change (IPCC, 2013). In contrast, during past glacial-interglacial cycles, atmospheric CO_2 levels and climate varied naturally. When the atmospheric CO_2 concentration changes, the CO_2 concentration in the ocean adjusts via a flux of CO_2 between the atmosphere and the ocean surface. In the euphotic zone of the ocean, a part of the CO_2 is taken up by photosynthesizing organisms (phytoplankton), thereby decreasing the CO_2 concentration in the surface ocean. In fact, the primary production of marine phytoplankton makes up for 56 Pg C yr^{-1}, which equals roughly half of the total primary production on earth (Buitenhuis et al., 2013). If the biomass is transported away from the surface to the deep ocean, the CO_2 is stored in the ocean for longer times. This increases the flux of CO_2 from the atmosphere to the ocean. However, the rate of photosynthesis and thus CO_2 uptake by phytoplankton is limited by the availability of nutrients (Moore et al., 2013). One of these nutrients is dissolved iron in seawater and iron limits phytoplankton growth in around 40% of the surface area of the ocean (Moore et al., 2001). It is therefore important to understand the controls of the marine iron cycle and its interaction with climate.

Around 25 years ago, Martin and Fitzwater (1988) proposed a hypothesis stating that phytoplankton growth in the Southern Ocean is widely limited by iron availability, today known as the *iron hypothesis*. The low deposition of iron containing dust that is eroded from arid areas on land to the Southern Ocean is suggested to be the main reason for the low iron concentrations. Furthermore, Martin (1990) states that enhanced atmospheric dust deposition to the Southern Ocean during the Last Glacial Maximum around 20,000 years ago triggered additional export of organically bound carbon to the deep ocean and contributed to the decrease in atmospheric CO_2 concentrations at that time. Indeed, analyses of ice and sediment cores show a good correlation between dust deposition and atmospheric CO_2 concentration. Although this does not proof a causal link, it suggests that dust deposition is coupled intimately to climate (Petit et al., 1999; Martínez-Garcia et al., 2011). In addition to the coupling between iron and climate, iron has also been shown to limit the growth of nitrogen fixing organisms, so-called diazotrophs (Mills et al., 2004). Unlike other phytoplankton, diazotrophs are able to use gaseous N_2 with atmo-

spheric origin as a nutrient and are capable of growing in waters that are low in dissolved nitrate and ammonium. Nitrogen is also an important nutrient for phytoplankton and its supply to the ocean is thus also influenced by the concentrations of iron in the ocean. This demonstrates that iron is an important part in ocean biogeochemistry.

Although the iron cycle has been researched intensively during the past decades, many questions remain unanswered today (Boyd and Ellwood, 2010). One of the most fundamental questions is the role of external sources of iron in regulating iron concentrations in the ocean (Tagliabue et al., 2014a). Dust that is eroded from land contains iron, is transported in the atmosphere by winds and is partly deposited to the ocean. While atmospheric iron deposition has been identified very early as an important source of iron to the surface of the open ocean, sediment release of iron was first believed to be of importance for coastal regions only. However, it is now becoming more and more clear that sediment release of iron reaches the open ocean as well (Elrod et al., 2004; Moore and Braucher, 2008). Scavenging reduces the concentration of bioavailable iron supplied by atmospheric deposition or sediment release. Scavenged iron is no longer available for phytoplankton as a nutrient and also prone to sinking into the deep ocean. With scavenging as an additional loss process the concentration of dissolved iron in the surface ocean is more dependent on external supplies, as compared to other nutrients. Once entering the ocean, dissolved iron stays in the ocean on average 15-200 years (Boyd and Ellwood, 2010) and a change in dust deposition or sediment release can thus have a strong impact on primary production, e.g. Tagliabue et al. (2014a). This shows the potential strong leverage that changes in external sources of iron to the ocean can have. This work addresses this issue with the following questions:

1. What is the response of the phytoplankton CO_2 uptake to changes in dust deposition? How does the response change when a dependence of phytoplankton light harvesting on iron availability is present? (Chapter 1)
2. How can the iron cycle be implemented in the ocean component of a global climate model of intermediate complexity? (Chapter 2)
3. What is an efficient parameterization of benthic iron release in global ocean biogeochemical models? (Chapter 3)
4. How does a better constrained sediment source of iron inform the global iron cycle? What is the role of the riverine iron source in supplying reactive iron to the sediment? (Chapter 4)

Before addressing these questions, I will introduce more general aspects of high-nutrient low-chlorophyll regions, the biological pump, the role of iron in glacial-interglacial cycles and the iron cycle and its interaction with marine biogeochemistry.

1.2 The Biological Pump

The motivation to study the iron cycle is largely based on the potential impact of the oceanic iron cycle on the Earth's climate via the so-called biological pump. The biological pump is one way dissolved CO_2 in the surface ocean can be transferred to the deep ocean. The first step of the biological pump is the photosynthetic fixation of dissolved CO_2 and its incorporation in the biomass of primary producers in the euphotic zone (Fig. 1.1). When these organisms die, are grazed or lyzed, a fraction remains as particulate organic matter that aggregates and sinks in the water column (Honjo et al., 2008). Some of the carbon is released again as CO_2 from the particles during remineralization of the organic matter by bacteria and zooplankton. A part of the remineralization takes place in deeper waters that are not in exchange with the atmosphere until they are upwelled to the surface again (DeVries et al., 2012). Only a small fraction of the organic matter sinks to sediment and even a smaller fraction is buried there. The net effect of a strong biological pump is a lowered atmospheric CO_2 concentration and storage of the CO_2 in the deep ocean where it does not influence the climate (Sarmiento and Orr, 1991; Falkowski et al., 1998). However, the transfer of carbon from the atmosphere to the deep ocean by the biological pump is limited by the availability of nutrients (e.g. iron) to phytoplankton in the surface ocean. For example in the Southern Ocean, macronutrients such as phosphate and nitrate are available in high concentrations but the low availability of the micronutrient iron limits the biological transfer of CO_2 to the deeper ocean (Boyd et al., 2000). According to

A second important process for the transfer of CO_2 from the atmosphere to the ocean is called the solubility pump, which is, however, not connected to the iron cycle and thus only briefly mentioned here. At cold water temperatures as in the high latitude ocean, the solubility of CO_2 in seawater is high and gas-exchange leads to the saturation of the cold surface waters with CO_2. In regions of deep or bottom water formation such as in the North Atlantic or Southern Ocean, the CO_2 rich waters are physically subducted into the deep ocean and in this way the CO_2 is prevented from influencing the climate (Sarmiento and Gruber, 2006).

1.3 The abundance of iron

1.3.1 Historical development

The concentrations of iron changed dramatically when around 2.5 billion years ago the oxygen levels on earth started to increase due to the establishment of photosynthesizing organisms that produced oxygen as a waste product on Earth (Barber, 2008). Since iron was readily available at that time and can have multiple electrical potentials, organisms

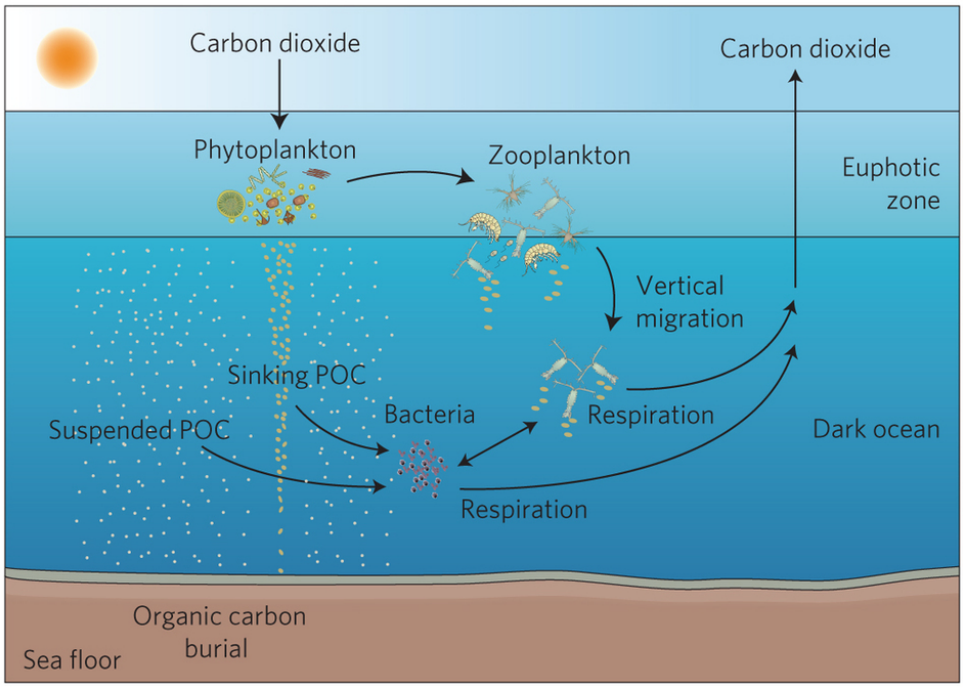

Figure 1.1: Schematic view on the biological pump illustrating the role of phytoplankton, zooplankton and bacteria (from Herndl and Reinthaler (2013)). Particulate organic carbon is denoted by POC.

had based their physiology strongly on iron and incorporated it into electron transport systems of photosynthesis and in essential enzymes (Behrenfeld and Milligan, 2013). However, the rising oxygen concentrations had negative consequences for the availability of iron in the ocean. Iron is present in two oxidative states in seawater, ferric iron (Fe(II)) and ferrous iron (Fe(III)). While Fe(II) is easy soluble in water and readily available for phytoplankton, Fe(III) is not very soluble. At the presence of oxygen, Fe(II) is rapidly oxidized to Fe(III) which then quickly precipitates, coagulates and adsorbs to particles (Rose and Waite, 2003). The result is that dissolved and thus bioavailable iron concentrations are reduced strongly at oxygen concentrations that organisms experience today. It is assumed that the reduced availability of iron lead to iron limitation in large areas of the ocean, i.e. the High-Nutrient Low-Chlorophyll (HNLC) regions described in the next section.

1.3.2 High-Nutrient Low-Chlorophyll (HNLC) regions

HNLC regions are a phenomenon that scientists struggled to explain until the discovery of widespread iron limitation in these regions (Raiswell and Canfield, 2012). Low concentrations of phytoplankton (chlorophyll) seemed to be in a logical conflict with high concentrations of the nutrients nitrate and phosphate that should allow phytoplankton to grow. Before the wide-spread iron limitation was discovered, strong grazing and light

limitation were discussed as possible reasons for the HNLC phenomenon, which was found in the Southern Ocean (Boyd et al., 2000), equatorial Pacific (Martin et al., 1994) and North Pacific (Tsuda et al., 2003). The area around the Kerguelen Plateau in the Southern Ocean is naturally iron fertilized because of iron release from sediments close to the ocean surface. The Kerguelen Plateau is an ideal place to study the marine biogeochemistry under iron limiting and iron replete conditions (Blain et al., 2007). In addition to studies at the Kerguelen Plateau, numerous artificial iron fertilization experiments were conducted, both, in shipboard bottle incubations and by directly fertilizing the ocean surface. In almost all experiments phytoplankton chlorophyll and macronutrient uptake increased significantly after the addition of iron to surface waters (de Baar et al., 2005; Boyd et al., 2007). However, the fate of the added iron is not very clear as in some experiments multiple iron additions were necessary to increase the surface iron concentrations and to stimulate phytoplankton growth (Bowie et al., 2001). Bowie et al. (2001) suggest that horizontal dispersion and scavenging strongly are likely to be responsible for the rapid loss of the fertilized iron. It was also rarely measured during the fertilization experiment to what quantity the organic matter, which was build up by phytoplankton in response to the iron fertilization, sinks in the water column and exports carbon to the deep ocean (de Baar et al., 2005; Aumont and Bopp, 2006). While, strong grazing and colimitation of iron with other nutrients and light are also still discussed to contribute to the limited growth of phytoplankton in the HNLC regions, it is widely accepted today that iron limitation is the main reason for the HNLC phenomenon (Moore and Doney, 2007; Breitbarth et al., 2010).

1.3.3 Modern global distribution

In the late 1980s trace metal clean bottles and highly sensitive analysis methods drastically improved the accuracy of measurements of iron concentrations in the ocean (e.g. Martin and Fitzwater (1988)). Different chemical forms of iron are operationally defined by the different pore filter sizes used during iron concentration measurements. Soluble iron is defined to be smaller than 0.02 µm, colloidal iron to have a size between 0.02 and 0.4 µm, and particulate iron is defined to be larger than 0.4 µm (Wu et al., 2001). Dissolved iron comprises soluble and colloidal iron and is usually assumed to be available for phytoplankton. However, some measurements of dissolved iron also use a pore filter size of 0.2 µm and thus do not include the whole fraction of colloidal iron, which complicates the interpretation of observations (Raiswell and Canfield, 2012). A compilation of dissolved iron observations by Tagliabue et al. (2012) shows that the number of measurements is still low as there are large areas of the ocean that remain completely unsampled (Fig. 1.2a). However, the observations at the ocean surface clearly show low

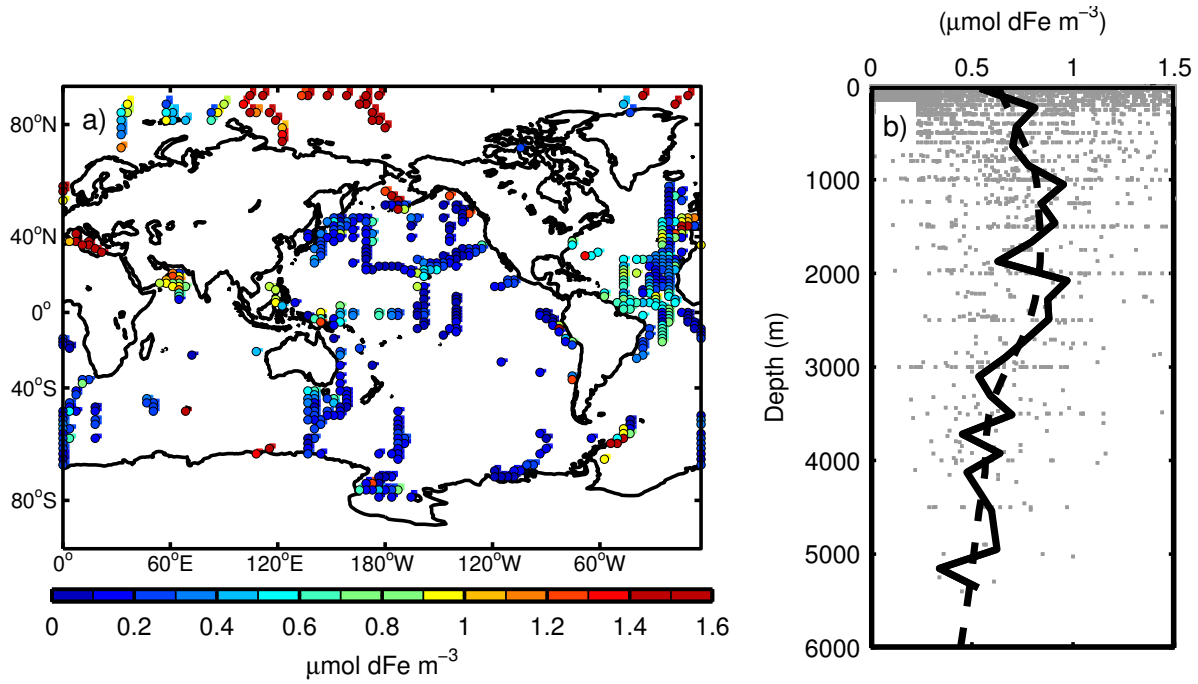

Figure 1.2: Observed iron concentrations: Surface iron concentrations averaged over the top 50 m and binned in 3.6°x1.8° boxes from the observation compilation by Tagliabue et al. (2012) are shown in **a)**. All observations plotted versus depth (gray dots) with horizontally averaged iron concentrations discretized in 200 m depth intervals (solid line) and a strongly smoothed curve (dashed line) plotted on top are shown in **b)**.

concentrations of dissolved iron (< 0.2 µmol m^{-3}) in the Southern Ocean and elevated iron concentrations (> 0.6 µmol m^{-3}) in regions influenced by the atmospheric deposition of iron originating from nearby deserts. For example in the tropical Atlantic where dust from the Sarahan desert is deposited, iron concentrations are clearly elevated. The globally averaged vertical profile of dissolved iron observations reveals an approximate nutrient like profile with low concentrations at the surface and increasing concentrations at the midwater maximum (Fig. 1.2b). The shape of the profile is caused by biological uptake at the surface and remineralization of iron from organic particles at subsurface depths. However, below 2000 m iron concentrations decrease again because of scavenging, the chemical transformation of dissolved iron to particulate iron. Scavenging is explained in more detail in section 1.4.2.

1.4 The iron cycle and global ocean biogeochemical models

1.4.1 Phytoplankton iron uptake and limitation

Phytoplankton uses iron particularly in the photosynthetic system (Twining and Baines, 2013). Iron is a part of several enzymes and other proteins that are involved in the electron transport chain of photosynthesis, such as ferredoxin or the midstream oxidase

(Behrenfeld and Milligan, 2013). Multiple lab culture but also shipboard bottle incubation experiments show that the chlorophyll to carbon (Chl:C) ratio of phytoplankton and the initial slope in the photosynthesis-irradiance curve (P-I curve) are reduced under iron stress (Greene et al., 1991; Davey and Geider, 2001; Hopkinson et al., 2007; Moore et al., 2007; Hopkinson and Barbeau, 2008). The strongest physiological signal of iron stress is a reduced linear electron transfer so that both, maximum photosynthesis rate and the initial slope or half saturation rate in the P-I curve are affected by iron stress (cf. chapter 2). However, iron stress also downregulates nitrate and nitrite reductases (Behrenfeld and Milligan, 2013) and nitrogenase, an enzyme involved in nitrogen fixation (Berman-Frank et al., 2001). In summary, the physiological needs for iron are high in phytoplankton and particularly the photosynthetic capacity as well as nitrate uptake and nitrogen fixation might be reduced under iron limitation.

Before iron can be used physiologically by phytoplankton, it needs to be taken up. The iron uptake strategies of different phytoplankton groups differ. Photoautotrophic bacteria use siderophores to bind iron, prevent it from scavenging and eventually to take it up. Siderophores are small organic molecules (oligopeptides) that build complexes with iron and are assumed to be released by photoautotrophic bacteria (and other prokaryotes) under iron stress (Boyd and Ellwood, 2010). Eukaryotic phytoplankton like diatoms are not observed to produce siderophores. They take up dissolved inorganic iron (Fe') and rely on iron complexed with weaker ligands that are produced by heterotrophic bacteria during remineralization of organic particles (Gledhill and Buck, 2012). Before Fe(III) is taken up it has been shown to be reduced by enzymes in membranes of eukoryotes (Shaked et al., 2005). Small phytoplankton species have been observed to be capable of a more efficient iron reduction than larger phytoplankton cells reflecting the higher surface to volume ratio (Boyd and Ellwood, 2010). The small cells are thus often assumed to be less affected by low iron concentrations (e.g. Aumont et al. (2015)). Iron uptake ratios can vary strongly even within the same phytoplankton species (Sunda and Huntsman, 1997).

Global biogeochemical models use either a minimum function of limitation factors determined from for example iron, phosphate, nitrate and light limitation (Galbraith et al., 2010; Tagliabue et al., 2014a; Aumont et al., 2015) or compute the effective limitation by multiplication of the limitation factors (Parekh et al., 2008). The assumptions here are that only the most limiting factor determines phytoplankton growth (minimum function) or that iron colimits phytoplankton growth with other factors such as nitrate or light (multiplicative limitation). In some of these models the half saturation constant of iron uptake is affected to mimick higher iron uptake by small phytoplankton species (Galbraith

et al., 2010; Aumont et al., 2015). Additionally, Galbraith et al. (2010) modelled the effect of iron on the P-I curve by a dependence of the Chl:C ratio and initial slope of the P-I curve on iron concentrations. The effect of this can be quiet strong and its importance is tested in the sensitivity of atmospheric CO_2 levels on dust deposition in chapter 2.

1.4.2 Iron speciation and scavenging

Dissolved inorganic iron (Fe') is available for phytoplankton as a nutrient but quickly oxidized and scavenged in seawater. Scavenging summarizes several processes: 1) precipitation of iron to oxides, hydroxides and oxihydroxides (e.g. Fe_2O_3, $Fe(OH)_3$, $FeO(OH)$), 2) adsorption to particles, 3) colloid formation and subsequent coagulation (Wu et al., 2001; Rose and Waite, 2003). All of these processes ultimately lead to the transformation of soluble iron to particulate iron which is not available anymore for phytoplankton (cf. Fig. 1.3). On the one hand, the colloidal fraction that consists of iron complexed with organic ligands and suspended iron oxides is subject to aggregation which eventually leads to the formation of sinking iron particles. On the other hand, prior to aggregation, complexation of dissolved inorganic iron with organic ligands prevents the precipitation of soluble iron and is believed to largely maintain the bioavailability (Gledhill and Buck, 2012). Complexed iron is observed to be mainly dissolved in seawater but the binding strength of iron with ligands is variable and dependent on the type of ligand. The exact structure and nature of the ligands is not known today but ligands are often classified in two classes according to their binding strength (Rue and Bruland, 1995). The strong ligand class (L_1) is assumed to mainly consist of siderophores, i.e. small organic molecules that are released by bacteria under iron stress. Weak ligands (often denoted L_2) are produced during remineralization and cell lysis after grazing of phytoplankton. A more refractory part of the weak ligand class is also suggested to consist largely of humic acids (Laglera and van den Berg, 2009; Misumi et al., 2013) which are degradation products of organic matter. In most waters the ligand concentrations are found to be in excess of iron concentrations (Gledhill and Buck, 2012).

The strength of iron-ligands is expressed with the conditional stability constant $K_{FeL} = \frac{[FeL]}{[Fe][L]}$. Here, dissolved inorganic iron is denoted by Fe, the ligand concentration by L and iron complexed with a ligand FeL. The L_1 ligand class is defined by having a $\log(K_{FeL}) > 12$ and the L_2 class with a $\log(K_{FeL}) < 12$ (Gledhill and Buck, 2012). Iron ligands can be generally thought of as organic molecules that have one or more free electron pairs that can coordinatively bind to central metal ions such as Fe^{2+}. In contrast to a covalent bond, in coordinative bonds the ligand provides one or more electron pairs and the bond is weaker.

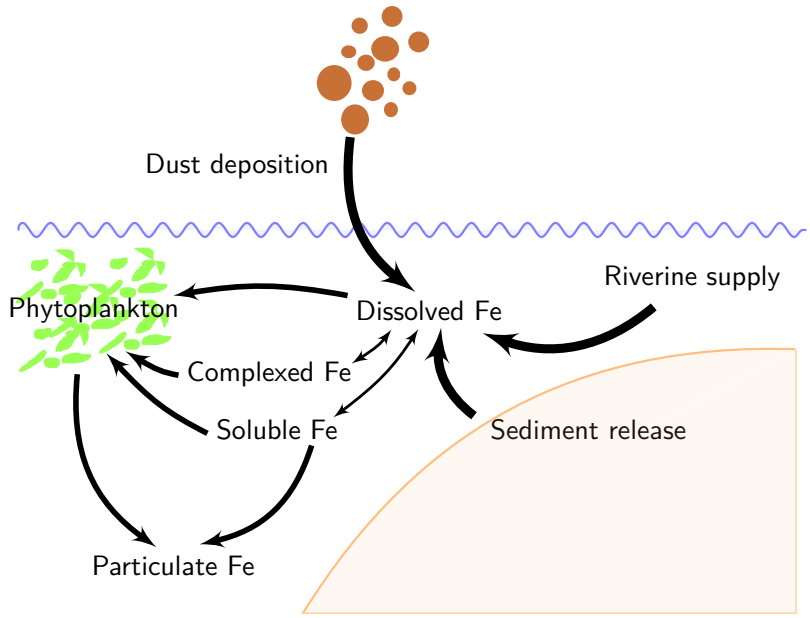

Figure 1.3: Strongly simplified schematic of the marine iron cycle as it is often represented in global ocean biogeochemical models. Of the external sources of iron to the ocean, only dust deposition and sediment release are often considered. Dissolved iron comprises complexed iron and soluble iron, both are available for phytoplankton. Only soluble iron is considered to scavenge and build particulate iron as for example in Galbraith et al. (2010).

In the euphotic zone, photochemistry is complicating the iron cycle. While on the one hand, photoreduction leads to increased concentrations of the more soluble iron species Fe(II), on the other hand photodissociation of Fe(II) and Fe(III) ligand complexes and subsequent scavenging could lead to a net loss of bioavailable iron (Barbeau, 2006). In addition, the photoreduced iron is quickly reoxidized to Fe(III). It is not very clear which mechanism prevails in the surface ocean. The rates of the individual processes are very uncertain, but in a global modeling study, Tagliabue et al. (2009b) found a positive trend of bioavailable iron with irradiance.

Generally, in global ocean biogeochemical models some rates such as complex formation and dissociation and the oxidation of Fe(II) to Fe(III) are too fast to be explicitly resolved. Instead, equilibrium assumptions of the complex formation and oxidation kinetics are often made. From given values for ligand concentration and the conditional stability constant K_{FeL}, the concentration of soluble inorganic iron can be computed, making use of the conservation of total ligand and total iron concentrations in models (Parekh et al., 2005; Moore and Braucher, 2008; Galbraith et al., 2010; Aumont et al., 2015). In many models only the dissolved inorganic iron (Fe') is subject to first order

scavenging rates. The conditional stability constant K_{FeL} and total ligand concentration are often assumed to have globally fixed, spatially not varying values (Parekh et al., 2005; Moore and Braucher, 2008). However, to mimic the photodissociation of iron-ligand complexes, Galbraith et al. (2010) decrease K_{FeL} with increasing irradiance and Aumont et al. (2015) make K_{FeL} dependent on temperature as proposed by Liu and Millero (2002).

At very low oxygen concentrations <5 mmol m^{-3} elevated dissolved iron concentrations are repeatedly observed at the eastern subtropical north Pacific (Hopkinson and Barbeau, 2007), eastern subtropical south Pacific (Vedamati et al., 2014) and in the northern Indian Ocean (Moffett et al., 2007). In these regions, oxygen minimum zones are present due to high bacterial respiration of organic matter during which oxygen is consumed. The sluggish ventilation in the oxygen minimum zones prevents oxygen supply from the ocean surface, which is saturated with oxygen from the atmosphere. The low concentration of oxygen leads to a slowed iron oxidation and significant amounts of Fe(II) are observed in the low oxygen waters. One source of Fe(II) is the sediment where iron can be used as an electron acceptor by bacteria and Fe(II) is released to the water column. As soon as this Fe(II) is transported to waters with higher oxygen concentrations it is oxidated again and most of the iron precipitates as iron oxides (Scholz et al., 2011). In their ocean biogeochemical model, Galbraith et al. (2010) account for the slowed down oxidation of iron under low oxygen concentrations by simply setting all scavenging processes to zero when oxygen concentrations fall below 5 mmol m^{-3}. However, elevated Fe(II) concentrations are also observed away from the sediment at the upper boundary of the oxygen minimum zones where the Fe(II) can not stem from the iron reduction in the sediment (Hopkinson and Barbeau, 2007). One process that could explain the Fe(II) accumulation is iron reduction as an iron acquisition strategy of microbes (Moffett et al., 2007) but evidence is still missing.

Since iron isotopes are not part of this thesis but can be used to identify the origin and fate of observed iron concentrations (Radic et al., 2011), they are only briefly mentioned here. Although the differences in the isotopic fractionation are small, iron from atmospheric deposition, release by hydrothermal vents, riverine supply and sediment release have different isotopic signatures that in principle allow to indicate the source of observed iron concentrations in seawater (Radic et al., 2011). Additionally, in marine sediments a low δ^{56}Fe value indicates a reduction and subsequent release of iron because bacteria preferably use the isotopically light iron (^{54}Fe) for the reduction of organic matter (Severmann et al., 2010; Scholz et al., 2014b). The growing number of iron-isotope measurements could thus serve as an additional constraint for ocean biogeochemical models

in the future.

1.4.3 Particulate iron, sinking and remineralization

The biological uptake of iron by phytoplankton and the chemical precipitation, scavenging and coagulation of dissolved iron produce particulate iron that sinks to deeper waters (Boyd et al., 2010a). Most of the insoluble lithogenic particulate iron (e.g. from dust deposition) aggregates in the euphotic zone with organic matter so that organic and inorganic particulate iron is difficult to distinguish in subsurface and deep waters (Boyd and Ellwood, 2010). While there is strong uncertainty in the exact rates of remobilization of iron from particles, the fraction of new to regenerated iron, often expressed as the fe ratio (fe= new iron / (new iron + regenerated iron)), is observed to be relatively small in HNLC regions. This indicates the importance of remobilization of iron from the particulate phase. In the euphotic zone this rapid turnover between particulate and dissolved iron is termed the "ferrous wheel". Grazing by bacterivory and herbivory zooplankton as well as remineralization of iron in organic matter by bacteria are contributing to the ferrous wheel (Boyd et al., 2010a). Below the euphotic zone, remobilization of particulate iron is much slower and partly balanced by rescavenging of iron (Boyd et al., 2010b). A factor influencing how much remobilized iron stays dissolved in seawater is the simultaneous release of iron-binding ligands from organic matter (Boyd et al., 2010a). Generally, the decrease of particulate iron with depth seems to be smaller than the decrease of particulate organic carbon indicating that a pool of iron is refractory or that rapid rescavenging balances the remobilization of iron (Boyd and Ellwood, 2010).

The particulate iron pool is treated very differently in global models of the iron cycle. The most complex models resolve organic and inorganic particulate iron (Aumont et al., 2015), some models assume just one pool of particulate iron with no distinction between organic and inorganic particles (e.g. Galbraith et al. (2010)) and others do not account for particulate iron at all but just assume that all scavenged iron is lost permanently from the ocean (Parekh et al., 2008). A higher resolution of different particle types is complicated because of the uncertainty in rates of aggregation processes of organic and inorganic particles, scavenging and ligand complexation (Weber et al., 2007).

1.4.4 Dust deposition

One of the major external sources of iron to the ocean is dust deposition (Jickells et al., 2005) (Fig. 1.3). Terrestrial dust that is eroded from arid areas such as deserts contains a certain amount of iron and is transported by winds in the atmosphere and eventually deposited to the ocean. The result is enhanced iron concentrations in the areas where

dust deposition occurs. The most prominent dust deposition region is the tropical and subtropical North Atlantic where trade winds transport dust from the Sahara over the ocean. Further major dust deposition regions are the northern Indian Ocean, the Southern Ocean south east of Australia and of Patagonia and the North Pacific region downwind of the Gobi desert (Maher et al., 2010). Deposition of dust can occur by wet and dry deposition. Wet deposition describes the removal of aerosol particles by precipitation events while dry deposition occurs due to turbulent deposition (random contact with the ocean surface due to small-scale eddies) and gravitational settling (Mahowald et al., 2009).

The fraction of iron that dissolves when dust is deposited to the ocean is observed to be highly variable. The responsible processes that determine thesolution of iron from the atmosphere in the ocean could not yet be clearly determined. Observations show a wide range of iron solubility of 0.001%-80% (Jickells et al., 2005). Luo et al. (2008) used a atmospheric transport model and found that acidic leaching of iron from minerals in acid clouds is able to explain the observations best although strong discrepancies remain. Other studies focus less on the mechanisms that determine the solubility of iron in dust and instead simply observe an inverse trend of iron solubility with mineral dust concentration (Baker and Croot, 2010). Iron solubility is found to be low at high dust deposition and high at low dust deposition. Baker and Croot (2010) suggest that preferential deposition of larger dust particles with lower surface area to volume ratio and hence less dissolvable iron at the surface of the particle could be the mechanism behind the inverse relationship. However, they also state that this is very likely not the sole mechanism.

Due to the unclear processes that determine iron solubility, in many ocean biogeochemical models, dust deposition maps are used together with an assumed constant solubility of iron in dust. The assumed constant solubility varies between 0.5% and 1% (Parekh et al., 2008; Tagliabue et al., 2009c). Among others, the effect of the constant solubility assumption is tested under preindustrial conditions in chapter 3. The dust deposition maps employed in ocean biogeochemical models are derived from simulations with atmosphere models that include dust source regions and model the transport of particles until their deposition (Mahowald et al., 2009). Different assumptions in the erosion of dust and differences in the setup of the physical transport model can lead to different dust deposition distributions (e.g. Mahowald et al. (2006) and Ginoux et al. (2004)). However, such models allow to produce estimates of dust deposition for example during the last glacial maximum which may then be used for studies with ocean biogeochemical models (Mahowald et al., 2006; Parekh et al., 2006).

1.4.5 Sediment release

While atmospheric dust deposition was discovered early as an important external source of iron to the ocean, the role of sediment release was believed to be restricted to coastal regions at first. For instance, Bruland et al. (2005) observe very high phytoplankton concentrations at the northern coast off Peru where the shelf is broad and iron is readily available. In contrast, in southern Peru the shelf is very narrow, iron concentrations are far lower and phytoplankton grows much less despite similar macronutrient concentrations. Capone and Hutchins (2013) find similar patterns along the coast of California and suggest that sediment-derived iron is a key determinant of biological productivity particularly in coastal upwelling regions. However, recent observations suggest that sediment released iron is not only important for coastal productivity but may also reach up to 1200 km offshore (Elrod et al., 2004; Severmann et al., 2010) and thus may influence phytoplankton growth in larger parts of the ocean. This strong impact of the sedimentary iron release is also confirmed by modeling studies. Moore and Braucher (2008) suggest that models, which do not include a sedimentary source of iron, will overestimate the impact of variations in dust deposition on the marine carbon cycle.

Sediment release of iron is found to be correlated with the amount of organic carbon that sinks to the sediment and is oxidized therein (C_{ox}) (Elrod et al., 2004). The low oxygen concentrations created by the oxidation of the organic carbon in the sediment favor the iron release. The highest sedimentary iron fluxes were hence observed at very low bottom water oxygen concentrations, e.g. below 5 mmol O_2 m^{-3} (Noffke et al., 2012; Scholz et al., 2014a). At the Oregon-California continental shelf the benthic iron flux is also observed to be extremely high under low oxygen concentrations (Severmann et al., 2010). Sediments on the shelf, which are influenced by high riverine iron discharge, are suggested to be underestimated in their role in releasing iron that may reach the surface (Severmann et al., 2010). Although up to 95% of the dissolved iron in rivers might be lost as particulate iron before it reaches the ocean (Wetz et al., 2006), a large part of the scavenged iron could sink to the sediment and contribute largely to the availability of reactive iron that could be released again.

Specifically, dissimilatory iron reduction (DIR) in sediments is an important mechanism for the release of iron (Jones et al., 2011). DIR describes the oxidation of organic material with iron as an electron-acceptor by heterotrophic bacteria. When organic matter reaches the sediment, it is remineralized by heterotrophic bacteria with the use of oxygen. If oxygen is depleted nitrate, manganese, iron and sulfate are used for the remineralization, generally in this order but sometimes simultaneously (Kraal et al., 2012). Reactive iron

particles that are used for the oxidation of organic matter are iron oxides (e.g. hematite), pyrite and to a lesser degree iron in reactive silicates and magnetite (Canfield et al., 1992). Iron in crystalline silicate minerals are rather unreactive particulate iron species. Therefore, the concentration of reactive iron could limit the release of iron from the sediment in some regions (Severmann et al., 2010).

The sediment release is modeled very differently in existing global ocean biogeochemical models that include an iron cycle. The sediment release in the model by Tagliabue et al. (2014a) is only dependent on ocean depth because they assume that C_{ox} is directly proportional to ocean depth and the primary driver of iron release. Changes in the amount of C_{ox} supplied to the sediment do hence not alter the sediment release in their model. In some models the observed ratio of iron release to C_{ox} by Elrod et al. (2004) is applied (e.g. Moore and Braucher (2008); Galbraith et al. (2010)). Additionally, in the model by Galbraith et al. (2010) iron release is also oxygen dependent. They introduced a threshold of oxygen concentrations below which all particulate iron supplied to the sediment is released back to the water column as dissolved iron. A simple function describing the sediment release of iron in dependence on C_{ox} and O_2 is developed and tested in a global model in chapter 4. The implications of the new function for the modeled global iron cycle are analyzed in chapter 5.

1.4.6 Riverine iron supply

Recently measured iron concentrations in river waters are 120 nM (Wetz et al., 2006) and 200 nM (Colbert, 2004) and thus much higher than the iron concentrations of around 0.7 nM observed in the ocean (Tagliabue et al., 2012) (Fig. 1.2). However, how much of the iron is reaching the ocean is not clear. Large parts of the dissolved iron are scavenged at the river-ocean interface by salt-induced flocculation. Yet, the scavenged iron could contribute to the shelf iron inventory (Boyd and Ellwood, 2010), which possibly determines how much iron is available for the sediment release. If this supply of iron delivers reactive iron species to the sediment, rivers could be very important in controlling the sediment release of iron that has already be identified to be a crucial source of iron to the ocean.

The riverine source of iron has not received much attention in global ocean biogeochemical models (da Cunha and Buitenhuis, 2013). In a regional high resolution modelling study in the tropical Atlantic riverine supply of iron is found to increase primary productivity in coastal regions and to be an important source of iron to sustain nitrogen fixation (da Cunha and Buitenhuis, 2013). Cotrim da Cunha et al. (2007) study the importance

of coastal nutrient supply for global ocean biogeochemistry. They find a high sensitivity of primary and export production to coastal phosphorus, iron and silicate supply, in particular in upwelling regions with high runoff but also generally in eastern margin seas. In a similar global modeling study Giraud et al. (2008) find that supply of iron from coastal processes (including riverine supply) appears to have the largest potential impact on open ocean biogeochemistry compared to other nutrients because of the limited vertical supply of iron due to scavenging. Therefore, although riverine supply of iron has been shown to be potentially important, it has not been investigated much. Chapter 5 thus focuses on the potentially important role of riverine iron sources and its interaction with sedimentary iron release.

1.4.7 Other external sources

One other external source of iron to the ocean is ice meltwater (Bhatia et al., 2013) that can stem from glacial and iceberg melt or from seasonal sea-ice retreat (Sedwick and DiTullio, 1997). Much of the meltwater discharged into the ocean interacts with basal sediment and bedrock material before exiting at outlet glaciers. Mechanical and chemical weathering beneath glaciers may produce nanoparticulate iron that is transported with the glacier. Subglacial microbial activity may produce iron minerals that are more labile than the original silicate rocks, and thus supply dissolved iron to the runoff waters. The presence of organic ligands and iron-reducing anoxic regions at the bed of glaciers could then serve to maintain a portion of the iron in solution (Bhatia et al., 2013).

Located at deep-sea environments, hydrothermal vents are suggested to provide a large source of iron to the ocean as well (Saito et al., 2013). The heated and acid water in the vents leaches iron and other minerals from the surrounding rocks and pours out of the vent. However, due to rapid reprecipitation in the seawater around the vent, iron released from hydrothermal vents does reach the ocean surface only to a very small part and thus has a small impact on ocean surface productivity (Tagliabue et al., 2010).

Although dust deposition is the dominant aerosol source, iron in dust is not the only aerosol iron source to the ocean. Extra-terrestrial dust, iron-rich particles from urban pollution and biomass burning are also observed to be minor sources of iron to the ocean (Luo et al., 2008; Boyd and Ellwood, 2010).

1.5 Dust deposition and glacial-interglacial cycles

The iron hypothesis by Martin and Gordon (1990) proposes that iron fertilization by increased dust deposition to the Southern Ocean during last glacial times was partly responsible for the drawdown of atmospheric CO_2. Martinez-Garcia et al. (2014) analyzed a sediment core from the Subantarctic Atlantic to reconstruct ice age nitrate consumption, burial fluxes of iron, and proxies for productivity and found that subantarctic iron fertilization could be an explanation for the lowering of CO_2 at the transition from mid-climate states to full ice age conditions. They find that during the last glaciation, atmospheric CO_2 levels decreased from around 270 ppm to 190 ppm during ca. 110,000 years until the Last Glacial Maximum (LGM) around 20,000 years ago. An ice record from the Vostok station in East Antarctica allows to also reconstruct atmospheric composition and climate of the past four glacial-interglacial cycles. An elevated dust deposition is found for each of the four glacial periods (Petit et al., 1999). Although the strength of the desert-dust connection is still under debate it is therefore very likely that dust deposition and climate are strongly coupled.

Many studies employ physical ocean circulation models that include marine biogeochemical models to explore how much of the glacial decrease in atmospheric CO_2 concentrations can be attributed to changes in dust deposition. Reductions of atmospheric CO_2 in response to increases of the dust deposition to estimates of the LGM range from 10 μatm (Parekh et al., 2008) to 25 μatm (Oka et al., 2011). The reasons for the differences are difficult to assess because of the many differences of the biogeochemical models and the uncertainties in the iron cycle (Tagliabue et al., 2008). Due to the high variability in the response of atmospheric CO_2 to changes in dust deposition by model sensitivity studies to dust deposition, the quantitative influence of dust deposition on atmospheric CO_2 levels remains a matter for investigation. However, the model results indicate that iron fertilization by dust deposition can not explain the full glacial decrease of 80 ppm but is major factor that contributes to the decrease.

1.6 Chapter synopsis and author contributions

Chapter 2 focuses on the effect of iron-light colimitation on the sensitivity of oceanic CO_2 uptake to dust deposition. The results reveal an enhanced sensitivity of atmospheric CO_2 concentration by 19% of the total response for a dust deposition estimate of the last glacial maximum. For a dust deposition estimate for a climate with double CO_2 concentration relative to today the sensitivity of atmospheric CO_2 concentration increases by 32%. This chapter is from the published manuscript: Nickelsen, L., and Oschlies,

A. (2015). Enhanced sensitivity of oceanic CO_2 uptake to dust deposition by iron-light colimitation. *Geophysical Research Letters*, 42, 492–499. doi:10.1002/2014GL062969.
L. Nickelsen conceived the idea and designed the experiments. He performed all simulations, calculations and analyses. L. Nickelsen also wrote the manuscript, with comments provided by A. Oschlies.

Chapter 3 introduces the coupling of a dynamic marine iron cycle to an existing global climate model of intermediate complexity, which uses a static iron concentration mask. The results show that including a dynamic iron cycle leads to a better agreement between observed and simulated iron concentrations than with the iron concentration mask used in the previous model. Due to the dynamic iron cycle the response to possible perturbations of the iron cycle is interactive with the ocean biogeochemistry. A strong sensitivity of simulated iron concentrations to parameterized ligand concentrations indicates a key role of ligand dynamics in regulating the dissolved iron content of seawater. While a variable solubility of iron in dust mainly has a strong impact on iron concentrations simulated in the model, a subgridscale bathymetry for sedimentary iron release has a very strong impact on both, iron and macronutrient concentration. This is due to the fact that sediment release is the dominant source of iron in iron limited regions such as the Southern Ocean and eastern tropical Pacific in our model. This chapter is from the manuscript that is published as a discussion paper and accepted for a peer-reviewed publication: Nickelsen, L., Keller, D., and Oschlies, A. (2014). A dynamic marine iron cycle module coupled to the University of Victoria Earth System Model: the Kiel Marine Biogeochemical Model 2 (KMBM2) for UVic 2.9. *Geoscientific Model Development*, accepted.
A. Oschlies and L. Nickelsen conceived the idea and L. Nickelsen designed the experiments. L. Nickelsen performed all simulations, calculations and analyses. He also wrote the manuscript, with comments provided by D. Keller and A. Oschlies.

Chapter 4 uses a compilation of benthic iron flux observations to develop a simple transfer function of benthic iron release that can be applied easily to ocean biogeochemical models. The results provide an estimate of the global dissolved iron flux from marine sediments of 109 $\pm$ 23 Gmol yr^{-1} and suggest that the benthic dissolved iron flux has been underestimated in the marine iron cycle. Applying the simple transfer function in a global ocean biogeochemical model leads to a strong overestimation of iron concentrations. Since scavenging rates are not well constrained, they are suggested to be possibly underestimated in the model and other models that use similar scavenging rates. This chapter is from the manuscript: Dale., A. W., Nickelsen, L., Scholz, F., Hensen, C., Oschlies, A. and Wallmann, K. (2015), A revised global estimate of dissolved iron fluxes from marine

sediments. *Global Biogeochemical Cycles*, accepted, doi:10.1002/2014GB005017.
A. Dale conceived the idea and performed all simulations with the sediment model, calculations and analyses. L. Nickelsen performed the global ocean biogeochemical model simulations. A. Dale wrote the manuscript and L. Nickelsen wrote the description and discussion of the global modelling results in section 7 and contributed to the general introduction. Comments on the whole manuscript were provided by all co-authors.

Chapter 5 further investigates implications of the transfer function developed in chapter 4 for the global marine iron cycle. The results show that the overestimation of iron concentrations in the ocean found in chapter 4 only takes place if it is assumed that there is an unlimited supply of reactive iron to the sediment as usually done in global biogeochemical models. If a balance between reactive iron supplied to and released from the sediment is assumed, iron concentrations are largely underestimated and reactive iron supplied to the sediment limits the release of iron in large parts of the ocean. The results further show that a riverine source of iron can supply enough reactive iron to create a sediment source of iron that leads to a good agreement between observed and simulated iron concentrations in the ocean. Changes in the reactive iron supplied through rivers are found to have a strong impact on ocean biogeochemistry, in particular near oxygen minimum zones. This chapter is from the manuscript: Nickelsen, L., Dale, A., Wallmann, K. and Oschlies A. (2015), Riverine supply of iron is needed to sustain iron release from marine sediments in a global ocean biogeochemical model, in preparation.
L. Nickelsen, K. Wallmann, A. Dale and A. Oschlies conceived the idea and L. Nickelsen designed the experiments. L. Nickelsen performed all simulations, calculations and analyses. He also wrote the manuscript with comments provided by A. Dale.

2 Enhanced sensitivity of oceanic CO_2 uptake to dust deposition by iron-light colimitation

This chapter is based on the paper "Enhanced sensitivity of oceanic CO_2 uptake to dust deposition by iron-light colimitation" published in the journal Geophysical Research Letters.
Citation: Nickelsen, L., and Oschlies, A. (2015). Enhanced sensitivity of oceanic CO2 uptake to dust deposition by iron-light colimitation. Geophysical Research Letters, 42, 492—499. doi:10.1002/2014GL062969

Abstract The iron hypothesis suggests that in large areas of the ocean phytoplankton growth and thus photosynthetic CO_2-uptake is limited by the micronutrient iron. Phytoplankton requires iron in particular for nitrate uptake, light harvesting and electron transport in photosynthesis, suggesting a tight coupling of iron and light limitation. One important source of iron to the open ocean is dust deposition. Previous global biogeochemical modeling studies have suggested a low sensitivity of oceanic CO_2-uptake to changes in dust deposition. Here we show that this sensitivity is increased significantly when iron-light colimitation, i.e. the impact of iron bioavailability on light harvesting capabilities, is explicitly considered. Accounting for iron-light colimitation increases the shift of export production from tropical and subtropical regions to the higher latitudes of subpolar regions at high dust deposition and amplifies iron limitation at low dust deposition. Our results re-emphasize the role of iron as a key limiting nutrient for phytoplankton.

2.1 Introduction

Low concentrations of the micronutrient iron limit primary production in vast areas of the ocean and in particular in most parts of the Southern Ocean (Boyd and Ellwood, 2010). One of the major sources of iron to the ocean is dust deposition that is suggested to be coupled intimately to climate (Martínez-Garcia et al., 2011). While today dust deposition to the Southern Ocean is very low, the iron hypothesis (Martin, 1990) states that enhanced dust deposition to the Southern Ocean during the last glacial maximum triggered additional export of organically bound carbon and therefore decreased atmospheric CO_2 concentrations. Although a recent modeling study estimates only an increase of 2 ppmv in preindustrial atmospheric CO_2 when dust deposition is shut off completely (Tagliabue et al., 2014a), other studies suggest that decreasing dust deposition in the future such as predicted by Mahowald et al. (2006) may possibly lead to more severe iron limitation and a larger reduction in oceanic CO_2 uptake by phytoplankton (Parekh et al.,

2006; Tagliabue et al., 2008). The role of iron in regulating the oceanic CO_2 uptake is thus important for understanding past and possibly future atmospheric CO_2 levels.
From a biological point of view iron limitation in coupled biogeochemical ocean circulation models has, until now, been treated in a very simplistic way and interactions with other limiting nutrients and factors are often neglected. Observations show that iron limitation of phytoplankton growth is created by the requirement of iron for nitrate uptake, for proteins in the electron transport chain, for synthesizing chlorophyll and photoreaction centers and the functioning of light harvesting antennae (Sunda and Huntsman, 1997; Behrenfeld and Milligan, 2013). Although physiological adaptation of polar phytoplankton species to low iron concentrations may compensate for some of the positive effect of iron on light harvesting capabilities (Strzepek et al., 2011, 2012), incubation experiments show elevated light harvesting capabilities of phytoplankton after adding iron (Feng et al., 2010). However, in most biogeochemical models that have been used to investigate the sensitivity of ocean biogeochemistry and CO_2 uptake to dust deposition, iron limitation is included as a further Monod term in a minimum function (Bopp et al., 2003; Moore and Braucher, 2008; Parekh et al., 2008; Tagliabue et al., 2009a) while in explicit quota models such as in Tagliabue et al. (2009a, 2014a) iron uptake is allowed to continue also under light limiting conditions. Only the recent model of Galbraith et al. (2010) explicitly describes the impact of iron limitation on the chlorophyll-to-carbon ratio and the initial slope of how irradiance is processed into photosynthesis as observed in culture and field experiments (Greene et al., 1991; Davey and Geider, 2001; Hopkinson et al., 2007; Moore et al., 2007; Hopkinson and Barbeau, 2008). The way the influence of iron limitation on light limitation is implemented in this model leads to parallel changes in the light-limited slope and light-saturated rate of photosynthesis with iron concentrations (Figure 2.1). The increase of the maximum growth rate only, as illustrated in Figure 2.1, is the response to additional iron as it is often treated in the other models. Here, in addition, also the initial slope increases. This response of both, maximum growth rate and initial slope, to the addition of iron is also observed in culture experiments (Behrenfeld et al., 2004; Behrenfeld and Milligan, 2013).
The model used here has been shown to perform well in simulating the observed present-day global surface iron and phosphate concentrations while the agreement to observations decreases if iron limitation of light harvesting capabilities is not considered (Galbraith et al., 2010). However, how iron limitation of light harvesting capabilities influences the response of oceanic CO_2 uptake to changes in dust deposition has yet to be answered.

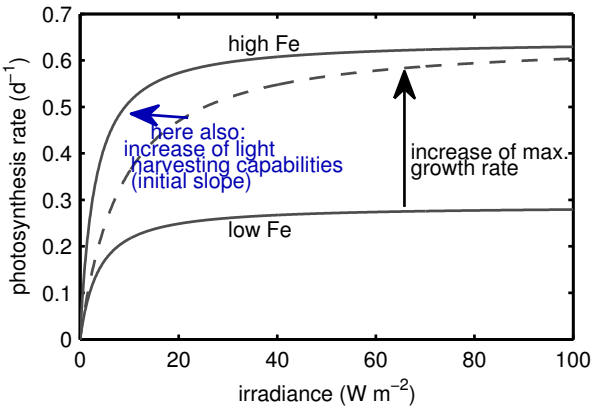

Figure 2.1: Impact of iron on the photosynthesis irradiance (P-I) curve. The lower solid line represents the P-I curve for low iron concentrations, the upper solid line represents the P-I curve for high iron concentrations in the model we use here. The dashed line represents the P-I curve if a higher iron availability only increases the maximum growth rate and not the light harvesting capabilities.

2.2 Methods

The model we use is a coupled global ocean-biogeochemistry model with a detailed iron cycle (Galbraith et al., 2010). In brief, the biogeochemical model consists of four prognostic tracers, namely phosphate (PO_4), dissolved organic phosphorus (DOP), dissolved iron (Fe) and oxygen (O2). Phytoplankton biomass is modeled as a prognostic variable that is not transported. Export production, grazing and community structure formulations are based on empirical formulations by Dunne et al. (2005). External sources of iron to the ocean are dust deposition and sediment release. The complexation of iron with organic ligands is implicitly calculated as in Parekh et al. (2006). A complete description of the biogeochemical model based on the model code made available by Galbraith et al. (2010) is included in Nickelsen (2011).

The difference of our approach in comparison to prior approaches is illustrated in the photosynthesis-irradiance (P-I) curve in Figure 2.1. If increased iron concentrations only increase the maximum photosynthesis, the effect is most pronounced at high light levels. If the impact of iron on light harvesting capabilities is considered as well, also the slope of the response of photosynthesis to irradiance increases. This has a particularly strong effect at low light levels.

The physical ocean model configuration used in this study is described by Galbraith et al. (2010, 2011). The model is the coupled ocean-sea ice model component of the climate model version 2 with the Modular Ocean Model version 4p1 at coarse resolution (CM2Mc). It has a nominal resolution of 3 degrees in longitudinal direction and 3 degrees in latitudinal direction with a higher resolution up to 2/3 degrees near the equator and at the latitudes of the Drake Passage and the equivalent latitudes on the Northern Hemisphere.

The vertical resolution of the model consists of 28 levels with pressure as the vertical coordinate and a free sea surface. The vertical resolution varies from 10 m at the surface to 506 m in the lowest layer. The ocean surface is forced using a repeated climatological year from the Coordinated Ocean Reference Experiment (CORE) (Griffies et al., 2009). Surface salinities are restored to observations with a time constant of 10 days over the top layer.

We ran the model in a coupled ice-ocean mode with fixed atmospheric forcing and prescribed atmospheric 278 μatm CO_2 for 2500 years as a spinup run. To simulate aeolian deposition of iron a repeated climatological seasonal cycle of dust deposition (Ginoux et al., 2004) is used. Dust deposition is converted to iron deposition assuming a fraction of iron in dust of 3.5 % in clay fractions and 1.2 % in silt fractions and an iron solubility of 2 % following Galbraith et al. (2010). Burial of organic matter or $CaCO_3$ is not allowed in any of our simulations. After the spinup, we applied a dynamic and homogenous atmospheric CO_2 reservoir with an initial value of 590 Pg C (Sarmiento and Gruber, 2002) corresponding to 278 µatm. The atmospheric CO_2 reservoir is in exchange with the ocean but does not affect temperature. The experiments were started after 200 additional years of spinup with a free atmospheric CO_2 concentration. During these 200 years the change of average surface phosphate concentrations was -6.1×10^{-4} mmol PO_4 m^{-3} and the atmospheric CO_2 concentration decreased from 278 µatm to 277.81 and to 277.63 µatm during the following 1000 years of the control simulation. The decrease is likely due to the small but continuous accumulation of iron from the sediments (Galbraith et al., 2010).

Before starting our model sensitivity experiments, the model was tuned to reproduce observed responses to the two iron fertilization experiments, SOIREE (Boyd et al., 2000) and IRONEXII (Coale et al., 1996), in the same way as Aumont and Bopp (2006). The experiment SOIREE was conducted in the Southern Ocean while IRONEXII in the equatorial Pacific. To simulate the mesoscale iron fertilization experiments the iron concentration was set to 2 nM in the whole mixed layer every 5 degrees in latitudinal and 9 degrees in longitudinal direction and held constant for 30 days. For SOIREE the ocean was fertilized only south of 40°S starting with February in our model and for IRONEXII between 5°S and between 5°N and 140°E and 120°W starting in May. To calculate ΔpCO_2 the simulation was repeated without iron fertilization and the difference in pCO_2 was calculated from these two simulations. Following Aumont and Bopp (2006), the response to fertilization was determined from sites that were within ± 10 m difference in the mixed layer depth and ± 2 °C to the respective fertilized location in SOIREE or IRONEXII. The responses in pCO_2 of these fertilization sites give a range of responses that are then compared to the observed values. The model parameters were optimized to reduce the difference between observed and simulated ΔpCO_2. In the resulting parameter set the stability constant of

iron-ligand complexes increases from $KFeL_{min} = 8 \times 10^9$ M^{-1}, $KFeL_{max} = 8 \times 10^{10}$ M^{-1} to $KFeL_{min} = 1 \times 10^{11}$ M^{-1}, $KFeL_{max} = 5 \times 10^{11}$ M^{-1}. These values are more in line with a recent compilation by Gledhill and Buck (2012) of $KFeL$ being in the range of 10^{11} to 10^{12} M^{-1}. The half-saturation constant of iron to phosphate uptake ($k_{Fe:P}$) is reduced from 0.8 mmol Fe (mol PO_4)$^{-1}$ to 0.4 mmol Fe (mol PO_4)$^{-1}$ and the mortality rate (λ_0) is increased from 0.19 d^{-1} to 0.38 d^{-1} to better reproduce the observations.

We perform 4 sensitivity experiments to test the importance of iron-light colimitation at different iron concentrations: (i) Abrupt increase of dust deposition to a deposition as estimated for the last glacial maximum (Mahowald et al., 2006) hereafter abbreviated as LGM-ILL. (ii) Equal to (i) but without the impact of iron on light harvesting capabilities (LGM-NOILL). (iii) Abrupt decrease of dust deposition to a deposition as estimated for a climate with double CO_2 concentrations relative to today (Mahowald et al., 2006) hereafter abbreviated as 2xCO_2-ILL. (iv) As (iii) but without the impact of iron on light harvesting capabilities (2xCO_2-NOILL). In addition to the sensitivity experiments the spinup run is continued with a prognostic atmospheric CO_2 reservoir as a control simulation to compare the experiments to (CTL). All dust deposition fields are shown in the Supplementary Figure S1.

The dust deposition used in the control run and the preindustrial estimate by Mahowald et al. (2006) differ. To make the experiments independent of the control dust deposition, the dust deposition estimates in the experiments are created by multiplying the dust deposition in the control run with the ratio of the LGM or 2xCO2 dust deposition estimates by Mahowald et al. (2006) to the preindustrial estimate by Mahowald et al. (2006). Additional experiments were performed without scaling the change in dust deposition to the preindustrial estimate, thus using the absolute dust deposition fields as simulated by Mahowald et al. (2006) (Supplementary Figure S2). In these additional runs more CO_2 is taken up using the LGM dust and less using the 2xCO2 dust. The impact of iron limitation of light harvesting capabilities, however, is as strong as in the simulations shown here.

Note that we are not trying to realistically simulate past conditions of the last glacial maximum or predictions into the future. Atmospheric forcing, temperature and circulation remain at preindustrial conditions in all our sensitivity experiments and we concentrate our analysis of a more mechanistic parameterization of iron limitation on the isolated impact of changes in aeolian iron supply. Also fraction and solubility of iron in dust in all experiments are kept as in the spinup run for reasons of comparability.

To turn off the effect of iron on light harvesting capabilities in experiments 2) and 4), the variables describing the light harvesting capabilities, the initial slope in the P-I curve (α^{chl}) and the chlorophyll-to-carbon ratio (θ^{Fe}_{max}) (also see the model description in Nick-

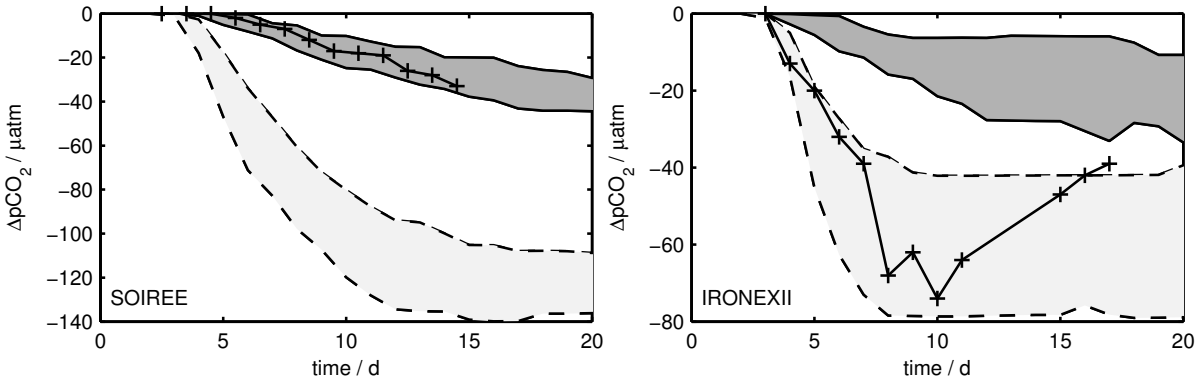

Figure 2.2: Comparison between observed and simulated response in pCO_2 to mesoscale iron fertilization as in the experiments SOIREE (Boyd et al., 2000) (left) and IRONEXII (Coale et al., 1996) (right). The crosses are observed differences between pCO_2 inside and outside the fertilization area as read by eye from (Aumont and Bopp, 2006). The light shaded area indicates the simulated response with parameters as in Galbraith et al. (2010) and the dark shaded area with the new parameter values. Note the different scales.

elsen (2011)), are kept at the annual mean values they have at the end of the spinup run at each point in space. There is thus no seasonal cycle of these variables in the experiments with no iron limitation of light harvesting capabilities whereas in the control experiment α^{chl} and θ^{Fe}_{max} vary seasonally. In a comparison between the control experiment to an additional control experiment (not shown here) in which we fixed α^{chl} and θ^{Fe}_{max} to the annual mean of the last year of the spinup, the differences are very small and, in terms of the atmospheric carbon reservoir, amount to 0.6 µatm.

2.3 Results and Discussion

2.3.1 Tuning the model

In order to validate the response of the model to changes in iron concentrations, we tune the model to be able to reproduce observed responses to mesoscale iron fertilization experiments in the same way as Aumont and Bopp (2006) (Figure 2.2a). With the original parameter set of Galbraith et al. (2010) pCO_2 is much more reduced than observed in SOIREE while with the tuned parameter set the observed values are perfectly within the simulated range of ΔpCO_2. On the other hand, the difference between new and old parameters is not that pronounced in the fertilization experiment IRONEXII. With the new parameter set ΔpCO_2 is underestimated although at the end of the experiment the observed value lies in between of the simulated ranges of original and new parameter set.

The root mean square errors (RMSE) for the simulated phosphate, oxygen and iron concentrations compared to observations from the World Ocean Atlas and Tagliabue et al. (2012) are 0.30 mmol PO_4 m^{-3}, 34.79 mmol O_2 m^{-3} and 1.0 nM dFe, respectively, using

the original parameter set by Galbraith et al. (2010). With the tuned parameter set the RMSE for phosphate does not change, the RMSE for oxygen concentrations increases slightly to 36.73 mmol O_2 m^{-3} and the RMSE for iron concentrations reduces strongly to 0.89 nM dFe for the full ocean and from 0.27 nM dFe to 0.26 nM dFe at the surface. It is encouraging that the model we use is able to reproduce the observed response to iron fertilization during SOIREE in the Southern Ocean and that the agreement to observed iron concentrations is improved with the tuned parameter set.

2.3.2 Oceanic CO_2 uptake

The LGM dust deposition leads to a total decrease of atmospheric CO_2 by 22.8 µatm (Figure 2.3a) in our model simulations. This decrease is about 19% larger (or 3.7 µatm) than that of simulation LGM-NOILL, which does not account for iron-light colimitation. Recent estimates of the CO_2 uptake of the ocean by increasing the dust to LGM conditions have all been smaller than in our idealized model results. The oceanic drawdown of CO_2 in simulations with dust of the last glacial maximum from the literature are 11µatm (Bopp et al., 2003), 10 µatm (Parekh et al., 2008), 16 µatm(Tagliabue et al., 2009c), 25 µatm (Oka et al., 2011) and are thus a small part of the full glacial decrease in atmospheric CO_2 of ∼50 µatm prior to carbonate compensation, i.e. the burial of carbon as $CaCO_3$ in ocean sediments (Brovkin et al., 2007; Tagliabue et al., 2009c). Particularly the interactive limitation of the phytoplankton in the Southern Ocean by iron and light could produce a strong impact of dust deposition in our experiment LGM-ILL. Our new simulations suggest that dust deposition can have a larger impact on the biological carbon pump than suggested by recent studies, and thus could be a major factor contributing to the reduction of atmospheric CO_2 concentration during glacial times.

The difference of our simulated sensitivity of atmospheric CO_2 already in the NOILL simulations in comparison to other studies stems from differences in the residence time of dissolved iron at the surface. In the model we use, the equilibrium constant between free iron, ligands and their complexation ($KFeL = 1 \times 10^{11}$ to 5×10^{11} M^{-1}) is lower than in other models such as in (Tagliabue et al., 2009c) ($KFeL = 10^{12}$ M^{-1}). In addition, in the model we use, photodissociation of iron-ligand complexes reduces the equilibrium constant to the lower end of $KFeL = 1 \times 10^{11}$ to 5×10^{11} M^{-1} at the surface. The low equilibrium constant at the surface leads to fast iron scavenging and a short residence time of dissolved iron. The dissolved iron concentrations rely much more on external sources because of the low background concentrations. A further factor reducing the background concentration is the neglect of a hydrothermal source of dissolved iron in our model configuration - although the link of this iron source to biological productivity in the surface ocean has been argued to be negligible (Tagliabue et al., 2014a). The response of the bio-

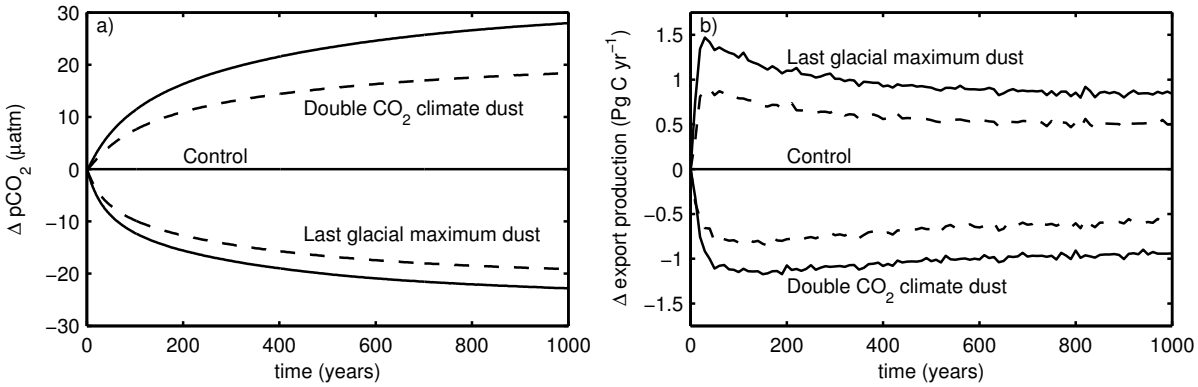

Figure 2.3: Change of a) atmospheric CO_2 concentration for the 2xCO_2 dust deposition (upper lines) and for the LGM dust deposition (lower lines) and b) globally integrated export production (at 100 dbar) relative to the control simulation for the LGM dust deposition (upper lines) and for the 2xCO_2 dust deposition (lower lines). Dashed lines are runs without the dependence of light harvesting capabilites on iron, solid lines are runs with considering the effect of iron on light harvesting capabilities.

logical pump to changes in iron supply is hence much stronger than with a long residence time of dissolved iron at the surface. For a better estimate of how the oceanic CO_2-uptake changes with a varying degree of iron limitation of phytoplankton, the residence time of iron in surface water needs to be better constrained in observational studies.

For predictions of future atmospheric CO_2 concentrations an estimation of the susceptibility of the ocean biogeochemistry to possible decreases in dust deposition in a warmer and wetter climate is necessary (Mahowald et al., 2006, 2010). Accounting for the iron limitation of light harvesting capabilities at low dust deposition leads to an extra increase of atmospheric CO_2 by 9.6 µatm in experiment 2xCO_2-ILL compared to experiment 2xCO_2-NOILL. This makes up for 32 % of the total response of 28.0 µatm and is around twice the CO_2 increase estimated by previous studies. In the modeling study by Tagliabue et al. (2014a) shutting the dust deposition off completely leads to a slight increase of the atmospheric CO_2 concentration by 2 ppmv. Another modeling study with a different model simulated an increase of 14 µatm by reducing current dust deposition by half (Parekh et al., 2006). Based on observations of interactions between iron and light limitation in incubation experiments and culture studies (Greene et al., 1991; Davey and Geider, 2001; Hopkinson et al., 2007; Moore et al., 2007; Hopkinson and Barbeau, 2008) our global model results show that a decrease in dust deposition could lead to a larger decrease in future oceanic CO_2 uptake than estimated previously.

The globally integrated export production shows a strong response to the changes in dust deposition particularly during the first 100 years of the experiments (Figure 2.3b). The fluctuations on shorter time scales stem from fluctuations in sea ice coverage and are mediated to export production by affecting the irradiance reaching the ocean surface. In the

case of the LGM dust, excess macronutrients are taken up and in the case of the 2xCO_2 dust, excess iron is taken up during the first 100 years until in the end global export production equilibrates at a higher (+0.86 Pg C yr^{-1} at 100 dbar) or lower level (-0.94 Pg C yr^{-1} at 100 dbar) relative to the control simulation, respectively. At the end of the simulations the difference in the response of export production between applying and not applying the iron limitation of light harvesting capabilities of phytoplankton is 0.36 Pg C yr^{-1} at 100 dbar in the case of LGM dust and 0.35 Pg C yr^{-1} at 100 dbar in the case of 2xCO_2 dust and thus very pronounced on the globally integrated scale (compare also Supplementary Table S1). The iron limitation of light harvesting capabilities has thus a strong control on the sensitivity of simulated global export production and atmospheric CO_2 concentrations to the supply of iron to the surface ocean.
The regional difference between the experiments with and without consideration of the impact of iron on light harvesting capabilities (LGM-ILL minus LGM-NOILL) reveals that, in comparison to the LGM-NOILL experiment, export production is particularly increased in the North Pacific, the North Atlantic and the Southern Ocean (Figure 2.4). Accordingly, surface phosphate concentrations are reduced in these regions. The reason for that is that due to the consideration of iron-light colimitation, growth rates are increased the most at low light (not saturated) levels which leads to the strongest response to iron addition in areas with light limitation (Figure 2.1). In contrast, in the 2xCO_2-ILL experiment the effect of iron limitation is enhanced so that carbon export is generally reduced, particularly in the northern subtropical Pacific for which a large decline in dust deposition is predicted under global warming (Figure 2.4). With export production being reduced under 2xCO2, more macronutrients are left unutilized in these regions and can be transported into the more oligotrophic subtropical gyres, where export production can thus increase in the 2xCO2 scenario.

2.4 Conclusions

Iron-light colimitation is, in contrast to colimitation of, for example, nitrogen and phosphorus, biochemically dependent in that iron is needed for light harvesting antennae and enzymes in the electron transport (Saito et al., 2008). We show that our model has a higher sensitivity to changes in dust deposition than earlier models and that the direct effect of iron concentrations on light harvesting capabilities of phytoplankton further enhances the model sensitivity to changes in dust deposition. Decreasing dust deposition could decrease oceanic CO_2 uptake, by a larger amount than suggested previously. Furthermore, we show that the CO_2 uptake triggered by LGM dust is up to twice as large in our simulations than estimated before. We suggest that the consideration of the effect of iron on light harvesting has a strong impact on the response of the ocean biogeochem-

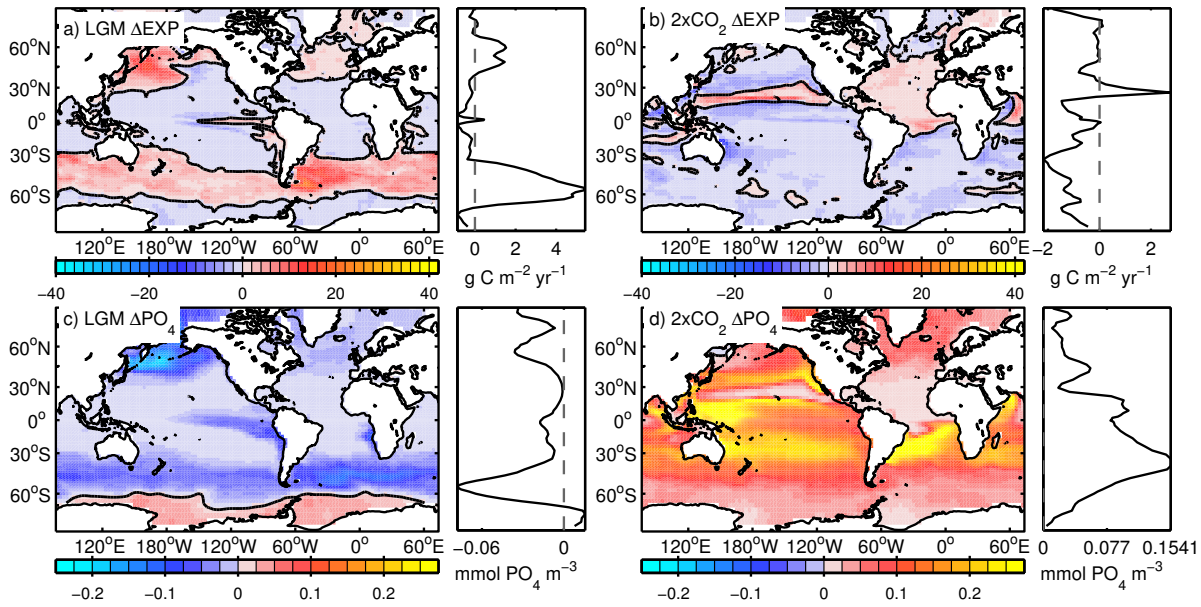

Figure 2.4: Difference between the simulations with and without considering the effect of iron on light harvesting in export production at 100 dbar (g C m^{-2} yr^{-1}) (first row) and in surface phosphate concentrations (mmol m^{-3}) (second row). The left column shows the results using the LGM dust and the right column the results using the 2xCO_2 dust. The zonal mean is displayed right to each map.

istry to dust deposition. The influence of iron on light harvesting increases the response of atmospheric CO_2 to dust deposition by 19 % of the total response for the LGM dust deposition and 32 % for the 2xCO_2 dust deposition. Due to the importance of this mechanism, more observational and experimental constraints on iron limitation and colimitation with other nutrients and factors are needed for accurate reconstructions of the past climate and prediction of the future. Small details of nutrient limitation of phytoplankton could have large effects of the oceanic response to changes in dust deposition.

Acknowledgements We acknowledge financial support from the Deutsche Forschungsgemeinschaft (SFB 754) and thank two anonymous reviewers for their constructive comments and suggestions for improvement. We thank Natalie Mahowald (Cornell University, Ithaca, USA) for sharing the dust deposition estimates, Eric Galbraith (McGill University, Montreal, Canada) and Heiner Dietze (GEOMAR, Kiel, Germany) for helpful discussions, advice and technical support. The model data used to generate the figures will be available at `http://thredds.geomar.de/thredds/catalog_open_access.html`.

3 A dynamic marine iron cycle module coupled to the University of Victoria Earth System Model: The Kiel Marine Biogeochemical Model 2 (KMBM2) for UVic 2.9

This chapter is based on the paper "A dynamic marine iron cycle module coupled to the University of Victoria Earth System Model: the Kiel Marine Biogeochemical Model 2 (KMBM2) for UVic 2.9 " published as a discussion paper in Geoscientific Model Development Discussions and accepted for a peer-reviewed publication in the journal Geoscientific Model Development.
Nickelsen, L., Keller, D., and Oschlies, A. (2014). A dynamic marine iron cycle module coupled to the University of Victoria Earth System Model: the Kiel Marine Biogeochemical Model 2 (KMBM2) for UVic 2.9. Geoscientific Model Development, accepted.

Abstract Marine biological production and the associated biotic uptake of carbon in many ocean regions depend on the availability of nutrients in the euphotic zone. While large areas are limited by nitrogen and/or phosphorus, the micronutrient iron is considered the main limiting nutrient in the North Pacific, equatorial Pacific and Southern Ocean. Changes in iron availability via changes in atmospheric dust input are discussed to play an important role in glacial/interglacial cycles via climate feedbacks caused by changes in biological ocean carbon sequestration. Although many aspects of the iron cycle remain unknown, its incorporation into marine biogeochemical models is needed to test our current understanding and better constrain its role in the Earth system. In the University of Victoria Earth System Climate Model (UVic) iron limitation in the ocean was, until now, simulated pragmatically with an iron concentration masking scheme that did not allow a consistent interactive response to perturbations of ocean biogeochemistry or iron cycling sensitivity studies. Here, we replace the iron masking scheme with a dynamic iron cycle and compare the results to available observations and the previous marine biogeochemical model. Sensitivity studies are also conducted with the new model to test the sensitivity of the model to parameterized iron ligand concentrations, the importance of considering the variable solubility of iron in dust deposition, the importance of considering high resolution bathymetry for the sediment release of iron, the effect of scaling the sedimentary iron release with temperature and the sensitivity of the iron cycle to a climate change scenario.

3.1 Introduction

The Earth system consists of three major components: ocean, atmosphere and land. All of them interact and shape the Earth's climate. Understanding the most important dynamics and the way they influence the climate is an urgent task because of mankind's dependence on, and increasing interference with, the climate of our planet. The ocean is a particularly important component of the Earth system since it has the capacity to compensate for large fluctuations of the greenhouse gas CO_2 in the atmosphere. For instance, Sabine et al. (2004) estimated that the global oceanic anthropogenic CO_2 sink for the period from 1800 to 1994 accounts for 48 % of the total fossil-fuel and cement-manufacturing emissions. The oceanic uptake of anthropogenic carbon is thought to have, until now, occurred predominantly through the solubility pump, which describes the physical dissolution of CO_2 in sea water, a strongly temperature dependent process with more CO_2 being absorbed into cold, high latitude waters that sink into the ocean interior. So far, there is little evidence for changes in the so-called biological pump that transfers carbon from the surface ocean via phytoplankton uptake and sinking of organic matter to the deeper ocean. The biological pump does, however, have a huge potential to affect the partitioning of carbon between the ocean and the atmosphere. Its strength in many regions depends on nutrient limitation of phytoplankton so that ocean biogeochemistry has an influence on the global carbon cycle and climate.

Over the last two decades iron has been discovered to play an important role in ocean biogeochemistry. The availability of iron limits phytoplankton growth in the North Pacific, equatorial Pacific and Southern Ocean (Boyd and Ellwood, 2010). Dust deposition and more recently, sediment release of iron are seen as the major sources of iron to the ocean. Increases in Southern Ocean dust deposition are still discussed as possibly contributing to glacial/interglacial changes in atmospheric CO_2 concentrations by reducing Southern Ocean iron limitation (Martinez-Garcia et al., 2014). On the other hand, Tagliabue et al. (2014a) find in a modeling study that without sediment release of iron, the atmospheric CO_2 concentration would be 10.0–18.2 ppm higher. Furthermore, iron is particularly important for nitrogen fixing phytoplankton, so called diazotrophs that have a strong impact on the balance of the ocean nitrogen inventory (Mills et al., 2004; Moore and Doney, 2007; Somes et al., 2010). Thus, the marine iron cycle is an important part of the Earth system.

Earth system models are well suited for investigating the dynamics and sensitivities of the earth system to perturbations. However, Earth system and global ocean-only models have usually incorporated representations of the iron cycle with a varying degree of com-

plexity (Moore and Braucher, 2008; Parekh et al., 2008; Tagliabue et al., 2014a). A low level of complexity is useful for example, for investigating the sensitivity of oceanic CO_2 uptake to dust deposition or for comparing the role of sedimentary iron release to that of aeolian iron deposition. However, these models can have quite different sensitivities and a comparison of the models and their assumptions can indicate the reasons for the different sensitivities (Tagliabue et al., 2008). More mechanistic models are needed to identify the important processes and their sensitivities to environmental changes, and to reduce uncertainties in the model simulations.

In the University of Victoria Earth System Climate Model (UVic), which we use in this study, iron limitation has either been ignored (Schmittner et al., 2008) or modeled with the use of an iron deposition mask (Somes et al., 2013) and of a non-dynamic iron masking scheme (Keller et al., 2012) that was based on iron concentrations calculated by another model (Galbraith et al., 2010), which contained a dynamic iron cycle. Thus, the iron concentrations in the most recent version of the marine biogeochemical component (Keller et al., 2012) are not interactive with the rest of the model. Furthermore, sensitivity studies and experiments that require dynamic feedbacks of the iron cycle from changes in biogeochemistry and physics cannot be carried out with a constant iron concentration mask. Here, we add a dynamic iron cycle to the UVic marine biogeochemical model to create the ability to investigate the iron cycle itself, the interactions of the iron cycle with other biogeochemical cycles and the climate. Our results indicate the importance of including the variable solubility of dust-deposited iron and the importance of the depth of sedimentary iron release to the water column. We also find that scaling the benthic iron release with temperature increases the agreement between simulated and observed iron concentrations in the Southern Ocean and a high sensitivity of dissolved iron concentrations to parameterized ligand concentrations. The new model allows us to provide an estimate of global marine iron fluxes and shows how implementing the dynamic iron cycle improves the agreement of simulated ocean tracers with observations. Finally, the dynamic response of the iron cycle during a climate change scenario simulation is demonstrated.

3.2 Model description

A dynamic iron cycle is added to the Kiel Marine Biogeochemical Model (KMBM) by Keller et al. (2012) and coupled to the UVic version 2.9 (Eby et al., 2009, 2013; Weaver et al., 2001). The UVic model and the ocean biogeochemical model are briefly outlined before the new dynamic iron cycle is described.

3.2.1 The University of Victoria Earth System Climate Model

The UVic model (Eby et al., 2009, 2013; Weaver et al., 2001) is an Earth system model of intermediate complexity (EMIC) with the advantage of relatively low computational costs. The model consists of three components: a simple one layer atmospheric model, a terrestrial model and a three dimensional ocean circulation model. The horizontal grid resolution of all model components is 3.6° in meridional and 1.8° in latitudinal direction. The atmospheric component is an energy-moisture balance model that dynamically calculates heat and water fluxes between the atmosphere and the ocean, land and sea ice. Advection of water vapor in the atmosphere is calculated using monthly climatological wind data from the National Center for Atmospheric Research/National Center for Environmental Prediction (NCAR/NCEP). The land vegetation model is the terrestrial model of vegetation and carbon cycles (Meissner et al., 2003) based on the Hadley Center model TRIFFID. Land processes are modelled via the MOSES1 land surface exchange scheme (Cox, 2001). Continental ice sheets are assumed to be constant in our model configuration. In contrast, sea-ice is calculated with a thermo-dynamic sea-ice model. The ocean component is the Modular Ocean Model 2 (MOM2) and consists of 19 vertical layers and, as with the atmospheric component, is forced by monthly climatological wind data from NCAR/NCEP. Subgrid-scale eddy mixing is parameterized according to Gent and Mcwilliams (1990), the vertical diffusivity parameter in the Southern Ocean is increased as in Keller et al. (2012), tidally induced diapycnal mixing over rough topography is computed according to the scheme by Simmons et al. (2004), and an anisotropic viscosity scheme (Large et al., 2001) is applied in the tropics.

3.2.2 The marine biogeochemical model

The marine biogeochemical model used here was developed and extended by Oschlies and Garçon (1999), Schmittner et al. (2005), Schmittner et al. (2008) and Keller et al. (2012). The model is a NPZD type of model with nutrients, phytoplankton, zooplankton and detritus. Sources and sinks are described in the following and illustrated in Fig. 3.1a, for the full equations see Schmittner et al. (2008); Keller et al. (2012).

The model is nitrogen-based, but has two dissolved inorganic nutrient pools, nitrate (NO_3) and phosphate (PO_4). Redfield stoichiometry is used to convert the tracer mass into carbon, phosphorus, or oxygen when necessary. There are two types of phytoplankton, one of which represents nitrogen fixing phytoplankton types (diazotrophs, P_D). Since they can fix dinitrogen into bioavailable forms, these diazotrophs are not limited by nitrate concentrations. In contrast, the other phytoplankton class (P_O), which represents all non-nitrogen

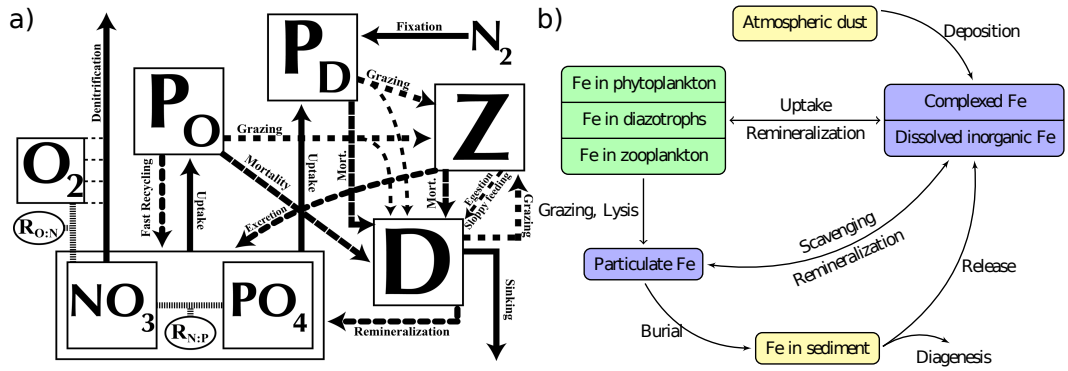

Figure 3.1: **(a)** Schematic of the previous ecosystem model, which did not include a dynamic iron cycle, illustrating the flux of material between model variables (reprinted from Fig. 1 Keller et al., 2012). **(b)** Schematic of the new iron cycle that is implemented into the previous model. Assuming that complexation and dissociation are very fast processes, the two new iron tracer are dissolved iron which is assumed to be bioavailable and particulate iron which is assumed to not be bioavailable. Yellow boxes indicate external reservoirs of iron, blue boxes not living iron species in the ocean and green boxes the living iron species in the ocean.

fixing phytoplankton, is limited by nitrate and phosphate. Microbial loop dynamics and dissolved organic matter cycling are parameterized via a fast recycling scheme that directly returns a fraction of phytoplankton into inorganic nutrients. Non-grazing related phytoplankton mortality also results in the production of detritus. Zooplankton (Z) graze on ordinary phytoplankton, diazotrophs, themselves and detritus (D). Growth and assimilation efficiency terms determine the fraction of prey biomass that is assimilated into biomass, respired, excreted or lost to detritus via sloppy feeding, egestion, and fecal pellet production. Zooplankton mortality also produces detritus. Detritus is considered as a tracer with horizontal advection and diffusion, but primarily sinks through the water column. A temperature-dependant function simulates microbial decomposition and remineralization to convert detritus back into inorganic nutrients and carbon. At the seafloor all detritus is instantly converted back into inorganic nutrients and carbon to simulate benthic decomposition and remineralization. During the remineralization of detritus, oxygen (O_2), which is also a dynamically calculated tracer, is consumed. When oxygen levels fall below a threshold of $5\,\mathrm{mmol\,m^{-3}}$, anaerobic remineratization sets in at rates 3 times slower than aerobic remineralization, and with associated nitrogen losses representing the combined effects of denitrification and anammox.

Using fixed Redfield ratios between carbon and nitrogen, dissolved inorganic carbon and alkalinity are also included in the model. For a more complete description of the biogeochemical model also see the complete model code in the Supplement or at `https://thredds.geomar.de/thredds/fileServer/peerReviewData/nickelsen-et-al_gmd_2014/`

`Nickelsen-et-al_GMD_2014_submitted.zip`.

3.2.3 The new dynamic iron cycle

The iron cycle described here (Fig. 3.1b) largely follows Parekh et al. (2004, 2005) and Galbraith et al. (2010). Sources and sinks of the modeled iron cycle are explained first with description of parameterizations for iron limitation, scavenging, remineralization, sediment release and dust deposition given in the subsequent sections.

Sources and sinks of iron

The iron cycle is simulated with the addition of two new physical tracers, dissolved iron (Fe) and particulate iron (Fe_P), to the marine biogeochemical model. The dissolved iron includes free iron and complexed iron, both of which are assumed to be entirely bioavailable.

The concentration of each tracer changes according to the following equation:

$$\frac{\partial C}{\partial t} = \mathrm{Tr} + S \tag{3.1}$$

where Tr denotes physical transport including advection, isopycnal and diapycnal diffusion. S represents the source minus sink terms. All dissolved iron (Fe) is assumed to be bioavailable whereas particulate iron (Fe_P) is not. Dissolved iron is taken up by phytoplankton and remineralized by grazing or microbial decomposition processes, biotically derived particulate iron is produced whenever organic detritus is produced. These biotic fluxes are calculated from the nitrogen-based rates using a fixed Fe : N ratio ($R_{\mathrm{Fe:N}}$) (Table 3.1). Observations indicate highly variable Fe : N ratios (Price, 2005), yet the usage of a fixed Fe : N ratio is a pragmatic choice that reduces computational costs as it circumvents the need to calculate iron concentrations within each biological tracer. The sources and sinks of the two additional iron tracers are described by:

$$\begin{aligned} S(Fe) = {} & R_{\mathrm{Fe:N}}(\mu_{\mathrm{P}} P_{\mathrm{O}} + (\gamma - \bar{\omega})(\mathrm{graz}_{\mathrm{P}} + \mathrm{graz}_{\mathrm{D}} + \mathrm{graz}_{\mathrm{Det}} + \mathrm{graz}_{\mathrm{Z}}) - J_{\mathrm{O}} P_{\mathrm{O}} - J_{\mathrm{D}} P_{\mathrm{D}}) \\ & + \mu_{Fe_P} - fe_{\mathrm{orgads}} - fe_{\mathrm{prp}} + fe_{\mathrm{sed}} + fe_{\mathrm{dust}} \end{aligned} \tag{3.2}$$

$$\begin{aligned} S(Fe_P) = {} & R_{\mathrm{Fe:N}}((1-\gamma)(\mathrm{graz}_{\mathrm{P}} + \mathrm{graz}_{\mathrm{D}} + \mathrm{graz}_{\mathrm{Det}} + \mathrm{graz}_{\mathrm{Z}}) + \mathrm{morp} + \mathrm{morp}_{\mathrm{D}} \\ & + \mathrm{morz} - \mathrm{graz}_{\mathrm{Det}}) - \mu_{Fe_P} + fe_{\mathrm{orgads}} + fe_{\mathrm{prp}} - w_{\mathrm{D}} \frac{\partial Fe_P}{\partial z} \end{aligned} \tag{3.3}$$

The first term in Eq. (3.2), ($\mu_{\mathrm{P}} P_{\mathrm{O}}$), is a temperature-dependent fast remineralization function that represents recycling of iron bound to phytoplankton-derived organic matter via the microbial loop and dissolved organic matter cycling. The second term represents iron

Table 3.1: Parameters that are new or different from Keller et al. (2012) with parameter name, description, value, range tested and unit. References for the parameters are given as footnotes. If no units are given in the reference column, reference units are equal to model units given in the last column.

Parameter	Description	Reference	Value	Tested Range	Unit
$\alpha^{\mathrm{chl}}_{\mathrm{min}}$	Minimum slope in the photosynthesis–irradiance curve	18.4–73.6 [a]	18.4	-	$\mu g\,C\,(g\,Chl)^{-1}\,(W\,m^{-2})^{-1}\,s^{-1}$
$\alpha^{\mathrm{chl}}_{\mathrm{max}}$	Maximum slope in the photosynthesis–irradiance curve	18.4–73.6 [a]	73.6	-	$\mu g\,C\,(g\,Chl)^{-1}\,(W\,m^{-2})^{-1}\,s^{-1}$
θ_{max}	Maximum Chl : C ratio, abundant iron	0.007–0.072 [a]	0.04	-	$g\,Chl\,(g\,C)^{-1}$
θ_{min}	Minimum Chl : C ratio, extreme iron limitation	0.007–0.072 [a]	0.01	-	$g\,Chl\,(g\,C)^{-1}$
kFe_{max}	Maximum half-saturation constant for iron uptake	0.19–1.14 [b]	0.4	0.3-0.4	$\mu mol\,Fe\,m^{-3}$
kFe_{min}	Minimum half-saturation constant for iron uptake	0.035 [c]	0.04	0.035-0.04	$\mu mol\,Fe\,m^{-3}$
P_{max}	Phytoplankton biomass above which *kFe* increases	0.15 [d]	0.15	0.1-0.15	$mmol\,N\,m^{-3}$
kFe_{D}	Diazotroph half-saturation constant for iron uptake	0.06 [e]	0.1	0.06-0.12	$\mu mol\,Fe\,m^{-3}$
$R_{\mathrm{Fe:N}}$	Fe : N uptake ratio	$5\,\mu mol\,Fe\,(mol\,C)^{-1}$ [f]	66.25	33.125-66.25	$\mu mol\,Fe\,(mol\,N)^{-1}$
L_{T}	Total ligand concentration	1 [g]	1	0.6-1.2	$\mu mol\,lig\,m^{-3}$
$Fe\ :\ P_{\mathrm{sed}}$	Fe : P ratio for sedimentary iron source	$0.072\,mol\,Fe\,(mol\,P)^{-1}$ [h]	0.004	0.001-0.01	$mol\,Fe\,(mol\,P)^{-1}$ at $0\,°C$
$KFeL$	Fe-ligand stability constant	10^{11}–10^{12} [i]	$10^{11.5}$	10^{11}-10^{12}	$(mol\,lig\,(l^{-1}))^{-1}$
kFe_{org}	Organic-matter dependent scavenging rate	0.5 [g]	0.45	0.45-0.5	$(g\,C)^{-0.58}\,(m^3)^{0.58}\,d^{-1}$
kFe_{prp}	Inorganic scavenging rate	0.003 [d]	0.005	0.003-0.005	d^{-1}
$O_{2\,\mathrm{min}}$	Minimum O_2 concentration for iron oxidation	5 [j]	5	0-5	$mmol\,O_2\,m^{-3}$

[a] (Geider et al., 1997), [b] (Timmermans et al., 2004), [c] (Price et al., 1994), [d] (Aumont and Bopp, 2006), [e] (Moore and Braucher, 2008), [f] (Johnson et al., 1997), [g] (Parekh et al., 2005), [h] (Elrod et al., 2004), [i] (Gledhill and Buck, 2012), [j] (Noffke et al., 2012)

excretion by zooplankton, which is calculated as the difference between their assimilation and growth efficiency coefficients ($\gamma - \bar{\omega}$) for the sum of all grazing on phytoplankton ($\mathrm{graz_P}$), diazotrophs ($\mathrm{graz_D}$), detritus ($\mathrm{graz_{Det}}$) and themselves ($\mathrm{graz_Z}$). The third and fourth terms represent the uptake of dissolved iron by ordinary phytoplankton and diazotrophs ($J_{\mathrm{O}}P_{\mathrm{O}}$,$J_{\mathrm{D}}P_{\mathrm{D}}$). The fifth term, ($\mu_{Fe_P}$), represents the temperature-dependent decomposition and remineralization of particle bound iron. The next two terms represent abiotic iron cycling, which is characterized by the loss of bioavailable, dissolved iron through scavenging. Scavenging is modeled here as two distinct processes: adsorption of iron to organic material (fe_{orgads}) and precipitation and colloidal formation with subsequent aggregation (fe_{prp}) described in detail below. The final two terms represent the external sources of iron that are added to the water column from sediment release (fe_{sed}) and dust deposition (fe_{dust}).

In Eq. (3.3) the biotic sources and sinks of particulate iron are equal to the sources and sinks of detritus (see Eq. (6) in Keller et al., 2012). Thus the first term, which is calculated as one minus the zooplankton assimilation efficiency ($1 - \gamma$) for the sum of all grazing (see coefficients above), represents the production of iron containing detritus from sloppy feeding, egestion, or fecal pellet release. The next three terms represent the production of iron containing detritus from the mortality of ordinary phytoplankton ($m_{P_{\mathrm{O}}}P_{\mathrm{O}}$), diazotrophs ($m_{P_{\mathrm{D}}}P_{\mathrm{D}}$) and zooplankton ($m_{\mathrm{Z}}Z^2$). The fifth term accounts for the removal of particle-bound iron by zooplankton grazing ($\mathrm{graz_{Det}}$). The sixth term, (μ_{Fe_P}), represents the loss of particulate iron due to temperature-dependent decomposition and remineralization. The next two terms represent the abiotic scavenging fluxes (fe_{orgads} and fe_{prp}) that add to the particulate iron pool. The final term, $w_{\mathrm{D}}\frac{\partial Fe_P}{\partial z}$, accounts for the ver-

tical sinking of particulate iron with a sinking speed w_{D} that increases linearly with depth (see Keller et al., 2012; Schmittner et al., 2008). Depending on the redox state of seafloor sediments, particulate iron that sinks to the bottom is either instantly remineralized or buried in the sediments (see Sect. 3.2.3).

Phytoplankton iron limitation

Iron limitations of ordinary and diazotrophic phytoplankton is described in terms of Monod functions as in Aumont and Bopp (2006). For ordinary phytoplankton the formulation of iron limitation is based on the observation that larger cells have higher iron half-saturation constants than smaller ones (Timmermans et al., 2004). As Aumont and Bopp (2006) we assume that an increase of phytoplankton biomass is mainly due to increases in cell size so that the half-saturation constant of iron limitation for ordinary phytoplankton varies with their biomass P_{O}:

$$P_1 = \min(P_{\mathrm{O}}, P_{\max}) \tag{3.4}$$

$$P_2 = \max(0, P_{\mathrm{O}} - P_{\max}) \tag{3.5}$$

$$\mathrm{kFe}_{\mathrm{O}} = \frac{\mathrm{kFe}_{\min} P_1 + \mathrm{kFe}_{\max} P_2}{P_1 + P_2} \tag{3.6}$$

The three parameters used for this formulation from Aumont and Bopp (2006) are the phytoplankton biomass above which the iron uptake half-saturation constant starts to increase, $P_{\max}$, and the minimum ($\mathrm{kFe}_{\min}$) and maximum iron uptake half saturation constants ($\mathrm{kFe}_{\max}$). The iron uptake half-saturation constant for diazotrophs ($\mathrm{kFe}_{\mathrm{D}}$) is set as a non-varying parameter to reduce the number of parameters and to reflect the stronger constraint that iron imposes on the growth of small, diazotrophic phytoplankton (Mills et al., 2004; Moore and Doney, 2007). Using these half-saturation constants, iron limitation variables ($\mathrm{felim}_{\mathrm{O}}$, $\mathrm{felim}_{\mathrm{D}}$) for both, ordinary and diazotrophic phytplankton are calculated:

$$\mathrm{felim}_{\mathrm{O}} = \frac{Fe}{\mathrm{kFe}_{\mathrm{O}} + Fe}, \tag{3.7}$$

$$\mathrm{felim}_{\mathrm{D}} = \frac{Fe}{\mathrm{kFe}_{\mathrm{D}} + Fe}. \tag{3.8}$$

Then as in Keller et al. (2012), these limiting variables are included in the calculation of the potential phytoplankton maximum growth rates to reflect the necessity of iron for photosynthesis, the reduction of nitrate to ammonium, and a number of other key cellular processes (Galbraith et al., 2010) (i.e., we assume that iron must be available

before photosynthesis or the uptake and utilisation of nitrogen and phosphate is possible).

$$J_{\mathrm{O}}^{\max} = a \exp(T/T_b)\mathrm{felim}_{\mathrm{O}} \tag{3.9}$$

$$J_{\mathrm{D}}^{\max} = c_{\mathrm{D}} \max(0, a \exp(T/T_b - 2.61)\mathrm{felim}_{\mathrm{D}}) \tag{3.10}$$

where the maximum growth at 0 °C is multiplied with an e-folding temperature dependence term T/T_b, which produces a temperature constrained growth rate curve that is identical to the Eppley curve (Eppley, 1972) except at very high ocean temperatures, and the iron limitation variable. As in Schmittner et al. (2008) and Keller et al. (2012) diazotroph growth is reduced by using a handicap c_{D} and a stronger temperature dependence so that growth is inhibited below 15 °C.

In addition to the constraints that iron limitation imposes on the maximum potential growth rate, iron is assumed to influence phytoplankton light harvesting capabilities. Phytoplankton light limited growth is basically calculated as in Keller et al. (2012) and Schmittner et al. (2008) using

$$J_{(\mathrm{O\ or\ D})I} = \frac{J_{(\mathrm{O\ or\ D})}^{\max} \alpha I}{\left[\left(J_{(\mathrm{O\ or\ D})}^{\max}\right)^2 + (\alpha I)^2\right]^{1/2}} \tag{3.11}$$

For the full calculation of the depth averaged light limitation with a triangular shaped diurnal irradiance cycle see Schmittner et al. (2009) and Keller et al. (2012). Here the Eq. (3.11) for light limited growth is modified following Galbraith et al. (2010) by making the initial slope of the photosynthesis irradiance curve α chlorophyll specific (α^{chl}) and making light limitation dependent on a Chl : C ratio θ. Both, α^{chl} and θ, are in turn dependent on iron concentrations. In this way the dependence of light harvesting capabilities and chlorophyll synthesis on iron concentrations as suggested by field and culture experiments (Hopkinson et al., 2007; Price, 2005) is represented in the model. Thus, the phytoplankton light limited growth becomes

$$J_{(\mathrm{O\ or\ D})I} = \frac{J_{(\mathrm{O\ or\ D})}^{\max} \alpha^{\mathrm{chl}} \theta_{(\mathrm{O\ or\ D})} I}{\left[\left(J_{(\mathrm{O\ or\ D})}^{\max}\right)^2 + \left(\alpha^{\mathrm{chl}} \theta_{(\mathrm{O\ or\ D})} I\right)^2\right]^{1/2}} \tag{3.12}$$

where $J^{\max}_{(\text{O or D})}$ are the maximum potential growth rates and I is irradiance. The realized Chl : C ratios $\theta_{(\text{O or D})}$ are calculated as

$$\theta_{\text{O}} = \theta_{\min} + (\theta_{\max} - \theta_{\min})\text{felim}_{\text{O}} \tag{3.13}$$

$$\theta_{\text{D}} = \theta_{\min} + (\theta_{\max} - \theta_{\min})\text{felim}_{\text{D}} \tag{3.14}$$

and the initial slope of the PI-curve as

$$\alpha^{\text{chl}}_{\text{O}} = \alpha^{\text{chl}}_{\min} + \left(\alpha^{\text{chl}}_{\max} - \alpha^{\text{chl}}_{\min}\right) \text{felim}_{\text{O}} \tag{3.15}$$

$$\alpha^{\text{chl}}_{\text{D}} = \alpha^{\text{chl}}_{\min} + \left(\alpha^{\text{chl}}_{\max} - \alpha^{\text{chl}}_{\min}\right) \text{felim}_{\text{D}} \tag{3.16}$$

The iron limitation variables $\text{felim}_{\text{O,D}}$ are used here to create a linear change between minimum and maximum parameter values following Galbraith et al. (2010). The impact of making α^{chl} and θ functions of iron concentrations is comprehensively described by Galbraith et al. (2010). They find that this formulation leads to an improved agreement with observations of surface phosphate concentrations and export production, a more pronounced seasonal cycle of primary production and a stronger phytoplankton growth limitation in the Southern Ocean.

Iron scavenging and remineralization

Scavenging, which converts dissolved iron into colloidal and particulate forms, is an important part of the marine iron cycle. Iron speciation determines whether iron is subject to scavenging or stays dissolved as an organic complex bound to an organic ligand. Since the association and dissociation of iron to ligands occurs on time scales < 1 day (Gledhill and Buck, 2012), we follow Parekh et al. (2004) in assuming that this process occurs rapidly enough so that a chemical equilibrium is reached between free iron, free ligands and organic iron complexes. Thus, we avoid the need to add computationally costly tracers for free ligands and organic iron complexes. As in Parekh et al. (2004) the concentration of free iron Fe_{prime} that is subject to scavenging can then be calculated from the following equations assuming a chemical equilibrium between free iron, free ligands and organic iron complexes.

$$L = FeL + L_{\text{prime}} \tag{3.17}$$

$$Fe = FeL + Fe_{\text{prime}} \tag{3.18}$$

$$K_{\text{FeL}} = \frac{FeL}{Fe_{\text{prime}} L_{\text{prime}}} \tag{3.19}$$

The total ligand concentration (L) is assumed to be a globally constant model parameter due to uncertainties in the sources and sinks and to lower numerical costs. Ligand bound iron is denoted by FeL, the free ligand concentration by L_{prime}, the total dissolved iron concentration by Fe and the equilibrium constant between free iron and ligands and the organic complexes by K_{FeL}. Solving for Fe_{prime} gives

$$Fe_{\mathrm{prime}} = \frac{-A + (A^2 + 4K_{\mathrm{FeL}}Fe)^{0.5}}{2K_{\mathrm{FeL}}}, \tag{3.20}$$

$$A = 1 + K_{\mathrm{FeL}}(L - Fe), \tag{3.21}$$

where the equilibrium constant K_{FeL} is considered a globally constant parameter whose value is based on a compilation by Gledhill and Buck (2012).

Once Fe_{prime} is known, scavenging can be calculated. The first scavenging process is the adsorption of free dissolved inorganic iron onto organic material. Following Parekh et al. (2005) and Galbraith et al. (2010) and based on the observations by Honeyman et al. (1988), the adsorption rate in the model (fe_{orgads}) is dependent on the particulate organic matter concentration Detr, the concentration of free iron Fe_{prime} and the scavenging rate $\mathrm{kFe}_{\mathrm{org}}$.

$$fe_{\mathrm{orgads}} = \mathrm{kFe}_{\mathrm{org}}\mathrm{kFe}_{\mathrm{prime}}\left(\mathrm{Detr}R_{\mathrm{C:N}}M_{\mathrm{C}}\right)^{0.58} \tag{3.22}$$

The carbon to nitrogen ratio is denoted by $R_{\mathrm{C:N}}$ and the molar mass of carbon by $M_{\mathrm{C}} = 12.011\,\mathrm{g\,mol^{-1}}$ In the second scavenging process (fe_{prp}), iron precipitates and forms colloids which can subsequently aggregate into larger particles. This more inorganic process is represented in the model using a linear scavenging rate that is independent of the organic particle concentration:

$$fe_{\mathrm{prp}} = \mathrm{kFe}_{\mathrm{prp}}Fe_{\mathrm{prime}} \tag{3.23}$$

The scavenging rate constant for precipitation, colloid formation and aggregation is denoted by $\mathrm{kFe}_{\mathrm{prp}}$. Both scavenging rates are set to zero when oxygen concentrations fall below a threshold $O_{2\mathrm{min}}$ (Table 3.1) as in the model by Galbraith et al. (2010) because iron oxidation rates are reduced and elevated iron concentrations are repeatedly observed under low oxygen concentrations (Hopkinson and Barbeau, 2007; Moffett et al., 2007; Rijkenberg et al., 2012). However, the threshold assumption is a pragmatic choice and there is still uncertainty in the impact of the reduced iron oxidation rates (Hopkinson and Barbeau, 2007). We therefore test the threshold assumption by running an additional

1000 year simulation in which scavenging is permitted when oxygen levels fall below $O_{2\min}$. The effect is small and might be important only locally.

Remineralization and sinking of particulate iron is proportional to that of particulate nitrogen (e.g., detritus). Thus, the temperature dependent remineralization rate is calculated as

$$\mu_{Fe_P} = \mu_{\mathrm{d}0} \exp(T/T_b) Fe_{\mathrm{P}} \tag{3.24}$$

where $\mu_{\mathrm{d}0}$ is the remineralization rate parameter for both particulate iron and particulate organic nitrogen at zero degrees C.

Sediment iron cycling

Observations of iron release or burial in sediments have shown that these processes are dependent on the sediment redox state, which is primarily determined by the oxygen content of the overlying water column (Noffke et al., 2012; Severmann et al., 2010), the ambient temperature (Arnosti et al., 1998; Sanz-Lázaro et al., 2011) and the amount of organic matter that reaches the sea floor and is remineralized therein (Elrod et al., 2004).

Here we follow the model of Galbraith et al. (2010) to calculate the flux of iron from the sediment (fe_{sed}). Iron is released with a constant ratio ($Fe : P_{\mathrm{sed}}$) of iron to particulate organic phosphorus reaching the sediment (F_{POP}). Particulate iron that sinks out of the bottom ocean layer is permanently removed from the ocean, as long as oxygen concentrations are greater than the suboxic threshold $O_{2\min}$ (cf. diagenesis in Fig. 3.1b). However, if bottom water oxygen concentrations are below $O_{2\min}$, then the environment is assumed to be strongly reducing and all particulate iron sinking to the sediment (F_{Fe_P}) is released back into the water column, producing dissolved iron:

$$fe_{\mathrm{sed}} = Fe : P_{\mathrm{sed}} F_{\mathrm{POP}} \exp(T/T_b) \qquad (O_2 > O_{2\min}), \tag{3.25}$$

$$fe_{\mathrm{sed}} = Fe : P_{\mathrm{sed}} F_{\mathrm{POP}} \exp(T/T_b) + F_{Fe_P} \qquad (O_2 \leq O_{2\min}). \tag{3.26}$$

The ratio between iron released from the sediment and phosphorus in particulate matter that sinks into the sediment is denoted by $Fe : P_{\mathrm{sed}}$ and is based on the observation of such a constant ratio by Elrod et al. (2004). Note that their observation relies on measurements from the California coast that we have applied to the whole ocean here. We recognize that the relation can of course vary globally because of for instance different microbial communities and chemical environments. However, the relationship by Elrod

et al. (2004) is empirically based and formulated so that it allows the sediment source of iron to adjust when the amount of organic carbon supplied to the sediment changes. In some regions this may cause a feedback to occur since the released iron affects productivity and organic matter export, which in turn affects sediment iron release. This interactive response of the sediment source could be important in sensitivity studies.

Due to the observation of temperature dependent remineralization (Arnosti et al., 1998; Sanz-Lázaro et al., 2011), the importance of sediment release for the iron reservoir and an improvement of agreement between our simulated and observed iron concentrations particularly in the Southern Ocean, we assume that remineralization of iron in the sediment is temperature dependent by multiplying with a temperature dependent factor ($\exp(T/T_b)$ where $T_b = 15.65\,^{\circ}\mathrm{C}$). The average observed iron concentrations in the whole water column south of 40° S are 0.52 nM, simulated concentrations are 0.67 nM without and 0.53 nM with the temperature dependence. The assumption of temperature dependent iron release is tested and discussed further in Sect. 3.4. Riverine sources of iron are scavenged quickly at river mouths so that they are not viewed as an important source of iron to the ocean. Yet, the scavenged iron from rivers can reach the sediment and under low bottom water oxygen concentrations are released again as dissolved iron to the water column (Severmann et al., 2010). Eq. (5.2) allows that locally, i.e. under bottom water oxygen concentrations smaller than $O_{2\min}$, more iron can be released from the sediment than reaches it to reflect the massive iron release under low bottom water oxygen concentrations (Noffke et al., 2012) and implicitly also representing the riverine source of iron to the sediment.

The importance of the sedimentary iron sources for surface ocean biogeochemical cycling has been emphasized in previous observational (Noffke et al., 2012) and modeling studies (Moore and Braucher, 2008; Tagliabue et al., 2009a). However, in coarse resolution three dimensional ocean circulation models the bathymetry defined by the lowest grid boxes can strongly differ from the actual bathymetry of the ocean and with that the depth at which transfers between sediment and water column occur. Thus, a subgrid-scale bathymetry is applied as in Aumont and Bopp (2006); Moore and Braucher (2008); Somes et al. (2013) where the model bathymetry is compared to a bathymetry dataset, here ETOPO2v2 (U.S. Dept. of Commerce et al., 2006). For each horizontal grid point and at each depth level the fraction of the bottom area of the model box that is actually ocean floor within this box is calculated. This fraction determines then the fraction of organic matter that is treated as if it hits the sea floor. The resulting sediment flux of iron is illustrated in Fig. 3.2. The role of the sediment fluxes for the iron cycle will also

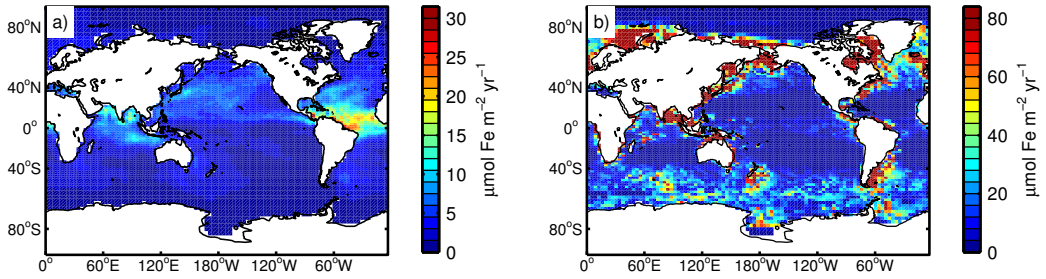

Figure 3.2: Annually averaged atmospheric deposition and sediment release of iron. **(a)** A preindustrial estimate of climatogical annually averaged dust deposition (Luo et al., 2008). **(b)** Sedimentary iron release as simulated with the model according to Eqs. (5.1) and (5.2). Note the different color scales.

be investigated further in a subsequent study.

Dust deposition of iron

An important source of iron in the open ocean comes from the deposition of iron-containing dust (Mahowald et al., 2009). The dust is eroded in arid terrestrial areas as for example the Sahara or some parts of Australia and then transported in the atmosphere to eventually be deposited in the ocean. We simulate this source of iron using a climatogical preindustrial estimate of monthly iron deposition (Luo et al., 2008). This estimate of iron deposition is derived from an atmospheric model that simulates the transport of dust in the atmosphere (Luo et al., 2008). During the transport in the atmosphere Luo et al. (2008) assume a constant 3.5 % fraction of iron in dust and that the solubility of iron increases due to reduction of Fe(III) to Fe(II) in acidic clouds. They can reproduce the observation of generally lower iron solubility at areas of high dust deposition and higher solubility at low dust deposition (Baker and Croot, 2010). Other estimates of total iron deposition of 56.7 Gmol Fe yr^{-1} (Mahowald et al., 2006) or 29.3 Gmol Fe yr^{-1} (Mahowald et al., 2010), assuming 3.5 % iron in dust and a globally constant 1 % solubility do not reproduce the solubility pattern and are thus considerably larger than the total iron deposition of 2.1 Gmol Fe yr^{-1} by Luo et al. (2008). At every ocean tracer time step we calculate the amount of iron that is deposited from the monthly values using linear interpolation (Fig. 3.2).

3.2.4 Parameter choices, spinup and assumptions

Only the parameters associated with the iron cycle are new (Table 3.1). All other parameters are as in Keller et al. (2012). Whenever possible model parameters were based on observed values or taken from previously evaluated modelling studies. For parameters that are poorly constrained, the parameters were chosen within an observed range

of values, if possible, to best simulate observed biogeochemical properties. In practice this involved varying the parameters individually, one by one, within the ranges given in (Table 3.1). The goal was to maximize agreement of surface macronutrients to observations and iron concentrations to the sparse observations while keeping the agreement of subsurface biogeochemical properties such as phosphate, nitrate and oxygen concentrations to observations similar to the agreement in the previous model version. Before the comparison to observations and the previous model version, the model was spun up for 10 000 years using preindustrial boundary conditions for insolation and a fixed atmospheric CO_2 concentration of 283 μatm

Here we summarize important assumptions that have been made to model the iron cycle. First, a fixed $Fe : N$ ratio is used for the biological state variables. This was done to minimize computational expenses and because the Fe stoichiometry of plankton is poorly constrained. Second, the ligand concentration is assumed to be globally constant since there are still a lot of uncertainties in the sources and sinks of iron-binding ligands (Völker and Tagliabue, 2014). Third, the sinking speeds of particulate nitrogen and iron are identical. Finally, the only two external sources of iron to the ocean that are considered are dust deposition and sediment release because other sources have been shown to be of minor importance (Tagliabue et al., 2014a). All of these assumptions are made to keep the computational costs low, which is necessary for long-term model runs such as paleo simulations or running multiple sensitivity tests to equilibrium (e.g. to keep the model as an EMIC). This is also the reason why the iron cycle is described with only two model tracers, dissolved and particulate iron. Due to the low number of parameters relative to other more complex models, the model also relies on less unconstrained parameters and has a smaller degree of freedom.

3.3 Model evaluation

The evaluation in this section focuses exclusively on the iron cycle and the other biogeochemical properties of the model because the physical (Weaver et al., 2001) and terrestrial components (Meissner et al., 2003) have been evaluated in detail in previous studies. Comparisons to the World Ocean Atlas 2009 (WOA09) (Garcia et al., 2010b,a), and Global Data Analysis Project (GLODAP) (Key et al., 2004) and an iron concentration compilation database (Tagliabue et al., 2012) allow us to evaluate the performance of the model in terms of agreement to observations. The model is also compared to the previous model version of Keller et al. (2012) to identify the changes that result from including a dynamic iron cycle.

3.3.1 The iron cycle

The new model with a dynamic iron cycle allows us to provide an estimate of global marine iron fluxes between major biogeochemical pools (Fig. 3.3). With the deposition forcing from Luo et al. (2008) the atmospheric iron deposition is a source of 2.1 Gmol Fe yr^{-1} to the ocean. Sedimentary iron release is one order of magnitude higher than iron deposition on the global scale, confirming the important role of the sediment in supplying iron to the ocean as already suggested by prior studies (Moore and Braucher, 2008; Tagliabue et al., 2009a). The sediment release of 18.8 Gmol yr^{-1} in our model is however still smaller than the 32.5 Gmol yr^{-1} of Misumi et al. (2014). Sixty three percent of the iron that is taken up by phytoplankton is recycled back to the dissolved iron pool. This compares well with observations of a large proportion of recycled to new iron sources (Boyd and Ellwood, 2010). The largest simulated flux is scavenging, which is even slightly larger than the remineralization of iron. Although some of the parameters are poorly constrained and, hence, there is some uncertainty in the magnitude of the fluxes, these results emphasize the difference between the iron cycle and macronutrient cycles since the residence time of iron in the ocean as computed from global inventory divided by global iron supply, which results to approximately 38 years here, is orders of magnitude shorter than the millennial residence time scales of the macronutrients nitrogen or phosphorus (Wallmann, 2010; Somes et al., 2013). This indicates that iron concentrations must be strongly dependent on local or regional sources. Our estimate of the iron residence time is within the range of other estimates of 12 years (Moore and Braucher, 2008) and 100 to 200 years (Boyd and Ellwood, 2010). The short residence time illustrates the potentially large leverage that changes in the Fe supply could have on marine biogeochemical cycles.

In comparison to the iron concentration mask used in the previous model version, the dynamically simulated surface iron concentrations in the new model are generally higher (Fig. 3.4). The average surface iron concentrations are 0.19 nM for the concentration mask and 0.41 nM for the new model. This is due to the higher stability constant of iron ligand complexes of $\log(KFeL) = 11.5$ here compared to the values of 9.8 to 10.8 used in the model of Galbraith et al. (2010), from which the iron mask in Keller et al. (2012) had been taken. Our choice is more in line with recent observational estimates of $\log(KFeL)$ being in the range of 11–12 (Gledhill and Buck, 2012). An additional factor could be the linear dependence of inorganic scavenging on free iron concentrations in the model presented here (cf. Eq. 3.23) which differs from the scaled (to the power of 1.5) inorganic scavenging of free iron in the model of Galbraith et al. (2010). Since our new formulation results in less scavenging the surface iron concentrations are slightly overestimated in the subtropical North Pacific, the tropical Atlantic and possibly the Indian Ocean as well as

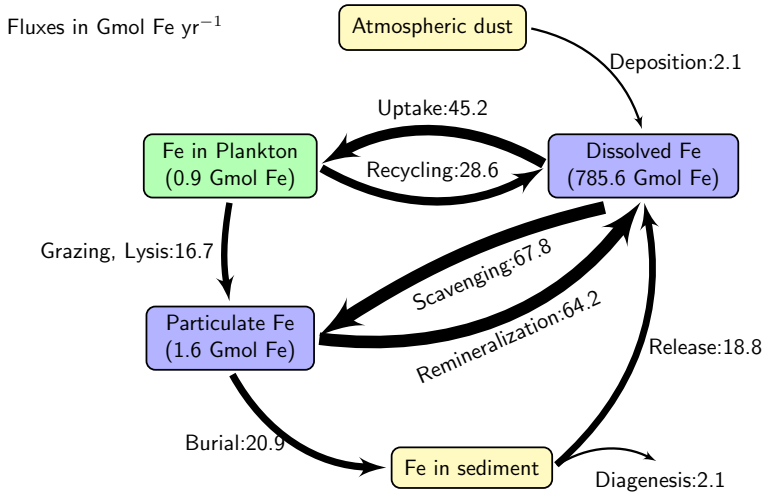

Figure 3.3: Global annually averaged iron fluxes as simulated with the dynamic iron cycle in the UVic model in Gmol Fe yr^{-1}. Arrow thickness is scaled with the size of the fluxes. The numbers inside the boxes denote the globally integrated amounts of iron in the respective pools in Gmol Fe.

the Arctic Ocean. However, the global root mean square error (RMSE), relative to observed surface iron concentrations (Tagliabue et al., 2012), decreases from 0.81 to 0.69 nM when compared to the surface iron concentrations of the iron concentration mask used by Keller et al. (2012), e.g., the regridded results of the BLING model (Galbraith et al., 2010).

The simulated zonal mean iron concentrations reveal that the iron concentrations in the Southern Ocean are probably a little too high, particular in the Pacific (Fig. 3.5). The average simulated concentration in the Southern Ocean is 0.53 nM and the observed value 0.56 nM, but in the Pacific sector the average simulated concentration is 0.56 nM opposed to the observed 0.33 nM. However, the model does capture the high iron concentrations that have been observed in the northern Indian Ocean, as well as elevated iron concentrations in the North Pacific and North Atlantic. The highest observed dissolved iron concentrations of up to 1.5 nM can not be represented by the model because of the globally constant ligand concentration of 1 nM which is probably too low in the regions of high iron concentrations (Gledhill and Buck, 2012).

The deviation of the profile of dissolved iron to the observations (Fig. 5.2) could be due to the constant and maybe too low ligand concentration assumed in the model and supports the notion that there is still no comprehensive understanding of sources and sinks of ligands although some promising approaches are emerging (Tagliabue and Völker, 2011; Misumi et al., 2013; Völker and Tagliabue, 2014). The observations also indicate that the simulated ferricline should be deeper than the nutricline (Fig. 5.2) (Tagliabue et al., 2014b). The other model tracers shown in Fig. 5.2 are discussed in the next section.

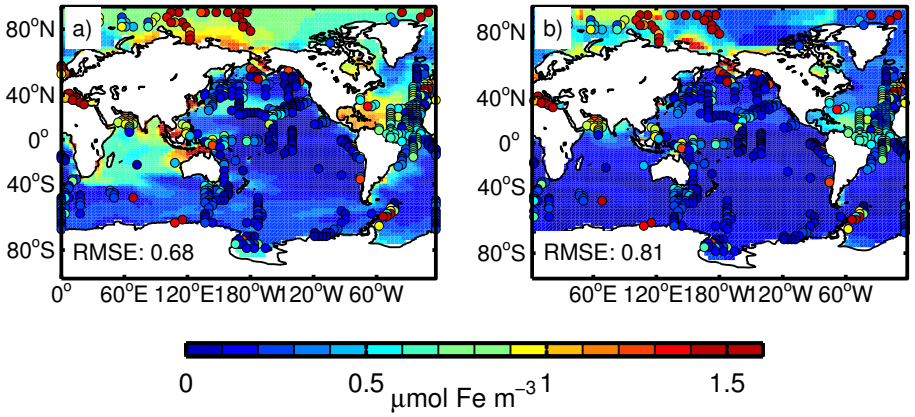

Figure 3.4: Annual mean surface iron concentrations **(a)** as simulated with the new model and **(b)** from the iron concentration mask used in the previous model version from Galbraith et al. (2010). Observations compiled by Tagliabue et al. (2012) are averaged over the first 50 m and plotted as colored circles on top.

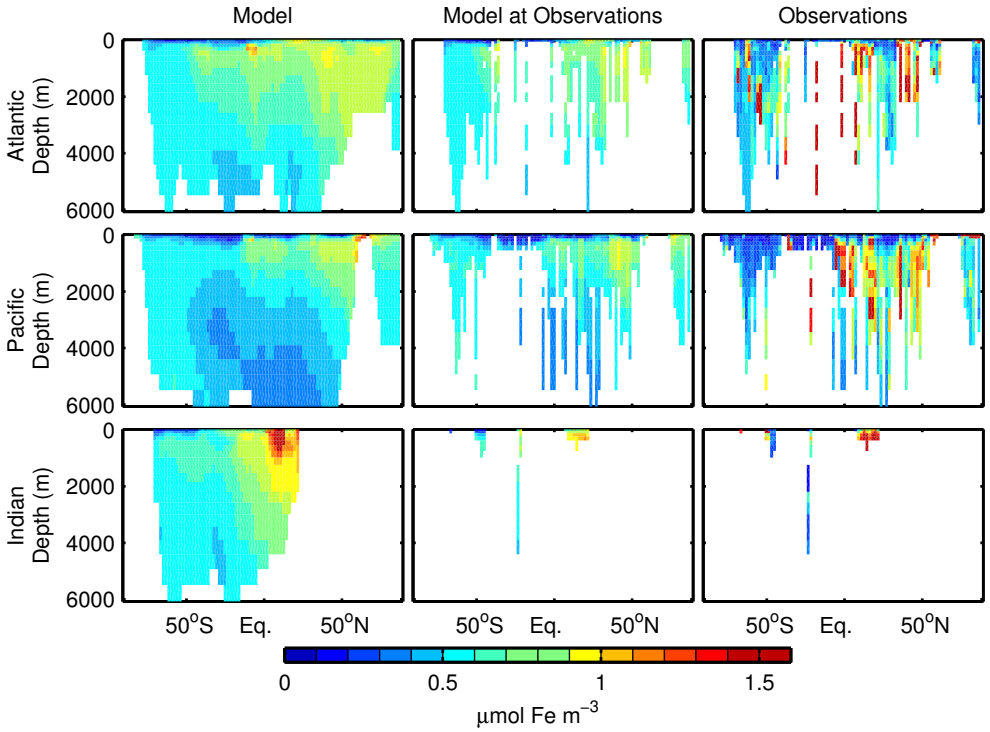

Figure 3.5: Zonal annual mean iron concentrations as simulated with the model (left column), model results averaged only at the locations of the observations (Tagliabue et al., 2012) (middle column) and observations (right column) for the different ocean basins.

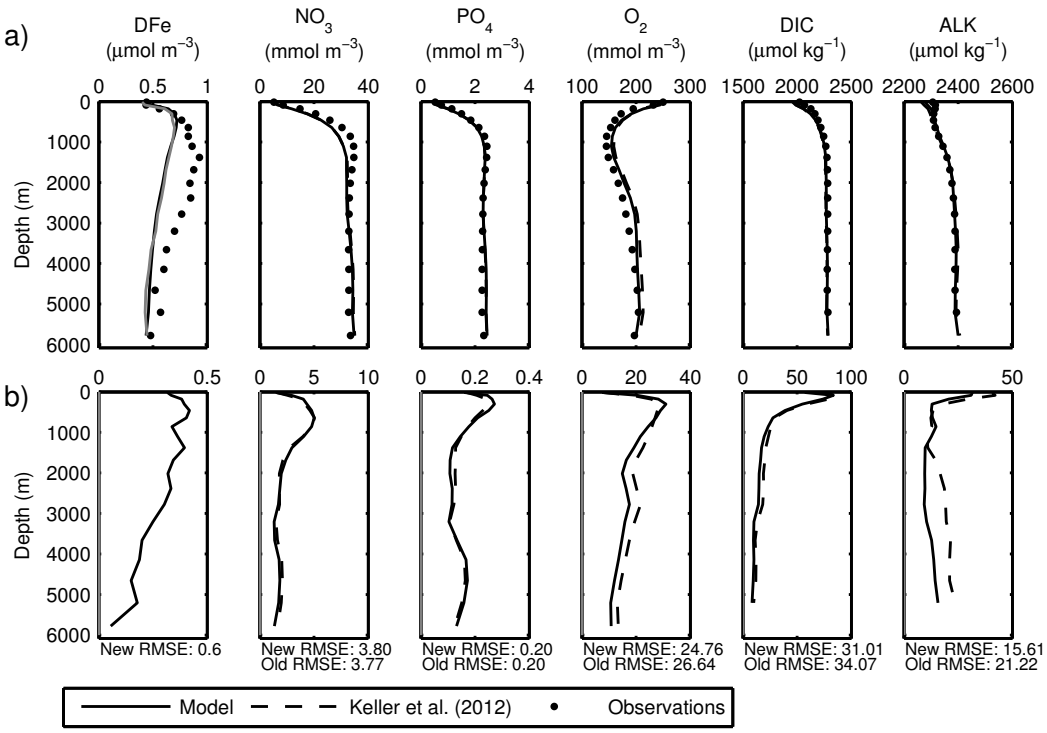

Figure 3.6: Vertical profiles comparing dissolved iron (DFe), nitrate (NO_3), phosphate (PO_4), oxygen (O_2), dissolved inorganic carbon (DIC) and alkalinity (ALK) with observations from Tagliabue et al. (2012), the World Ocean Atlas 2009 and GLODAP **(a)** and vertical profiles of the horizontally averaged absolute differences between model and the observations **(b)**. The gray line in the profile of dissolved iron is the horizontal average of simulated iron concentrations at the locations of the observations. The global root mean square errors (RMSE) relative to the observations are given below the respective panels in **(b)**.

Simulated surface iron concentration show a seasonal variability that appears somewhat smaller than can be inferred from the available data (Fig. 3.7). In the Northern Hemisphere simulated iron concentrations between 40 and 60° N start to get depleted in April. This is associated with the spring and summer bloom in the Northern Hemisphere. At the same time iron concentrations in the Southern Ocean start to increase showing that, as also stated by Tagliabue et al. (2014b), supply of iron to the surface from the deeper ocean during austral winter is an important source of iron.

In summary, the new dynamic iron cycle model allows identification of the important fluxes between the iron pools, indicates that more research is needed on ligand dynamics and shows a clear improvement over the iron concentration masking approach that was used previously with UVic. In comparison to the model by Misumi et al. (2013), who also compare their simulated iron concentrations to the full dataset by Tagliabue et al. (2012) and calculated a RMSE of 0.78 nM at the surface (0–200 m) and 0.86 nM in the

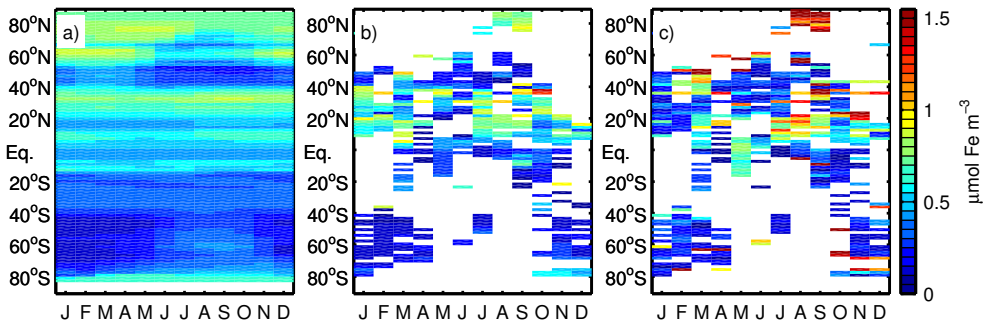

Figure 3.7: Zonal mean iron concentrations at the ocean surface plotted over time (Hovmöller diagram) as simulated with the model **(a)**, model results averaged only at the locations of the observations (Tagliabue et al., 2012) **(b)** and the observations **(c)**.

deep (200–5000 m) ocean, we get lower RMSEs of 0.58 nM at the surface (0–240 m) and 0.61 nM for the deep (240–5000 m) ocean.

One difficulty that we faced in evaluation of our results is that the observations of iron concentrations are still sparse and show high variability. The observed concentrations in the Southern Ocean are biased towards concentrations in the austral summer due to easier sampling at that time of the year (Tagliabue et al., 2012). Other limitations also have to be noted. Some regions are only poorly covered as for example the open Indian Ocean. Calculating root mean square errors and averaging over regions or depths will thus be biased towards strongly sampled regions. Different filter pore sizes of 0.2 to 0.4 µm during the measurements include different proportions of colloidal and soluble iron and produce some uncertainty in the dissolved iron observations. Additionally, the observations cover a long time span with different measurement techniques which reduces systematic bias but also adds to the uncertainty (Tagliabue et al., 2012). However, the database of dissolved iron observations is the best possibility to evaluate model results and the increasing number of measurements are highly valuable for the validation of models of the iron cycle and will improve this possibility in the future.

3.3.2 Biogeochemical validation

Having a dynamic iron cycle induces changes in all other simulated biogeochemical properties. Here we compare the biogeochemical results of these new simulations to the observations and previous model and discuss the reasons for them.

In comparison to the previous model version, surface PO_4 and NO_3 in the Southern Ocean are slightly lower (by on average 0.05 and 1.3 mmol m^{-3}, respectively) due to the higher iron concentrations and reduced Fe limitation (Fig. 5.3). In the equatorial Pacific the PO_4 concentrations are higher in the subtropical gyres, which are the regions where

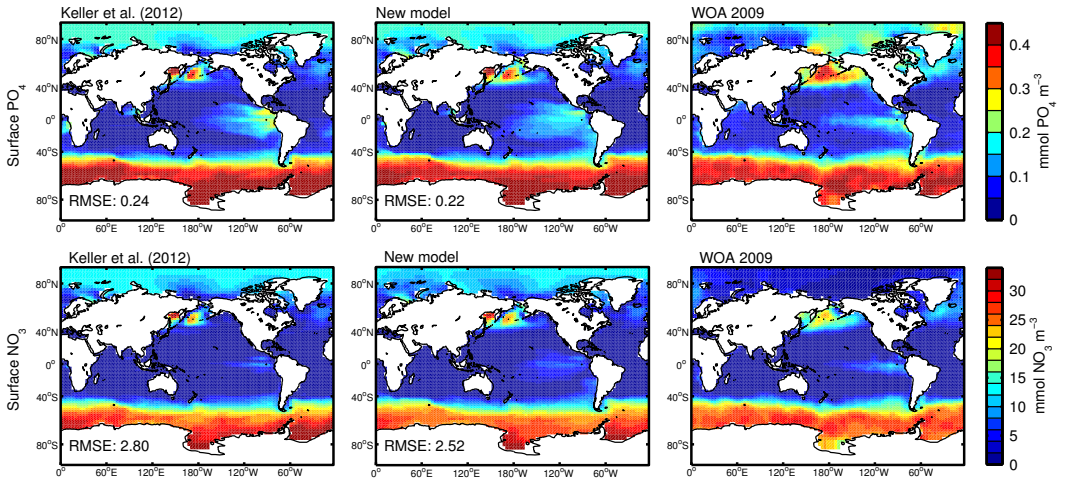

Figure 3.8: Annual mean surface phosphate (first row) and nitrate concentrations (second row) for the model by Keller et al. (2012) and the new model in comparison to observations from the World Ocean Atlas 2009 (WOA, 2009) (Garcia et al., 2010a).

iron concentrations are smaller than 0.1 nM (Fig. 3.4). This indicates that iron limitation might be too strong there. A further reason could be the not well resolved equatorial current system (Getzlaff and Dietze, 2013). However, the overestimation of phosphate concentrations in the tropical Pacific seen in the previous version is reduced and PO_4 and NO_3 are also more in agreement with observations in the North Pacific (Fig. 3.9). In total, surface PO_4 and NO_3 RMSEs reduce by 0.02 mmol PO_4 m^{-3} and 0.28 mmol NO_3 m^{-3} with the new version.

Changes in the surface nutrient limitation and hence productivity, influence oxygen concentrations via changes in the export of sinking organic matter to the deeper ocean and the subsequent oxygen consumption during remineralization. A common mismatch between observations and simulation results in models with a coarse resolution is that high nutrient concentrations are simulated in the eastern tropical Pacific and subsequently cause large oxygen minimum zones (OMZs), i.e. volumes of low oxygen waters (< 5 mmol m^{-3}), to be formed at intermediate depths as a result of processes that have been termed "nutrient trapping"' (Najjar et al., 1992; Dietze and Loeptien, 2013; Getzlaff and Dietze, 2013). With the new model the area of the OMZ in the eastern tropical Pacific at 450 m depth is reduced while low oxygen concentrations reach further into the western Pacific (Fig. 3.10). This is more in agreement with observations of low oxygen concentrations. The relatively low oxygen concentrations of around 190 mmol m^{-3} in some places of the Southern Ocean and the OMZ in the Indian Ocean can still not be represented by the model. The OMZ is located in the Bay of Bengal instead of the Arabian Sea in both model versions. This is a common model error (Moore and Doney, 2007) and a possible reason is the coarse

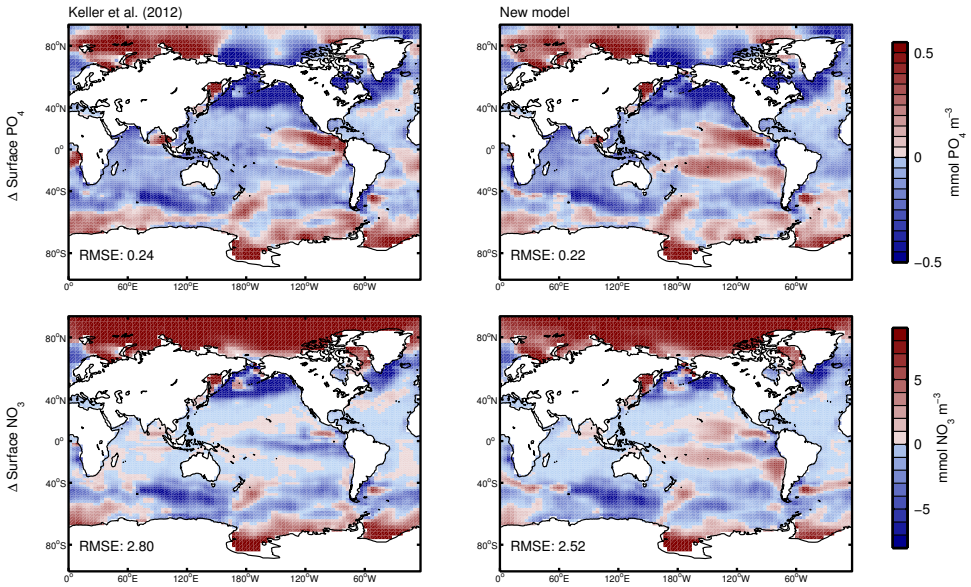

Figure 3.9: Difference between the annual mean surface WOA09 phosphate (first row) and nitrate observations (second row) and the values simulated with the model by Keller et al. (2012) and the new model.

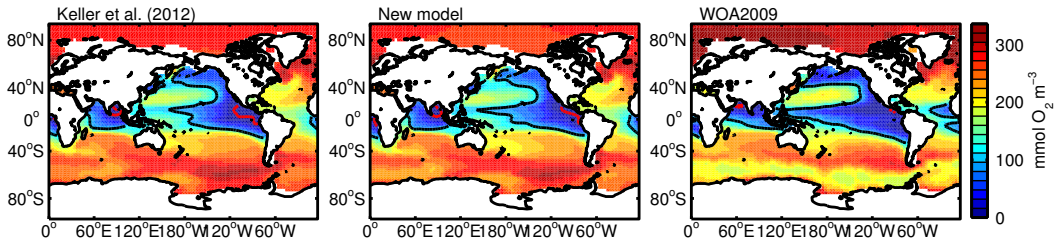

Figure 3.10: Annual mean oxygen concentrations at 450 m depth for the model by Keller et al. (2012) and the new model in comparison to observations from the World Ocean Atlas 2009 (WOA, 2009) (Garcia et al., 2010b). The black contour line is located at concentrations of 100 mmol O_2 m^{-3}, the red contour line is located at concentrations of 5 mmol O_2 m^{-3}.

resolution of these models which might not be able to realistically simulate Indian ocean currents and the transport of nutrients and oxygen. However, in total, also the global oxygen concentrations have a slightly smaller error than in the previous model (Fig. 5.2).

The global net primary production (NPP) in the ocean is calculated to be 55 Pg C yr^{-1} in the new model while it was 52 Pg C yr^{-1} in the old model. A recent estimate using both, observations and models, is in the same range, stating that 56 Pg C yr^{-1} is the most probable value for global NPP (Buitenhuis et al., 2013). Spatially, the net primary production in the new model deviates from the net primary production in the previous model mostly in that the production is more centered on the equator in the Pacific Ocean and less production occurs in the eastern tropical Pacific (Fig. 3.11). The new model also shows

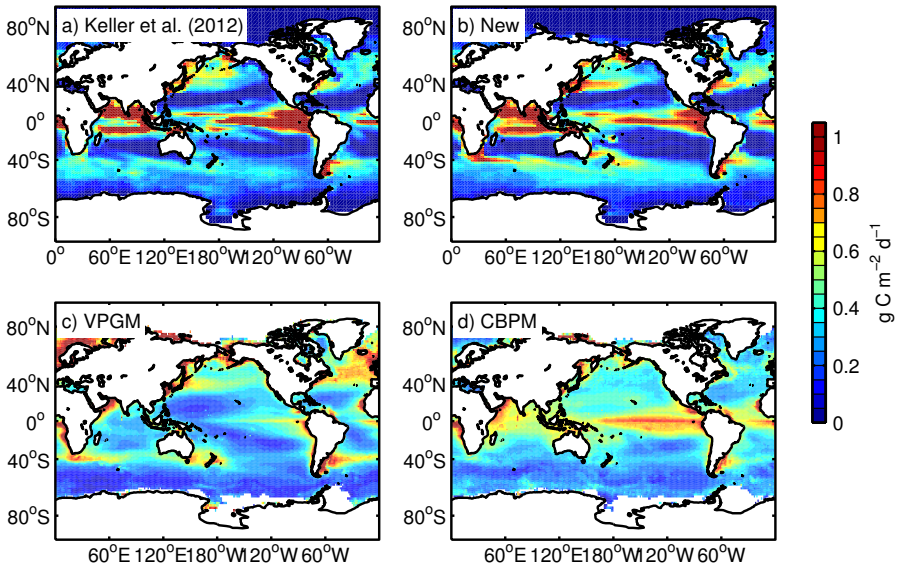

Figure 3.11: Marine vertically integrated annual mean net primary production for **(a)** the model by Keller et al. (2012) **(b)** the new model with the dynamic iron cycle, **(c)** the vertically generalized production model (VPGM) by Behrenfeld and Falkowski (1997) and **(d)** the carbon-based productivity model (CBPM) by Westberry et al. (2008).

higher production downstream of the southern tips of the continents in the Southern Ocean, such as South America, Africa and Australia. Although generally in comparison to the satellite based observational estimates coastal production seems still to be underestimated and open ocean production overestimated (Keller et al., 2012), the production in the equatorial Pacific and eastern tropical Pacific are now more similar to the observations.

These changes in productivity, relative to the old model, affect the simulated biological pump. Lower net primary production in the equatorial and eastern tropical Pacific is mirrored in the export of organic and inorganic matter (POC and PIC fluxes) at 2 km , in contrast to the higher export with the old model (Fig. 3.12a). Export in the North Pacific also decreases, although it is slightly higher off the coast of Japan. In contrast, export in the Southern Ocean is higher. The change of the flux of particulate inorganic carbon (PIC flux) from the old to the new model is similar to that of the POC flux with decreases in the equatorial and eastern tropical Pacific, North Pacific and increases in the Southern Ocean (Fig. 3.12b). Accordingly the rain ratio does not change substantially except for the arctic sea but POC and PIC fluxes are very low there so that the ratio is very sensitive to small changes and thus unimportant in a global context (Fig. 3.12c).

The higher export in the Southern Ocean with respect to the old version also increases deep phosphate concentrations in the Southern Ocean (Fig. 3.13). Apart from this Southern Ocean increase, zonally averaged phosphate concentrations are very similar to the old

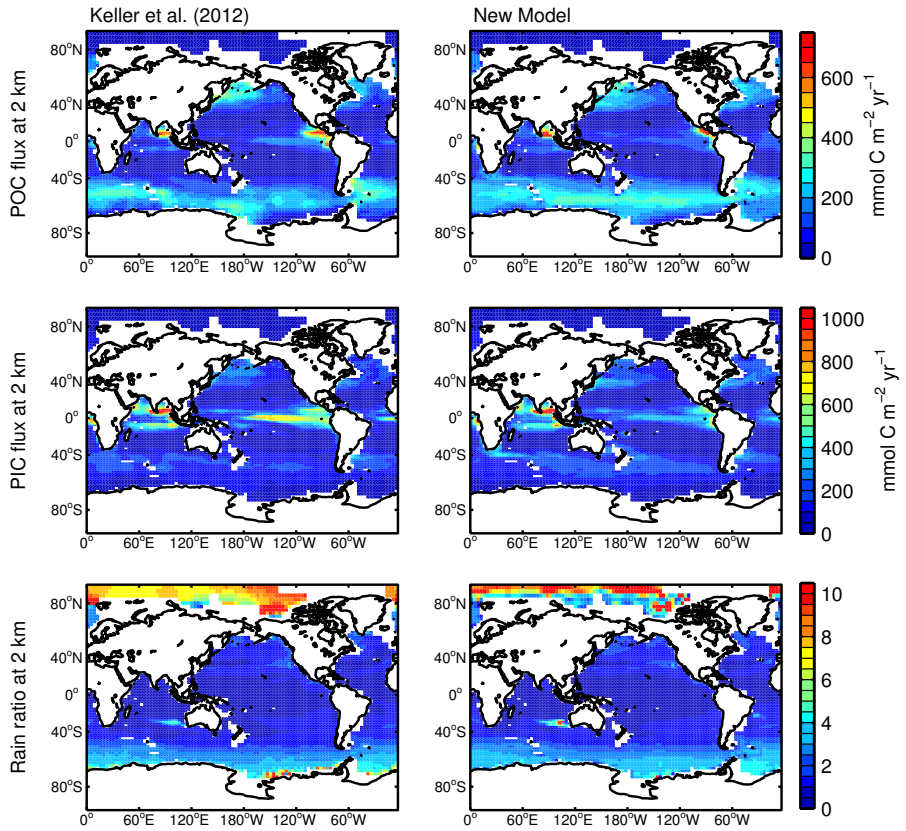

Figure 3.12: Annual mean fluxes of POC and PIC at 2 km and the rain ratio as simulated with the model by Keller et al. (2012) (left column) and with the new model (right column).

model. The global difference of NO_3 to the old version is similar to that of PO_4 because the same mechanisms apply except for N fixation and denitrification which are discussed later.

The increased export production in the Southern Ocean with the new model leads to more remineralization at the subsurface ocean and thus reduces oxygen concentrations (Fig. 3.14). This is more in line with observations. However, the observed two oxygen minima in the Atlantic Ocean directly south and north of the equator cannot be represented by the old nor the new model, presumably because of physical limitations of the model. A better representation can be achieved by adjusting the isopycnal diffusivity as in Getzlaff and Dietze (2013) and will be implemented in a future version. Globally, the RMSE of the oxygen concentrations is reduced from 26.64 mmol O_2 m^{-3} with the old model to 24.77 mmol O_2 m^{-3} with the new model. The improvement also stems from the oxygen concentrations at depths of 2000 to 3000 m in the subtropical Atlantic that are lower in comparison to the old model and thus, again closer to observed values.

The changes in zonal mean alkalinity are also closely linked to changes in export pro-

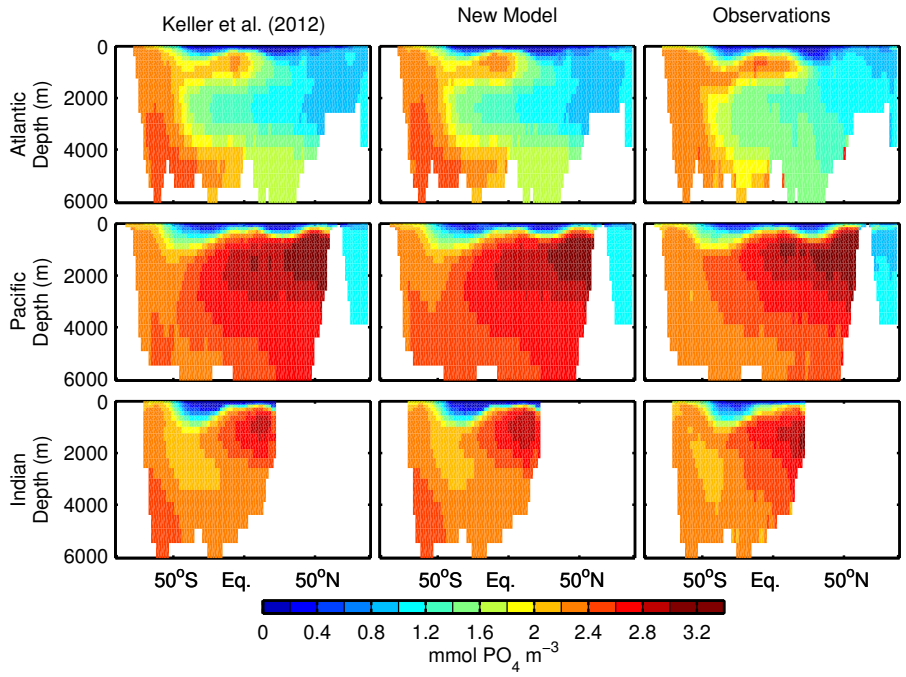

Figure 3.13: Zonal annual mean phosphate concentrations as simulated with the model by Keller et al. (2012) (left column) and the new model (middle column) in comparison to observations from the World Ocean Atlas 2009 (WOA, 2009) (Garcia et al., 2010a) (right column) for the different ocean basins.

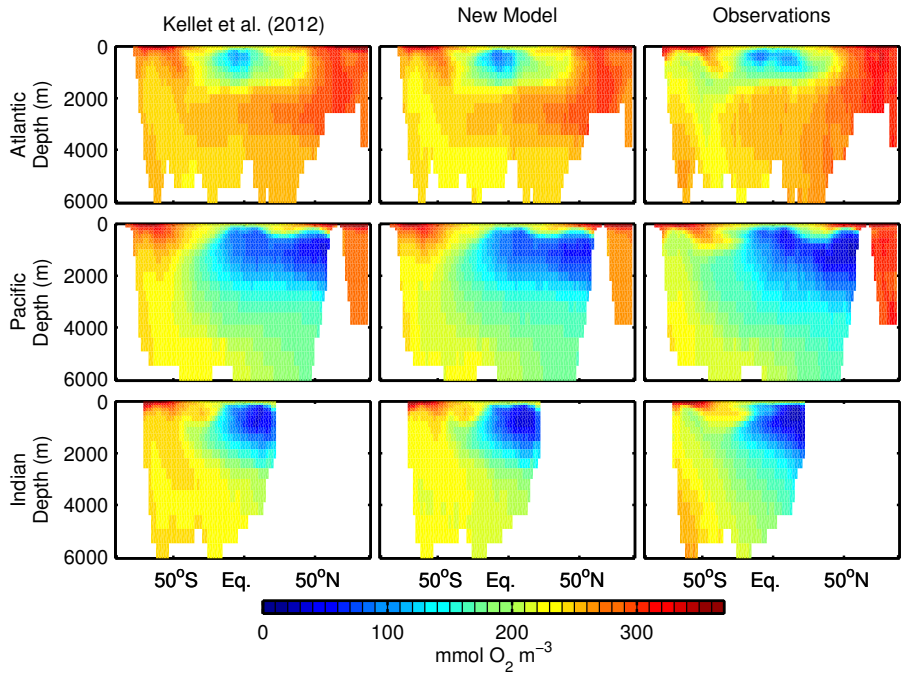

Figure 3.14: Zonal annual mean oxygen concentrations as simulated with the model by Keller et al. (2012) (left column) and the new model (middle column) in comparison to observations from the World Ocean Atlas 2009 (WOA, 2009) (Garcia et al., 2010b) (right column) for the different ocean basins.

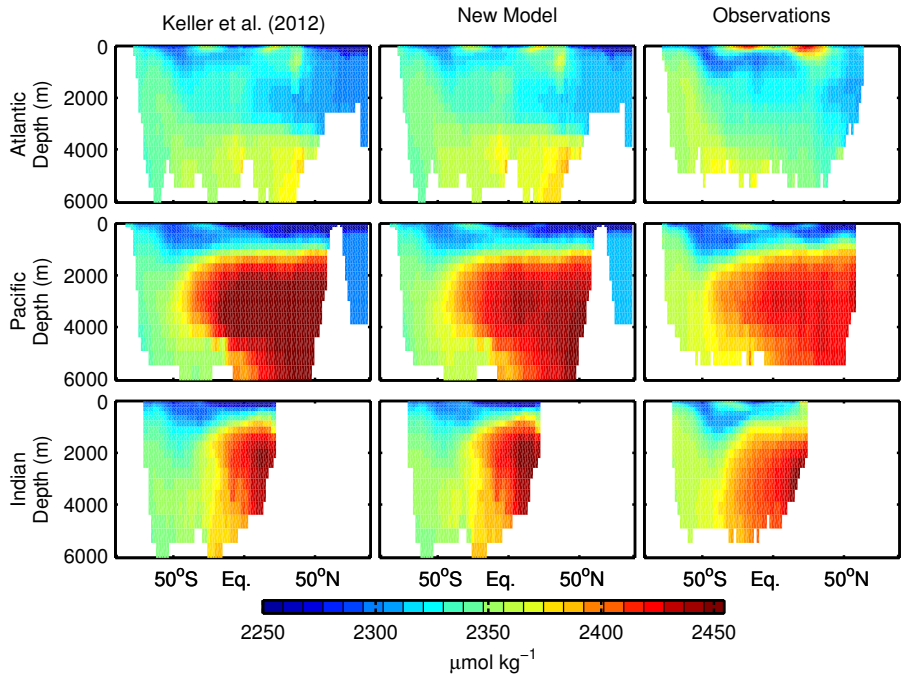

Figure 3.15: Zonal annual mean alkalinity as simulated with the model by Keller et al. (2012) (left column) and the new model (middle column) in comparison to observations from GLODAP (right column) for the different ocean basins.

duction, but the improvements in alkalinity, in comparison to the observations, take place in different regions than for oxygen (Fig. 3.15). The lower export production in the equatorial and North Pacific lowers alkalinity at intermediate depths, which thereby increases the agreement between the simulation results and the observations substantially. The improvements in alkalinity and oxygen are also visible in the globally averaged depth profiles of the model tracers in Fig. 5.2. Except for alkalinity and oxygen, the old and the new model look very similar. Differences between the simulation results and the observations however tend to be smaller with the new model (Fig. 5.2b).

The iron limitation of diazotrophs is suggested to be a major control of nitrogen fixation and thus on an important source of new oceanic nitrogen (Mills et al., 2004). With the new dynamic iron cycle simulated nitrogen fixation shifts more to the western tropical Pacific, but does also increase near the coast of the eastern tropical Pacific where deeper in the water column denitrification is taking place (Fig. 3.16). The vicious cycle hypothesis by Landolfi et al. (2013) states that spatially coupled nitrogen fixation and denitrification can lead to substantial loss of nitrogen when enhanced export production by the fixed nitrogen triggers oxygen consumption in deeper waters and thus increases denitrification which in turn increases nitrogen deficiency in upwelling water to the surface creating a niche for diazotrophs. Iron limitation at the surface was discussed as a mecha-

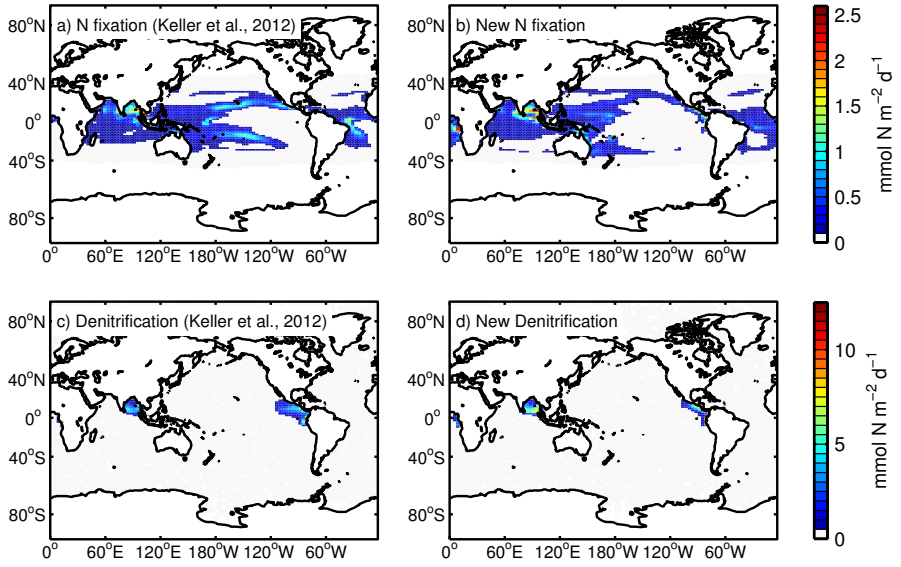

Figure 3.16: Annual mean nitrogen fixation with the model by Keller et al. (2012) **(a)** and the new model **(b)** and denitrification with the model by Keller et al. (2012) **(c)** and the new model **(d)**. Values below 0.1 mmol N m^{-2} d^{-1} are not shown for **(a)** and **(b)** while values below 0.5 mmol N m^{-2} d^{-1} are not shown for **(c)** and **(d)**.

nism that interrupts this feedback by shifting the nitrogen fixation to regions of sufficient iron concentrations away from the region of low oxygen concentrations and denitrification. However, the new model shows that near the coast, the spatial coupling of nitrogen fixation and denitrification can take place when the shallow sediments are a strong source of iron sufficient to sustain nitrogen fixation (cf. Fig. 3.2b). Elevated coastal iron concentrations may thus allow the feedback between nitrogen fixation and denitrification to exist. Indeed, Fernandez et al. (2011) observe N fixation in the eastern tropical Pacific in the area of the OMZ but more observations are needed to decide whether this feedback occurs as indicated by our model.

3.4 Model experiments

Critical assumptions in modeling the iron cycle are associated with the external sources of iron to the water column, atmospheric iron deposition and sediment release and ligand concentrations (Tagliabue et al., 2014a). Here we show the results of sensitivity tests of the globally constant ligand concentration, which is used to parameterize ligand-iron interactions, and evaluate the importance of assuming the spatially variable solubility of iron in dust and the water column depth of sedimentary iron release. The importance of assuming the spatially variable solubility of iron in dust and the water column depth of sedimentary iron release are tested for various globally fixed ligand concentrations. We also test the influence of a temperature dependence of sedimentary iron release and perform a climate warming simulation. All experiments are listed in Table 5.1. All ex-

Table 3.2: Summary of the model experiments conducted with short name, description and the parameter value of the globally constant ligand concentration.

Experiment name	Description	Ligand concentration
CTL	Control simulation configured as described in section 2	1 nM
LIG06	The globally fixed ligand concentration parameter (L_T) is varied	0.6 nM
LIG08	The globally fixed ligand concentration parameter (L_T) is varied	0.8 nM
LIG12	The globally fixed ligand concentration parameter (L_T) is varied	1.2 nM
SOL08	The solubility of iron in dust is set to a constant value of 1%	0.8 nM
SOL10	The solubility of iron in dust is set to a constant value of 1%	1 nM
SOL12	The solubility of iron in dust is set to a constant value of 1%	1.2 nM
BAT08	The subgridscale bathymetry is shut off	0.8 nM
BAT10	The subgridscale bathymetry is shut off	1 nM
BAT12	The subgridscale bathymetry is shut off	1.2 nM
TDEP	The temperature dependence of the sedimentary iron release is shut off	1 nM
CO_2EMI	Climate warming scenario with CO_2 emissions following a RCP 8.5 scenario	1 nM

periments except the climate warming simulation are run for 1000 years and the drift in average surface PO_4 during the last 100 years is less than $1.2\,\mu\text{mol}\,PO_4\,m^{-3}$

Ligand concentrations strongly control bioavailable iron concentrations (Gledhill and Buck, 2012). We thus examined the influence of varying the globally constant ligand concentrations between values of 0.6 nM and 1.2 nM on dissolved iron concentrations (Fig. 3.17). The globally averaged vertical profile of dissolved iron is strongly influenced by this variation at all depths and basically shifted to lower values for low ligand concentrations and higher values for high ligand concentrations while the shape of the curve is hardly affected. The vertical profiles of the absolute mean deviation of simulated to observed dissolved iron concentrations reveal that the chosen concentration of 1 nM is a compromise between good representation at the surface and in deeper waters. Also the global RMSE of simulated iron concentrations with a value of 0.6 nM is lowest for a ligand concentration of 1 nM. Ligand concentrations of 0.6, 0.8 and 1.2 nM lead to RMSE values of 0.69, 0.64 and 0.6 nM, respectively. While ligand concentrations of 0.6 or 0.8 nM decrease the difference to the observations from the surface to around 600 to 800 m, the deviation is increased below. On the other hand, if ligand concentrations equal 1.2 nM everywhere, the deviation from observed iron concentrations is increased from the surface down to 1500 m and is decreased or similar to the control simulation with a 1 nM ligand concentration below. For an improved agreement to the iron observations, lower ligand concentrations in the upper 1000 m would be required than below that depth, although one has to note that the low data coverage of the iron observations makes it difficult to draw robust conclusions. Völker and Tagliabue (2014) developed a model for the description of the global distribution of ligands in which they also have to assume strong ligand loss processes at the surface in order to achieve a good representation of the ligand and iron concentrations. Spatially, varying the ligand concentrations in our model leads to the strongest differences in dissolved iron concentrations in the Indian Ocean, the

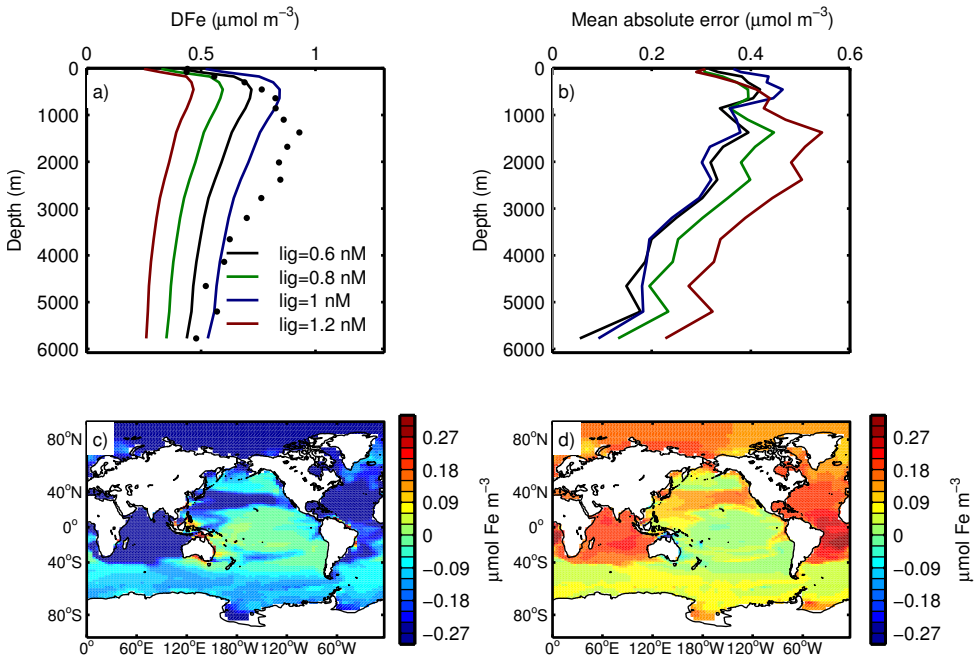

Figure 3.17: Impact of varying the globally constant ligand concentration on the globally averaged vertical profiles of dissolved iron **(a)**, vertical profiles of the horizontally averaged absolute differences between model and the observations **(b)**, difference between annual mean surface dissolved iron concentrations when ligands are set at constant values of lig=0.6 nM and lig=1.0 nM **(c)**, difference between annual mean surface dissolved iron concentrations when ligands are set at constant values of lig=1.2 nM and lig=1.0 nM **(d)**.

tropical and subtropical Atlantic and the subtropical north Pacific. In the other regions iron limitation prevails, iron concentrations are already small and do not decrease much further with lower ligand concentrations. If ligand concentrations are increased in these iron limited regions, the additional bioavailable iron that is produced is readily taken up by phytoplankton so that the difference is small as well. Overall, the sensitivity of dissolved iron concentrations is very high (on average ±0.27 nM at the surface). Because of this strong sensitivity, better constraints on the source and sink processes of ligands are needed to create a comprehensive and computationally efficient representation of variable ligand concentrations in global ocean models.

Most previous modeling studies have assumed a constant solubility of iron in dust (Moore and Braucher, 2008; Tagliabue et al., 2014a; Nickelsen and Oschlies, 2015). However, observations show that the solubility of iron in dust can vary significantly and is generally lower in areas of high dust deposition and higher when dust deposition is low (Baker and Croot, 2010). Luo et al. (2008) tested several assumptions on how iron solubility could change during transport in the atmosphere and compared their simulated atmospheric iron deposition to observations of iron deposition. They found that assuming all iron that

comes in contact with clouds is slowly converted to soluble iron and that particularly hematite is a source of soluble iron under acidic conditions results in the best agreement to observations. Their simulated iron deposition also reflects the observed trend of increased solubility at sites of low deposition. To test the importance of having variable solubility we performed a simulation in which iron solubility was set to a constant value of 1 % (this is equal to the global average solubility of the standard model run which has variable solubility) and ran the experiment for 1000 years We repeated this experiment with different globally constant ligand concentrations of 0.8 nM (experiment SOL08) and 1.2 nM (experiment SOL12) (cf. Table 5.1). The results are compared here to the results of the standard model simulation with variable solubility (CTL) and the runs from the ligand concentrations sensitivity experiments LIG08 and LIG12. Although the integrated total iron deposition increases from 2.1 in CTL to 17.8 Gmol Fe m^{-2} yr^{-1} in SOL01, the changes in surface iron concentrations are small (Figs. 3.18 and 3.4). As expected iron concentrations are higher at sites of high dust deposition (+2 nM Fe in the tropical Atlantic and +1 nM Fe in the Arabian Sea) and lower at low dust deposition (−0.1 nM Fe in the tropical Pacific). In the SOL08 experiment with constant solubility and a ligand concentration of 0.8 nM, a part of the increase in surface iron concentration in the high dust deposition areas is compensated by the lower ligand concentrations. In contrast, with a ligand concentration of 1.2 nM the constant solubility leads to strong overestimation of surface iron concentrations.

Surface phosphate concentrations are essentially unaffected because the iron limited areas are still iron limited and regions in which iron deposition is high are not iron limited in both cases. The only exceptions are based on a slight increase of iron concentrations at the southern tips of Australia (+0.3 nM) and South America (up to +0.2 nM). These are the areas where surface phosphate concentrations decrease. The strongest effect of the consideration of the variable solubility can be seen in the RMSE of simulated surface iron concentrations. The RMSE increases from 0.68 nM with variable solubility to 0.91 nM with constant solubility. This result supports the observation of variable solubility of iron in dust and the approach of Luo et al. (2008) but a higher spatial coverage of iron observations is needed to verify this result.

To investigate how ligand concentrations influence the response to the change in the solubility of iron in dust we compare the surface phosphate concentrations of the experiments SOL08 and SOL12 to the surface phosphate concentrations of the experiments LIG08 and LIG12 (Fig. 3.18d-f). For the higher ligand concentrations the difference in surface phosphate concentrations is even smaller than for the lower ligand concentrations. Higher

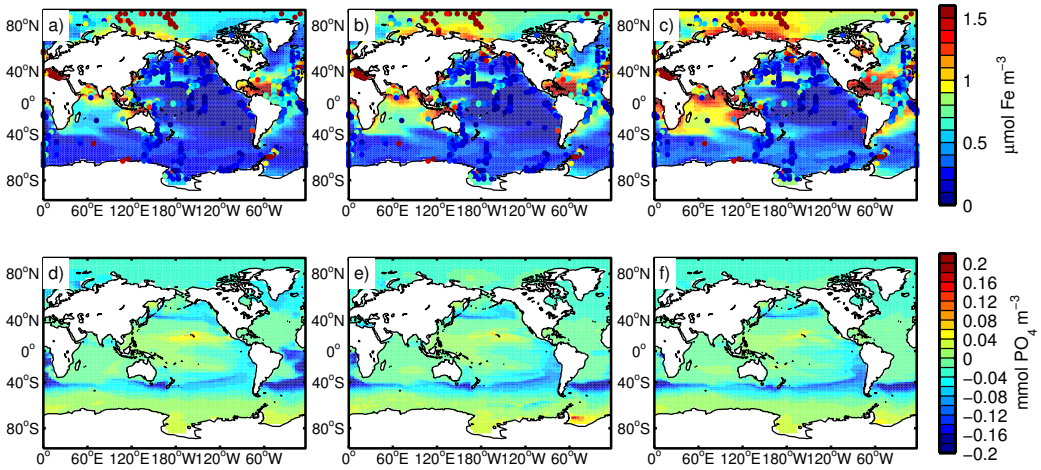

Figure 3.18: Impact of setting the iron solubility in dust to a constant value of 1 % Annual mean simulated surface iron concentrations with observations compiled by Tagliabue et al. (2012) averaged over the first 50 m plotted as colored circles on top for experiment SOL08 are shown in **(a)**, for SOL10 in **(b)** and for SOL12 in **(c)**. The difference between the annual mean surface phosphate concentrations after 1000 years of experiment SOL08 and LIG08 are shown in **(d)**, between SOL10 and LIG10 in **(e)** and between SOL12 and LIG12 in **(f)**. The experiments are listed in Table 5.1.

iron concentrations in the control run buffer changes in the external supply since iron concentrations are generally higher and the change of iron concentrations relative to their background concentration is smaller. As suggested also by Tagliabue et al. (2014a) ligand concentrations can have a strong control on sensitivities to changes in dust deposition.

The sediment release of iron is a much larger source of iron to the ocean than dust deposition (Tagliabue et al., 2014a), but it is not clear how much iron released from the sediment reaches the surface ocean. One factor determining whether iron from the sediments reaches the surface ocean in coarse resolution global ocean models is that the simulated bathymetry that can deviate quiet strongly from the actual bathymetry. As in other models (Moore and Braucher, 2008; Tagliabue et al., 2014a), we use a subgridscale bathymetry to correct the depth of the sedimentary iron release to that of a high resolution dataset of ocean depth. To test the importance of this depth correction, we turned the correction off in our second experiment and ran the model for 1000 years This leads to much lower surface iron concentrations, more phytoplankton iron limitation (NPP decreases from 55 to 39 Pg C yr^{-1}) and an accumulation of macronutrients at the ocean surface (Fig. 3.19). Although the globally integrated release of iron from the sediment increases from 18.8 Gmol Fe yr^{-1} in the control run to 35.5 Gmol Fe yr^{-1} in the experiment due to local feedbacks in the western Gulf of Mexico and north of Indonesia (Fig. 3.19a), iron in the experiment is released deeper and in regions that are not iron limited. This shows that iron released from the sediment is crucial for sustaining iron concentrations

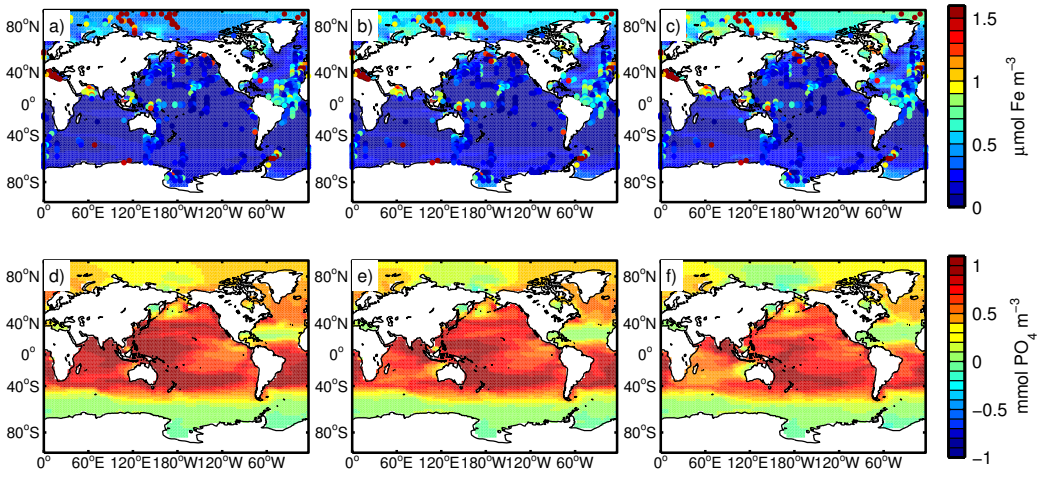

Figure 3.19: Impact of shutting of the subgridscale bathymetry after a 1000 year simulation. Annual mean simulated surface iron concentrations with observations compiled by Tagliabue et al. (2012) averaged over the first 50 m plotted as colored circles on top for experiment BAT08 are shown in **(a)**, for BAT10 in **(b)** and for BAT12 in **(c)** (cf. 5.1). The difference between the annual mean surface phosphate concentrations after 1000 years of experiment BAT08 and LIG08 are shown in **(d)**, between BAT10 and LIG10 in **(e)** and between BAT12 and LIG12 in **(f)**. The experiments are listed in Table 5.1.

at the surface in iron limited regions and that the depth of iron release is an important factor to consider in coarse resolution models. However, these results depend on the assumptions made for iron release from the sediment. The question whether sedimentary released iron reaches the surface is critical and observations show high uncertainties. At the study site of Elrod et al. (2004) with measurement depths ranging from 95 to 3710 m off of the California coast the amount of sedimentary released iron reaching the surface varies by 2.5 to 30 %. In a modelling study the efficiency of iron delivery from sediments to surface ocean waters can vary by 10-50 % (Siedlecki et al., 2012) depending on frequent wind changes. Therefore, more research is needed on the fate of sediment-derived iron.

To test the influence of the globally constant ligand concentration parameter on the effect of shutting off the subgridscale bathymetry we repeated the expreiment with different globally constant ligand concentrations of 0.8 nM (experiment BAT08) and 1.2 nM (experiment BAT12) (cf. Table 5.1). While iron concentrations are slightly higher with higher ligand concentrations (e.g. in the tropical Atlantic), the effect of shutting off the subgridscale bathymetry dominates over the change in ligand concentrations (Fig. 3.19). The difference in surface phosphate concentration between experiments BAT08 and LIG08 are similar to the differences with the higher ligand concentrations. Also with regard to the phosphate concentrations, the effect of shutting off the subgridscale bathmetry thus prevails over the effect of varying the ligand concentrations. Tagliabue et al. (2014a) even

shut off the complete sediment source of iron and at the same time double and halve the ligand concentrations. Their results similarly show that on top of the changes in atmospheric CO_2 concentration due to shutting off the sediment source of iron, ligand variations introduce additional changes of 10-25%. Thus, the effect of shutting off the sediment release is also larger than the variation of the ligand concentrations in their results.

We scaled the sedimentary iron release with bottom water temperature to introduce temperature dependent remineralization in sediments as it was already applied to remineralization in the water column in the previous model versions. Enzymatic reactions are directly temperature dependent (Arndt et al., 2013) so dissimilatory iron reduction in sediments should be temperature dependent as well. Although physiological adaptation of the benthic microbial community to low temperatures may compensate for some of the positive effect of temperature on remineralization rates (Arndt et al., 2013), lab experiments show that remineralization rates increase up to sevenfold when sediment is incubated at a temperature gradient (Arnosti et al., 1998; Sanz-Lázaro et al., 2011). The exact influence of temperature on remineralization in sediments is thus still unclear (Arndt et al., 2013). Our choice to include the temperature dependence on the sedimentary iron release is mainly motivated by too high simulated iron concentrations in the Southern Ocean without the temperature dependence. For comparison we optimized the ratio of iron released from the sediment and phosphorus in particulate matter that sinks into the sediment ($Fe : P_{\mathrm{sed}} = 0.015\,\mathrm{mol\,Fe\,(mol\,P)^{-1}}$) in a simulation without the temperature dependence of the sedimentary iron release to give the best possible agreement to observations and conducted a 1000 year test simulation. While the average observed iron concentrations south of 40° S are 0.52 nM, simulated concentrations are 0.67 nM without and 0.53 nM with the temperature dependence. Both simulations show a reasonable globally averaged vertical profile of dissolved iron while without the temperature dependence the profile appears to be closer to the observations because of generally higher concentrations (Fig. 3.20a). However, the difference between simulated and observed iron concentrations is smaller in the simulation with temperature dependence, particular in the deep ocean below 3500 m but also from the surface down to 1500 m (Fig. 3.20b). Generally, the simulation without temperature dependence leads to lower iron concentrations in the tropical ocean, particular in the Indian Ocean and the western Pacific because of shallow water depths, and higher iron concentrations in the higher latitudes compared to the simulation without the temperature dependence. Thus, more phosphate is taken up in the higher latitudes and phosphate concentrations increase in the tropical regions and east of Australia due to increased iron limitation near Australia and in the tropical Pacific. The model

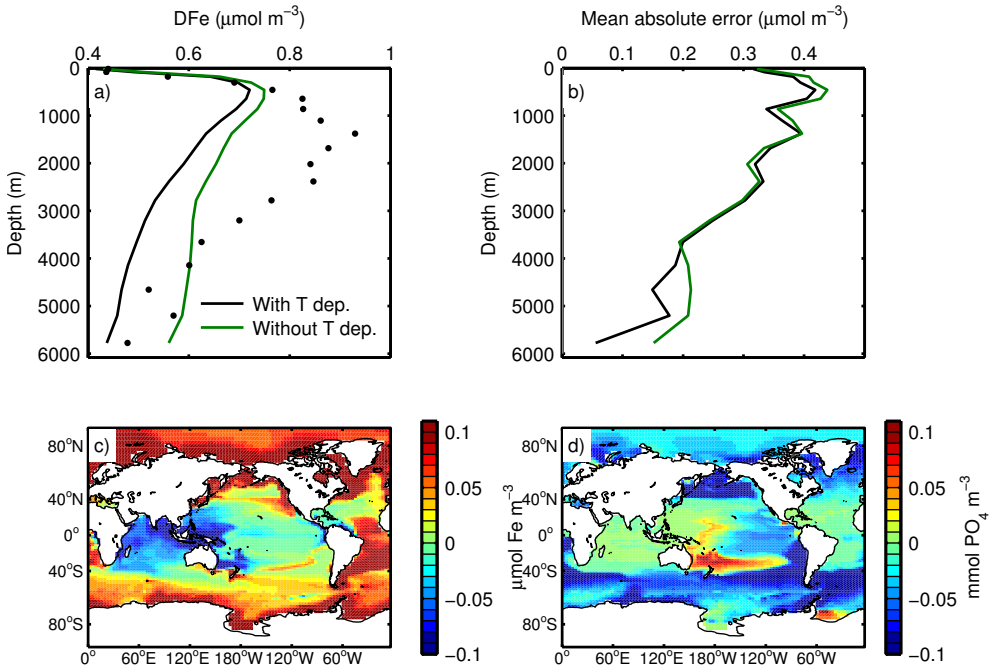

Figure 3.20: Influence of the temperature dependence (T dep.) of the benthic iron release. **(a)** Vertical profiles of globally averaged dissolved iron concentrations (dFe) with (black) and without (green) the temperature dependence. **(b)** Vertical profile of the averaged absolute deviation between simulated and observed dFe with (black) and without (green) the temperature dependence. **(c)** Difference in surface dissolved iron concentrations and **(d)** difference in surface phosphate concentrations between the simulations without and with the temperature dependence.

without the temperature dependence and $Fe : P_{\text{sed}} = 0.015\,\text{mol Fe}\,(\text{mol P})^{-1}$ can be seen as an alternative configuration. Although iron observations are still scarse and associated with uncertainty as discussed before, because there is a better agreement with the observations with the temperature dependent sedimentary iron release parameterization we made this formulation the standard one. However, more observations and experiments of the temperature dependence of benthic remineralization are needed to verify our assumption. Finally, we performed global warming scenario simulations with the old and the new model and analyzed the response of the ocean. The other components of the Earth system appear to be nearly not influenced by the inclusion of the dynamic iron cycle and the general response of the model to climate warming has already been analyzed in Eby et al. (2013), Zickfeld et al. (2013), and Keller et al. (2014). We ran both models from the 10 000 year long spinups for an additional 200 years during which the atmospheric CO_2 concentration was allowed to change. Then, we started the emissions driven climate change scenario in the year 1765 and ran the model to year 2100. The CO_2 emissions follow historical observations to the year 2000 and then a high-CO_2 emissions representative concentration pathway (RCP 8.5) scenario (Meinshausen et al., 2011). Changes in land use, volcanic and solar forcing, aerosols and other greeenhouse

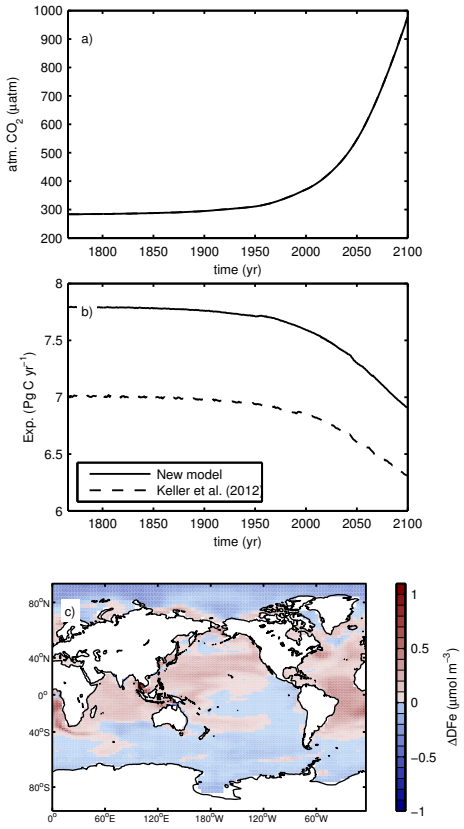

Figure 3.21: Results of the global warming scenario run following the high CO_2 emissions representative concentration pathway (RCP 8.5) scenario: **(a)** Annual average CO_2 concentrations with the new model and with the model by Keller et al. (2012) (not distinguishable), **(b)** globally integrated export production at 80 m with the new model and with the model by Keller et al. (2012), **(c)** the difference in surface dissolved iron concentrations between the year 2100 and year 1765.

gases are held constant in our simulations. The global warming scenario simulations with the old and new models do not differ much in terms of atmospheric CO_2 concentrations (Fig. 3.21) as it is only 1.2 μatm lower in the year 2100 with the new model than with the old one. The inclusion of a dynamic iron cycle does thus not alter the oceanic CO_2 exchange in our model during a climate change simulation on this time scale. However, export production is decreasing faster with the new model during the time from 1765 to 2100. At the same time NPP decreased from 54.82 to 50.98 Pg C yr^{-1} with the new model and only from 53.70 to 51.90 Pg C yr^{-1} with the old model. This stronger decrease is due to the increasing iron limitation in the iron limited regions such as the Southern Ocean, equatorial Pacific and North Pacific. The changes in iron limitation are caused by stronger stratification which increases iron concentrations at regions of high dust deposition but decreases iron in regions where supply from the deep ocean is dominant (Fig. 3.21c).

During the climate warming simulation we keep the atmospheric iron deposition con-

Table 3.3: Simulated fluxes in the iron cycle expressed in Gmol Fe yr^{-1} for the preindustrial model state at year 1765 and a future state at year 2100. The difference of the fluxes is denoted by ΔFlux.

Flux name	1765	2100	ΔFlux
Sediment release	18.8	17.8	−1
Svavenging	67.8	75.2	+7.4
Remineralization	64.2	65.2	+1
Recycling	28.6	26.7	−1.9
Uptake	45.2	42.2	−3
Grazing/Lysis	16.7	15.6	−1.1

stant but the sediment release of iron decreases from 18.8 to 17.8 Gmol Fe yr^{-1} (Table 3.3) due to the lower amount of organic matter reaching the sediment. In our model, the role of O_2 on the sediment release of iron is restricted to areas of $O_2 < 5\,mmol\,m^{-3}$ which, in our simulation, show a global decrease over the 21st century under global warming as in Duteil and Oschlies (2011). While scavenging and remineralization increase by 7.4 and 1.0 Gmol Fe yr^{-1} , iron recycling, uptake and grazing/lysis decrease during the simulations from 1765 to 2100. This is caused by the higher stratification, leading to lower iron concentrations in the euphotic zone and higher concentrations below. Together this shows that the response of the dynamic iron cycle to the CO_2 emission scenario has a limited impact on the atmospheric CO_2 concentration on centennial time scales, but that the changes of iron concentration can be strong and possibly lead to changes in ocean biogeochemistry on longer time scales.

3.5 Conclusions

Including a dynamic iron cycle leads to a better agreement between observed and simulated iron and, to a minor extent, macronutrient concentrations than with the iron concentration mask used in the previous model (Keller et al., 2012). The iron cycle now also responds dynamically and interactively with the ocean biogeochemistry to possible perturbations. The improvement of the iron cycling model, when compared to other models such as the one by Misumi et al. (2013), is in part due to better constrained parameters, for example by Gledhill and Buck (2012). Since many fluxes and parameters of the iron cycle are still unconstrained and we find a strong sensitivity of the simulated iron concentrations to ligand concentrations, more observations are necessary, particular ones associated with scavenging since it is the largest flux in the iron cycle.

Many studies have focused on dust deposition as the dominant source of iron to the ocean (Parekh et al., 2008; Tagliabue et al., 2008; Oka et al., 2011; Nickelsen and Os-

chlies, 2015), while recently sediment release of iron has been suggested to also be highly important (Moore and Braucher, 2008; Tagliabue et al., 2009a, 2014a). We add to these results with our experiments regarding the variable solubility of iron in dust, the temperature dependence of sedimentary iron release and the depth correction of iron release from the sediment. Although variable solubility of iron has a strong impact on the iron concentrations simulated by our model, its effect on macronutrient concentrations is small because it primarily alters iron concentrations in regions that are not iron limited. On the other hand, the subgridscale bathymetry for sedimentary iron release has a very strong impact on both iron concentrations and macronutrients because sediment release is the dominant source of iron in iron limited regions such as the Southern Ocean and eastern tropical Pacific in our model. The temperature dependence of the sedimentary iron release primarily leads to a better agreement between simulated and observed dissolved iron concentrations in the Southern Ocean. Changes in the sediment source can thus potentially drive strong changes in iron limitation at the surface and more observations on what controls sedimentary iron release are crucial.

The dynamic response of the iron cycle also allows us to investigate its response to climate change. A previous study found that physical changes in ocean circulation could influence iron supply in iron limited regions (Misumi et al., 2014). However, the largest external source of iron, the release of iron from the sediments, is constant in their model. Due to the strong control of iron released from the sediments on surface iron limitation shown earlier, the response of the sedimentary iron release to climate change could contribute largely to changes of iron concentration and primary production. Sediment release of iron depends on organic matter reaching the sediment, temperature and bottom water oxygen concentrations in our model, all of which change during climate change. Particularly changes in oxygen concentrations could influence iron release from the sediment and could, in turn, also be influenced by iron limitation at the ocean surface. Lower iron limitation could lead to higher export of organic matter and oxygen consumption during respiration. The possible interaction between oxygen and iron concentrations and parameterizations of iron release from the sediment are thus worth to be investigated further.

Model code availability

The University of Victoria Earth System Climate Model version 2.9 (2009) together with a readme file is available at `http://www.climate.uvic.ca/model/`. The complete files of the model code of the model version used in this paper that are different to files at `http://www.climate.uvic.ca/model/` are available in the Supplement together with additional forcing files. Please see the readme file in the supplement for further instructions on

how to use the code. In addition, the model output of the last 1000 years which is used to create the plots and restart files after 9000 and 10 000 years of the 10 000 year spinup are provided at `https://thredds.geomar.de/thredds/fileServer/peerReviewData/nickelsen-et-al_gmd_2014/Nickelsen-et-al_GMD_2014_submitted.zip`.

Acknowledgements We acknowledge financial support from the Deutsche Forschungsgemeinschaft (SFB 754). We thank Michael Eby (University of Victoria, Victoria, Canada) for maintaining the code of the UVic model, Natalie Mahowald (Cornell University, Ithaca, USA) for sharing the dust deposition estimates and Heiner Dietze (GEOMAR, Kiel, Germany) for helpful discussions, advice and technical support.

4 A revised global estimate of dissolved iron fluxes from marine sediments

This chapter is based on the paper "A revised global estimate of dissolved iron fluxes from marine sediments" accepted for publication in the journal Global Biogeochemical Cycles. Citation: Dale, A. W., Nickelsen, L., Scholz, F., Hensen, C., Oschlies, A., and Wallmann, K. (2015). A revised global estimate of dissolved iron fluxes from marine sediments. Global Biogeochemical Cycles, accepted, doi:10.1002/2014GB005017.

Abstract Literature data on benthic dissolved iron (DFe) fluxes (µmol m^{-2} d^{-1}), bottom water oxygen concentrations (O_{2BW}, µM) and sedimentary carbon oxidation rates (C_{OX}, mmol m^{-2} d^{-1}) from water depths ranging from 80 to 3700 m were assembled. The data were analyzed with a diagenetic iron model to derive an empirical function for predicting benthic DFe fluxes:

$$\text{DFe flux} \quad = \quad \gamma \tanh(\frac{C_{ox}}{O_{2BW}})$$

where γ (=170 µmol m^{-2} d^{-1}) is the maximum flux for sediments at steady state located away from river mouths. This simple function unifies previous observations that C_{OX} and O_{2BW} are important controls on DFe fluxes. Upscaling predicts a global DFe flux from continental margin sediments of 109 ± 55 Gmol yr^{-1}, of which 72 Gmol yr^{-1} is contributed by the shelf (<200 m) and 37 Gmol yr^{-1} by slope sediments (200 - 2000 m). The predicted deep-sea flux (>2000 m) of 41 ± 21 Gmol yr^{-1} is unsupported by empirical data. Previous estimates of benthic DFe fluxes derived using global iron models are far lower (ca. 20-30 Gmol yr^{-1}). This can be attributed to (i) inadequate treatment of the role of oxygen on benthic DFe fluxes, and (ii) improper consideration of continental shelf processes due to coarse spatial resolution. Globally-averaged DFe concentrations in surface waters simulated with an intermediate-complexity Earth system climate model (UVic ESCM) were a factor of two higher with the new function. We conclude that (i) the DFe flux from marginal sediments has been underestimated in the marine iron cycle, and (ii) iron scavenging in the water column is more intense than currently presumed.

4.1 Introduction

Iron (Fe) is a regulating micronutrient for phytoplankton productivity and the efficiency of the biological pump over large areas of the ocean (Martin and Fitzwater, 1988; Martin and Gordon, 1990; Moore and Doney, 2007; Boyd and Ellwood, 2010). Indeed, natural

iron fertilization of the ocean by enhanced dust inputs is believed to have contributed to lower CO_2 levels during the Last Glacial Maximum (Martin and Gordon, 1990; Sigman and Boyle, 2000). Understandably, therefore, global circulation models with a focus on Fe have often considered dissolution from dust to be the major external source of dissolved iron to the surface ocean (Archer and Johnson, 2000; Aumont, 2003; Parekh et al., 2004). The atmospheric, dissolvable iron input is around 10 Gmol yr^{-1} or less, yet is highly uncertain due to the poorly-constrained solubility of particulate iron (Jickells et al., 2005; Luo et al., 2008; Mahowald et al., 2005; Galbraith et al., 2010; Misumi et al., 2014; Nickelsen et al., 2014).

More recently, continental margin sediments have been shown to be important sources of dissolved iron (DFe) to the coastal ocean and beyond (Elrod et al., 2004; Lohan and Bruland, 2008; Cullen et al., 2009; Severmann et al., 2010; Jeandel et al., 2011; John et al., 2012; Conway and John, 2014). Most global iron models now include an explicit sediment source of DFe, albeit with very different parameterizations. For instance, benthic DFe fluxes have been described using a fixed or maximum flux at the seafloor (Moore et al., 2004; Aumont and Bopp, 2006; Misumi et al., 2014). Others used the empirical relationship between DFe flux and benthic carbon oxidation rates (C_{OX}) proposed by Elrod et al. (2004) (Moore and Braucher, 2008; Palastanga et al., 2013). In recognition that DFe fluxes from marine sediments are enhanced under oxygen-deficient bottom waters (McManus et al., 1997; Lohan and Bruland, 2008; Severmann et al., 2010), some workers opted for an oxygen 'switch' (Galbraith et al., 2010; Nickelsen et al., 2014). Here, all particulate iron that falls to the seafloor is returned to the water column as DFe if bottom water oxygen concentration (O_{2BW}) falls below a pre-defined threshold. Given the lack of consensus of how benthic iron should be described in models, the magnitude of this source is only vaguely constrained at 8 – 32 Gmol yr^{-1} (Jickells et al., 2005; Galbraith et al., 2010; Misumi et al., 2014; Nickelsen et al., 2014; Tagliabue et al., 2014a). This uncertainty is very likely propagated to the parameterization of the DFe source/sink terms in the water column, which themselves are very poorly understood (Nickelsen et al., 2014). Thus, there is a real need to better constrain DFe sources and sinks in the ocean.

Whilst there is little disagreement that both O_{2BW} and C_{OX} are important factors for predicting DFe fluxes, a unifying paradigm has so far not been proposed in a quantitative and empirical fashion. The oxygen threshold used by Galbraith et al. (2010) and Nickelsen et al. (2014) is an advance in the right direction, but the threshold concentration is somewhat arbitrary and not well justified empirically. In this study, we re-analyze the available literature data at sites where benthic DFe fluxes, O_{2BW} and C_{OX} have been

reported. Our prime objective is to derive a simple algorithm to predict DFe fluxes from marine sediments at the global scale based on O_{2BW} and C_{OX} as the two key controlling variables. We then analyze the impact of this source on DFe distributions in ocean surface waters by coupling the algorithm to an intermediate-complexity Earth system climate model (UVic ESCM). We find that the sedimentary DFe source may be several times higher than current estimates suggest, implying that scavenging in the water column is currently too weak in global iron models and that the residence time of iron in the ocean is shorter than assumed previously.

4.2 Data acquisition and evaluation

Benthic iron fluxes were compiled from the literature along with reported O_{2BW} and C_{OX} (Table 4.1). In these studies, the water samples for iron analysis were filtered (0.45 µm), acidified and analyzed for the total dissolved fraction using various analytical methodologies (see Table 4.1). Only fluxes measured using non-invasive benthic chambers were considered. DFe fluxes derived from pore water gradients often do not correlate with in situ fluxes due to processes at the sediment water interface operating over spatial scales smaller than the typical cm-scale sampling resolution Homoky et al. (2012). Furthermore, enhanced DFe flux to the bottom water by flushing of animal burrows (bioirrigation) is also not captured by pore water gradients. We note, however, that benthic DFe fluxes determined using chambers may also suffer from artifacts due to oxidative losses and scavenging onto particles (e.g. Severmann et al. (2010)). In this study, we make no attempt to re-evaluate the published data with regards to these aspects and the reported benthic DFe fluxes are used.

Almost all data where DFe fluxes, O_{2BW} and C_{OX} have been measured simultaneously originate from the Californian shelf and slope (McManus et al., 1997; Berelson et al., 2003; Severmann et al., 2010). These data cover a wide range of C_{OX} and O_{2BW} from severely hypoxic ($\sim$ 3 µM) to normal oxic ($>$ 63 µM) conditions. DFe fluxes range from $<$0.1 µmol m^{-2} d^{-1} on the slope to 568 µmol m^{-2} d^{-1} in the San Pedro Basin. High fluxes of 332 µmol m^{-2} d^{-1} were also measured on the Oregon margin close to river mouths (Severmann et al., 2010). Absent from the Californian data are DFe fluxes under anoxic conditions. In situ fluxes are available for anoxic areas of the Baltic and Black Seas (Friedrich et al., 2002; Pakhomova et al., 2007). Yet, these are not included in our database because supporting C_{OX} data are unfortunately lacking. We therefore supplemented the database with fluxes from the Peruvian OMZ where bottom waters on the shelf and upper slope are predominantly anoxic (Noffke et al., 2012). The highest DFe flux in our database was measured here (888 µmol m^{-2} d^{-1}). In this study, we define anoxia as O_2 concentrations

Table 4.1: Literature data on benthic DFe fluxes

Region	Water depth [a] (m)	O_2 (µM)	C_{OX} (mmol m^{-2} d^{-1})	DFe flux (µmol m^{-2} d^{-1})	Remarks
Californian margin and Borderland Basins [b]	100 – 3700	8 – 138	0.3 – 7.3	0.02 – 48	Highest fluxes with shallow oxygen penetration depths
Monterey Bay (California) [c]	100	101 – 185	6.9 – 14.7	1.3 – 10.8	Inter- and intra-annual variability at a single station
Oregon-California shelf and Californian Borderland Basins [d]	90 – 900	3 – 153	2 – 23	12 – 568	High fluxes for Eel River mouth and San Pedro and Santa Monica Basins. Temporal variability.
Peruvian margin [e]	95 – 400	< d.l	2.4 – 7.7	11 – 888	Highest flux measured for an open margin setting

[a] Depth range where the data were collected.
[b] McManus et al. (1997): Total dissolved iron determined by chemiluminescence. Positive fluxes only (= out of sediment). Negative fluxes are <0.5 µmol m^{-2} d^{-1} and ignored in this study. C_{OX} was determined from $\sum CO_2$ fluxes corrected for carbonate dissolution.
[c] Berelson et al. (2003): Total dissolved iron determined by flow-injection analysis with chemiluminescence detection. C_{OX} was determined from $\sum CO_2$ fluxes corrected for carbonate dissolution.
[d] Severmann et al. (2010): Total dissolved iron determined by inductively coupled plasma mass spectrometry. DFe fluxes of 421 to 568 µmol m^{-2} d^{-1} were reported for the San Pedro and Santa Monica basins compared to only 13 – 18 µmol m^{-2} d^{-1} measured previously at the same sites (reported by Elrod et al. (2004)). C_{OX} was determined from $\sum CO_2$ fluxes without correction for carbonate dissolution.
[e] Noffke et al. (2012): Total dissolved iron determined by inductively coupled plasma mass spectrometry. C_{OX} was determined as the HCO_3^- flux from pore water TA gradients and showed very good agreement with numerical modeling results (Bohlen et al., 2011).

below the detection limit of the Winkler titration, ca. 3 µM.

The final database includes 82 data points where DFe flux, O_{2BW} and C_{OX} data have been reported for the same site. DFe fluxes and C_{OX} were taken as the reported mean values plus error (where given) determined from multiple chambers during the same deployment. Hence, the actual number of individual DFe fluxes is much greater than 81. In total, 25 fluxes are from shelf settings (≤200 m), 40 are from the slope (>200 – 2000 m), and 16 are from deeper waters down to 3700 m. The deep sea is thus under-represented in the database compared to the continental margin.

At first glance, defining any relationship between DFe flux, O_{2BW} and C_{OX} seems like an impossible task (Fig. 4.1). DFe fluxes scatter over many orders of magnitude for any given O_{2BW} or C_{OX}. The apparent dependence of DFe flux on O_{2BW}, as observed in the data set of (Severmann et al., 2010), is much more tenuous when data from all studies are considered collectively. The linear relationship between DFe flux (in µmol m^{-2} d^{-1}) and C_{OX} (in mmol m- 2 d^{-1}) proposed by Elrod et al. (2004) does seem to broadly apply (DFe = 0.68 × C_{OX} – 0.5), although DFe fluxes > 10 µmol m^{-2} d^{-1} for low C_{OX} are not well represented by that model (Fig. 4.1b).

In order to understand the scatter in these plots, we first organized the individual fluxes into two groups depending on whether the C_{OX} was above or below 4 mmol C m^{-2} d^{-1}. This definition is not arbitrary; it represents the C_{OX} at the shelf break (ca. 200 m) where a sharp gradient change in total benthic O_2 uptake occurs (Andersson, 2004). Above this depth (i.e. on the shelf), C_{OX} increases to > 20 mmol m^{-2} d^{-1} whereas on the slope it declines much more gradually to ca. 1 mmol m^{-2} d^{-1} or less at 3000 m (Burdige, 2007). Although we recognize that C_{OX} does not strictly correlate with water depth, the overall relationship is clear enough (see Burdige (2007) that we can collectively term the sites above and below the C_{OX} threshold as shelf and slope, respectively.

In a second step, the DFe fluxes were binned into discrete O_{2BW} intervals: anoxic (O_{2BW} $\leq$ 3 µM), severely hypoxic (> 3 µM < O_{2BW} $\leq$ 20 µM), weakly hypoxic (> 20 µM < O_{2BW} $\leq$ 63 µM) and normal oxic (O_{2BW} > 63 µM). Two of these boundaries were chosen based on strict (i.e. anoxia, that is, below detection limit) or more consensual definitions (i.e. hypoxia = O_2 < 63 µM). The 20 µM boundary is somewhat subjective. We chose this value because Elrod et al. (2004) noted that their DFe-C_{OX} correlation did not capture iron fluxes at sites with O_{2BW} concentrations below this value. It may well be that this concentration represents a tipping point beyond which large changes in DFe flux occur due to alterations in respiration pathways and/or faunal regime shifts (Levin and Gage, 1998). We will revisit this idea later.

Following these criteria, the data broadly show that DFe flux correlates inversely with increasing O_{2BW} and decreasing C_{OX}. High DFe fluxes on the shelf (circles in Fig. 4.1a) are clearly distinguishable from the much lower fluxes on the slope (triangles). For the slope setting, low DFe fluxes of 1.3 and 0.4 µmol m^{-2} d^{-1} are found for the weakly hypoxic and oxic intervals, respectively, whereas a pronounced increase to 36 and 188 µmol m^{-2} d^{-1} is associated with the severely hypoxic and anoxic intervals (respectively). A very similar trend emerges for the shelf with a high end flux of 465 µmol m^{-2} d^{-1} in anoxic shelf settings. However, there is a large uncertainty associated with these numbers due to (i) few data available for anoxic and hypoxic sites on the shelf and (ii) bias towards the high fluxes measured in the San Pedro and Santa Monica Basins and on the Peru and Eel River shelves. Excluding these four points with DFe fluxes > 300 µmol m^{-2} d^{-1} considerably reduces the binned values for anoxic and severely hypoxic waters (open symbols in Fig. 4.1a). Furthermore, it is also not clear if the high fluxes on the shelf truly reflect higher C_{OX}, or whether this simply reflects the fact that most organic matter is deposited on the shelf along with iron-rich terrestrial material. Consequently, in the following section we use a diagenetic model to identify the factors regulating benthic iron

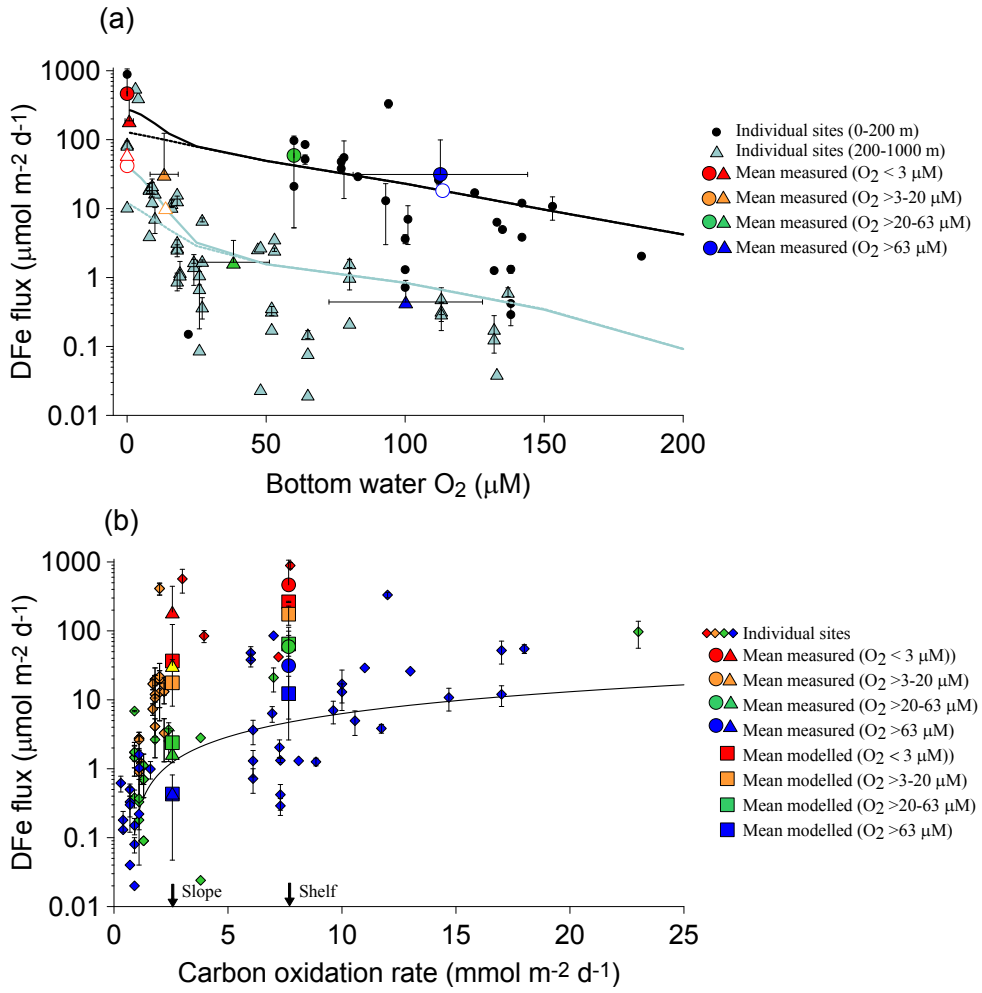

Figure 4.1: Measured DFe fluxes versus bottom water O_2. Black circles and light blue triangles correspond to individual sites with $C_{OX} > 4$ ($\approx$ shelf) and <4 mmol m^{-2} d^{-1} ($\approx$ slope), respectively. The larger colored symbols are the mean DFe fluxes and O_2 concentrations within each binned range of O_2 (error bars are standard deviations), where circles and triangles denote shelf and slope, respectively. The large white symbols with colored outlines show the binned data without the four fluxes > 300 µmol m^{-2} d^{-1} (San Pedro Basin, Santa Monica Basin, Eel River shelf and Peruvian shelf). The black and blue curves are modeled fluxes for the shelf and slope, respectively; solid curves = standard model, dashed curves = standard model with no decrease in faunal activity at low O_{2BW}. (b) Measured DFe fluxes versus C_{OX} color-coded according to O_{2BW} (diamonds). The large circles (shelf) and triangles (slope) are the measured binned data from (a) plotted for the shelf and slope values of C_{OX} (indicated on x-axis). The mean modeled fluxes for each O_{2BW} interval are the corresponding colored squares. The curve is the regression of Elrod et al. (2004): DFe = 0.68 × C_{OX} – 0.5, based on data published by McManus et al. (1997) and Berelson et al. (2003). Error bars for the individual sites in (a) and (b) are taken from the literature where reported (Table 4.1). Error bars on C_{OX} are not shown for clarity.

fluxes and provide a mechanistic understanding of the emerging trends in Fig. 4.1.

4.3 Benthic iron model

A vertically-resolved 1-D reaction-transport model was used to simulate the coupled C, N, Fe, Mn and S cycles in the upper 30 cm of sediments. Our aim is to calculate benthic DFe fluxes in representative shelf (0-200 m) and upper slope (200-1000 m) environments for the observed range of O_{2BW} (1-200 µM) and compare these to the measured data in Fig. 4.1. Water depths of 100 m and 600 m (respectively) were chosen based on conventional hypsometric intervals (Menard and Smith, 1966). In the model, solids are transported dynamically by sediment accumulation and by bioturbation in the upper mixed surface layer where metazoans mainly reside. Solutes are also affected by molecular diffusion and bioirrigation; the latter describing the non-local exchange of seawater with pore water by burrowing fauna. The model is described fully in the Supplement of Dale et al. (2015). It is based on previous empirical diagenetic models and for greater transparency we have formulated the biogeochemical reactions and parameters in line with these studies (e.g. VanCappellen and Wang (1996); Wang and Van Cappellen (1996); Berg (2003); Dale et al. (2009, 2013)).

The parameterization of key transport processes, boundary conditions and kinetic parameters was achieved using global empirical relationships where possible (Table 4.2). The sedimentation rate and surface bioturbation coefficient were calculated on the basis of water depth (Burwicz et al., 2011; Middelburg et al., 1997). Similarly, Burdige (2007) compiled a database of sediment C_{OX} for the same water depth intervals as used here. As a first approximation, this was assumed to be equal to the total rain rate of particulate organic carbon (POC) to the seafloor since less than 10% of organic matter reaching the ocean floor is ultimately preserved in marine sediments (Hedges and Keil, 1995). Bioirrigation coefficients were calculated following the procedure of Meile and Van Cappellen (2003). In line with other models, irrigation of Fe^{2+} was lowered relative to other solutes due to its high affinity to oxidation on burrow walls (Berg, 2003; Dale et al., 2013). Fluxes of total iron oxides were defined according to the bulk sedimentation rate (Table 4.2).

Due to the general scarcity of data from sediments underlying oxygen deficient waters, these global relationships apply to normal oxic conditions. Yet, the bioirrigation and bioturbation coefficients cannot be treated as constant parameters in the simulations due to the dependency of metazoans on oxygen. Faunal activity levels under low O_2 are not well documented, but the rate and intensity of bioturbation and irrigation are probably lower (Diaz and Rosenberg, 1995; Middelburg and Levin, 2009). The bioirrigation and

Table 4.2: Key model parameters used in the simulation of the shelf and slope sediments [a]

	Shelf	Slope	Source
Representative water depth (m) [b]	100	600	*Menard and Smith* [1966]
Temperature of the bottom water (°C)	10	8	*Thullner et al.* [2009]
Sediment accumulation rate, ω_{acc} (cm kyr^{-1})	100	16	*Burwicz et al.* [2011]
POC rain rate, F_{POC} (mmol m^{-2} d^{-1}) [c]	9.4	3	*Burdige* [2007]
Total iron oxide (Fe_T) rain rate, F_{FeT} (µmol m^{-2} d^{-1}) [d]	1840	290	This study
Dissolved oxygen concentration in seawater, O_{2BW} (µM) [e]	variable	variable	This study
Dissolved ferrous iron concentration in seawater	0	0	This study
Rate constant for aerobic Fe^{2+} oxidation, k_{l3} (M^{-1} yr) [f]	5×10^{-8}	5×10^{-8}	Various
Bioturbation coefficient at surface, $D_b(0)$ (cm^2 yr^{-1}) [g]	$28{\cdot}f$	$18{\cdot}f$	*Middelburg et al.* [1997]
Bioturbation halving-depth, z_{bt} (cm^2 yr^{-1})	3	3	*Teal et al.* [2008]
Bioirrigation coefficient at surface, $\alpha(0)$ (yr^{-1}) [g,h]	$465{\cdot}f$	$114{\cdot}f$	*Meile and Van Cappellen* [2003]
Bioirrigation attenuation coefficient, z_{bio} (cm) [i]	2	0.75	This study
Average lifetime of the reactive POC components, a (yr) [j]	3×10^{-4}	3×10^{-4}	*Boudreau et al.* [2008]
Shape of gamma distribution for POC mineralization, υ (-) [j]	0.125	0.125	*Boudreau et al.* [2008]

[a] The complete model is described in the Supplement of Dale et al. (2015).

[b] The mid-depth of the shelf (0-200 m) and upper slope (200-1000 m) according to Menard and Smith (1966).

[c] Table 4 in Burdige (2007), based on his compilation of benthic carbon oxidation rates.

[d] Fluxes of total particulate iron oxide (Fe_T) to the sediment were based on the Fe content in average sedimentary rock (∼5%, (Garrels and Mackenzie, 1971) which is similar to Fe content in red clays (Glasby, 2006). The total Fe flux was calculated using the equation $0.05\omega_{acc}(1-\phi(L))\rho_s/A_W$ where $\phi(L)$ is the porosity of compacted sediment (0.7), ρ_s is the dry sediment density (2.5 g cm–3) and A_W is the standard atomic weight of iron (55.8 g mol^{-1}). 50% of this flux is unreactive (Poulton and Raiswell, 2002), and the other 50% is divided equally among F_{FeHR}, F_{FeMR} and F_{FePR} (see text).

[e] Values tested in the model are 1, 2, 5, 10, 15, 25, 50, 100 and 200 µM.

[f] VanCappellen and Wang (1996); Wang and Van Cappellen (1996); Berg (2003) and others. See Supplement of Dale et al. (2015) for reaction stoichiometry and kinetics.

[g] f is a dimensionless factor that scales the bioturbation and bioirrigation coefficients to O_{2BW} (µM). It is equal to $0.5+0.5\cdot erf((O_{2BW}-a)/b)$, where *erf* is the error function and a (20 µM) and b (12 µM) are constants that define the steepness of decline of f with decreasing O_{2BW}.

[h] Meile and Van Cappellen (2003) calculated the average bioirrigation coefficient in surface sediments ($\overline{\alpha}$, yr^{-1}) based on total sediment oxygen uptake and bottom water O_2. As a first approximation, sediment oxygen uptake was assumed to be equal to F_{POC}. $\alpha(0)$ was calculated from $\overline{\alpha}$ following Thullner et al. (2009) for a bottom water O_2 concentration of 120 µM which is representative of shelf and slope environments. Irrigation of Fe^{2+} was scaled to 20% of that for other solutes due to its high affinity for oxidation on burrow walls.

[i] The depth of the sediment affected by irrigation on the shelf was adjusted to coincide with the depth of the bioturbation zone (ca. 7 cm).

[j] A full description of POC degradation kinetics is given in the Supplement of Dale et al. (2015).

bioturbation coefficients were thus multiplied by a factor (f) that mimics the reduction in faunal activity at low O_{2BW} (Table 4.2). Specifically, the maximum bioirrigation and bioturbation rates are reduced by 50% when O_{2BW} is at the level where shifts in faunal community structure occur (ca. 20 µM, Levin and Gage (1998). Bioirrigation and bioturbation rates are depressed even further at lower O_{2BW}, in line with field observations (Dale et al., 2013). The model sensitivity to constant animal mixing rates for all O_{2BW} levels is shown below.

Continuum kinetics for describing POC degradation is a key aspect of the model (Middelburg, 1989; Boudreau and Ruddick, 1991). This approach captures the temporal evolution of organic matter reactivity, as opposed to multi-G models that pre-define a fixed first-order decay constant of one or more carbon fractions (Westrich and Berner, 1984). However, continuum models cannot be readily applied to bioturbated sediments due to random mixing of particles of different ages by animals (Boudreau and Ruddick, 1991). Thus, we developed a procedure for approximating the continuum model in bioturbated sediments by defining multiple (14) carbon pools based on the initial distribution of carbon reactivity (see Supplement of Dale et al. (2015)). This distribution is defined by two parameters; the average lifetime of the reactive components, a (yr), and the distribution of POC reactivity, ν (-) (Table 4.2). Low ν values indicate that organic matter is dominated by refractory components, whereas higher values correspond to a more even distribution of reactive types. Similarly, organic matter characterized by low a will be rapidly degraded below the sediment-water interface whereas a high a implies less reactive material that is more likely to be buried to deeper sediments. Whilst we can expect some regional differences in these parameters, we used values corresponding to fresh organic matter to shelf and slope settings (Boudreau et al., 2008). This is a reasonable, but not entirely robust, assumption given relatively rapid particulate sinking rates in the water column (Kriest and Oschlies, 2008).

A comprehensive iron cycle is included. The reactivity of particulate iron (oxyhydr)oxides (hereafter Fe oxides) was defined according to the widely-employed classification based on wet chemical extraction methods (Canfield et al., 1992; Raiswell and Canfield, 1998; Poulton et al., 2004). Reactive Fe oxides can be broadly defined as highly reactive (Fe_{HR}), moderately reactive (Fe_{MR}) or poorly reactive (Fe_{PR}). Fe_{HR} has a half-life of < 1 yr and represents iron contained within amorphous and reactive crystalline oxides (ferrihydrite, goethite, lepidocrocite and hematite), pyrite and acid volatile sulfides, plus a small fraction of iron in reactive silicates (Canfield et al., 1992; Raiswell and Canfield, 1998). Fe_{PR} has a half-life of at least 105 yr and represents iron released from a wide range of reactive

silicates and magnetite. Fe_{MR} comprises all the iron with a reactivity intermediate between Fe_{HR} and Fe_{PR} (i.e. magnetite and reactive silicates) with a half life of 102 yr. An additional terrigenous detrital iron fraction, representing Fe bound within silicate minerals (Fe_U), is essentially unreactive on early diagenetic time scales and constitutes about half of all sedimentary iron underlying oxic waters (Poulton and Raiswell, 2002). The model simulates all four of these fractions, defined chemically as $Fe(OH)_3$.

The Fe cycle involves a number of oxidation-reduction pathways (see Supplement of Dale et al. (2015)). These include authigenic precipitation of Fe_{HR} via aerobic and anaerobic oxidation of ferrous iron; processes that constitute an efficient geochemical barrier against DFe release from the sediment (McManus et al., 1997; Berg, 2003). Reactive Fe oxides can be reduced by dissolved sulfide according to the reaction kinetics proposed by (Poulton et al., 2004). Fe_{HR} is also consumed by dissimilatory iron reduction (DIR), whereas the other phases are too crystalline (unreactive) to be of benefit to iron reducing bacteria (Weber, 2006). Non-reductive dissolution of iron has also been proposed to be a dominant source of benthic iron on continental margins that display low rates of reductive Fe dissolution (Radic et al., 2011; Jeandel et al., 2011; Homoky et al., 2013; Conway and John, 2014). However, this process has not been described mechanistically and is not considered in our model at this point in time. Fe_{HR} further undergoes ageing into more crystalline Fe_{MR} (Cornell and Schwertmann, 1996). The iron module also includes iron mono-sulfide (FeS) and pyrite (FeS_2) precipitation; the latter via the H_2S pathway (Berzelius reaction) and by reaction with elemental sulfur, S^0 (Bunsen reaction) (Rickard and Luther, 2007). FeS and FeS_2 can be oxidized aerobically, whereas S^0 can disproportionate to sulfate and sulfide.

The model was coded and solved using the method of lines with MATHEMATICA 7.0 assuming a diffusive boundary layer of 0.04 cm thickness at the sediment-water interface (Boudreau, 1996). Further details on the model solution can be found in the Supplement Dale et al. (2015).

4.4 Model results

The model reproduces the trend of higher DFe fluxes with decreasing O_{2BW} (Fig. 4.1a) and increasing C_{OX} (Fig. 4.1b). The absolute magnitude of the modeled fluxes for the shelf and slope settings depends on the water depths chosen to represent these environments, meaning that the fluxes are not as rigidly defined as implied in the plots. The modeled DFe fluxes for each O_{2BW} interval in the anoxic and severely hypoxic intervals are underestimated. Yet, with the exception of the anoxic shelf, removing the four fluxes

> 300 µmol m^{-2} d^{-1} improves the agreement with the model (open symbols, Fig. 4.1a). The anoxic shelf flux is tenuous because only two data points are available here.

As O_{2BW} increases, a larger fraction of POC is respired by O_2 at the expense of other electron acceptors, principally sulfate (Fig. 4.2a). DIR accounts for less than 2% of POC respiration under all O_{2BW} conditions on the shelf, and less than 0.2% on the slope. Nonetheless, DIR constitutes the largest source of DFe for anoxic and hypoxic settings (Fig. 4.2b). At higher O_{2BW}, reduction of iron oxides by sulfide becomes more important. This finding is counter-intuitive because sulfidic reduction is expected to be less pronounced as O_{2BW} increases. It can be explained by the increase in bioturbation which mixes labile iron oxide below the surface sediment where POC mineralization rates are highest (Fig. 4.2d). This results in a less pronounced DIR peak and a greater likelihood that iron oxide is instead reduced by sulfide deeper down. In these subsurface horizons, iron undergoes repeated redox cycling (Fig. 4.2b,c) whereby DFe is oxidized to Fe(III), mainly by Mn(IV), and then regenerated when the authigenic iron oxide is again reduced by sulfide or organic matter (e.g. Wang and Van Cappellen (1996). This tends to increase the apparent total rate of iron sources (or sinks), from 595 µmol m^{-2} d^{-1} under anoxia to 757 µmol m^{-2} d^{-1} under weakly hypoxic conditions, even though the total flux of particulate iron to the sediment is the same in all cases.

Under near anoxic conditions, almost half of all DFe is lost to the water column (Fig. 4.2c). A sink-switching effect takes place with higher O_{2BW}, whereby DFe oxidation increases at the expense of benthic DFe loss, thereby leading to greater retention of DFe. DFe fluxes fall sharply when bottom waters transition from severe to weak hypoxia, which is reflected in the field observations by the increase in DFe fluxes when $O_{2BW} < 20$ µM (Fig. 4.1). This concentration may represent a tipping point, beyond which sediments become highly efficient at retaining the iron deposited on the sediment surface. In this regard, it is noteworthy that the boundary between surface sediments that are enriched and depleted in Fe in the Peruvian oxygen minimum zone is located exactly where bottom oxygen concentrations rise above 20 µM (Scholz et al., 2014a).

The impact of O_{2BW} on DFe fluxes is illustrated more graphically by the DFe pore water concentrations in Fig. 4.2d. Under very low O_{2BW}, the DFe concentration gradient at the sediment-water interface is extremely sharp, which drives a large flux across the diffusive boundary layer. In this case, O_2 barely penetrates the sediment and acts as a poor geochemical barrier to DFe flux (McManus et al., 1997). Under weakly hypoxic conditions, O_{2BW} penetrates deeper leading to a more efficient oxidative sink for DFe. The resulting

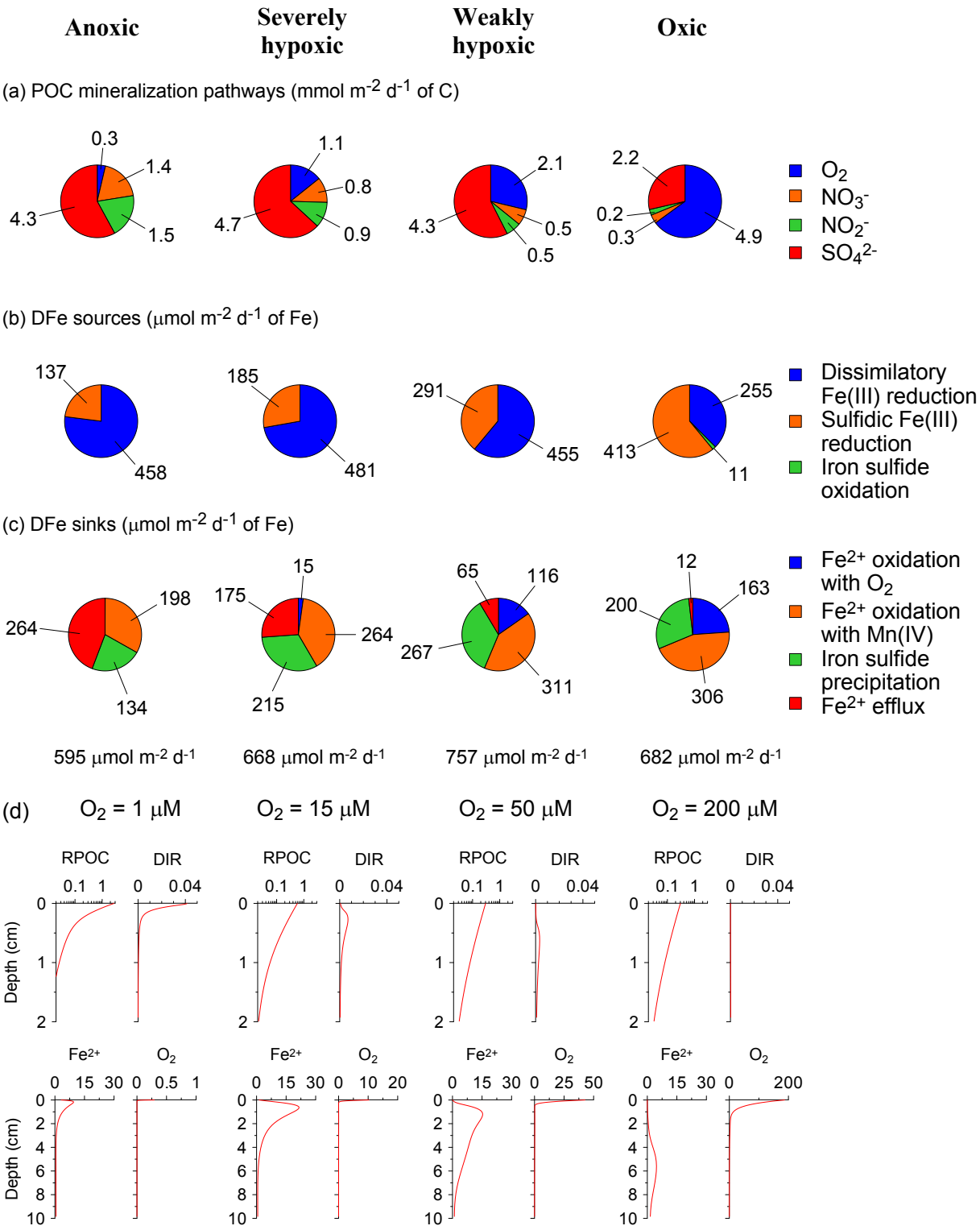

Figure 4.2: (a-c) Simulated rates for the shelf environment for each oxygen regime indicated at the top of the figure. (a) POC mineralization pathways. Fe and Mn oxide reduction rates are <0.1 mmol m^{-2} d^{-1} and not indicated. (b) DFe sources. Iron sulfide oxidation is negligible and only shown for the oxic setting. (c) DFe sinks. Oxidation by NO_3^- and irrigation are negligible and not shown. Aerobic oxidation of ferrous iron in the anoxic setting is zero and also not shown. The total sum of sinks (= sum of sources) is shown underneath the lower pie charts. (d) Sediment depth profiles of POC mineralization rate (RPOC) and dissimilatory iron reduction (DIR) in mmol cm^{-3} yr^{-1} of C, and dissolved ferrous iron and oxygen concentration in μM for representative O_{2BW} in each interval (note different depth scales). Total fluxes on the slope are lower, but the pathways are qualitatively similar.

DFe concentration gradient in the uppermost millimeters is markedly shallower, and the flux to the bottom water much smaller. Finally, under normal oxic conditions, the DFe peak is spatially separated from the surface by several centimeters and only a very weak DFe flux is predicted.

We propose that the DFe flux tipping point is related to sediment ventilation by burrowing animals. The impact of irrigation in our model is demonstrated by the dashed curves in Fig. 4.1a which show that DFe fluxes are much lower on the shelf and slope if faunal activity is unaffected by low O_{2BW}. This conflicts with (Elrod et al., 2004), who suggested that DFe fluxes were enhanced by bioirrigation in Monterey Bay sediments ($O_{2BW} > 100$ µM). Yet, the importance of bioirrigation in mitigating DFe fluxes is supported by previous observations. Firstly, mesocosm experiments showed that burrowing fauna act to increase iron retention due to rapid immobilization of DFe as particulate iron oxide phases on burrow walls (Lewandowski et al., 2007). These results have been reproduced using bioirrigation models that employ empirically-derived rate constants for aerobic DFe oxidation (Meile et al., 2005). Secondly, bottom water DFe concentrations in the later stages of sediment incubations increase quasi-exponentially concomitant with dissolved oxygen depletion (Severmann et al., 2010). This has been attributed to the loss of the surface oxidized layer on the walls of animal burrows as well as a reduced rate of DFe oxidation in oxygen-depleted chamber waters. More generally, DFe fluxes are low in sediments bearing a surface oxidized layer (McManus et al., 1997). Clearly, then, in addition to C_{OX}, DFe fluxes show a strong dependence on O_{2BW}, especially for concentrations below 20 µM. In the following section, we derive a function based on both these variables to predict DFe fluxes from sediments.

4.5 Derivation of a predictive function for benthic iron fluxes

An empirical function for predicting benthic DFe fluxes from C_{OX} and O_{2BW} was derived using a more detailed sensitivity analysis. This was based on a standardized model defined by the average parameter values of the shelf and slope settings (Table 4.3). A series of model runs was executed where organic matter rain rate and O_{2BW} were varied between 0.5-16 mmol m^{-2} d^{-1} and 1-200 µM, respectively. The corresponding C_{OX} for these rain rates is 0.4-13.2 mmol m^{-2} d^{-1}. These ranges are characteristic of the sites in Table 4.1 and much of the seafloor in general. Although rain rate and O_{2BW} were the only two model aspects to be varied directly, the bioturbation and bioirrigation coefficients were dependent on O_{2BW}, as previously. This avoids anomalous scenarios, such as high bioirrigation at sites with low benthic respiration (e.g. pelagic settings).

Table 4.3: Input parameters and boundary conditions used in the standard model and for the sensitivity analysis [a]

	Standard model	Sensitivity analysis
Representative water depth (m)	350	350
Sediment accumulation rate, ω_{acc} (cm kyr^{-1})	60	60
POC rain rate, F_{POC} (mmol m^{-2} d^{-1})	6.2	0.5-15 [b]
Total iron oxide (Fe_T) rain rate, F_{FeT} (µmol m^{-2} d^{-1})	1110	1110
Dissolved oxygen concentration in seawater, O_{2BW} (µM)	120	1-200 [c]
Bioturbation coefficient at surface, $D_b(0)$ (cm^2 yr^{-1})	$23 \cdot f$	$23 \cdot f$
Bioirrigation coefficient at surface, $\alpha(0)$ (yr^{-1})	$290 \cdot f$	$290 \cdot f$
Bioirrigation attenuation coefficient, z_{bio} (cm)	1.4	1.4

[a] Model parameters that are unchanged from Table 4.2 are not listed.
[b] Values tested (in mmol m^{-2} d^{-1}) are: 0.5, 1, 2, 4, 6, 8, 10, 12, 14, 16, which are equivalent to C_{OX} of 0.4, 0.8, 1.7, 3.3, 5.0, 6.6, 8.3, 9.9, 11.6 and 13.2.
[c] Values tested are 1, 2, 5, 10, 15, 25, 50, 100 and 200 µM.

The dependence of DFe flux on O_{2BW} for constant values of C_{OX} is shown in Fig. 4.3a. DFe flux increases with decreasing O_{2BW} for all C_{OX}, with a tipping point centered at around 20 µM, as observed previously. Furthermore, sediments release more iron as C_{OX} increases due to higher rates of aerobic carbon respiration at the expense of DFe oxidation. Benthic DFe flux also responds strongly to small increases in C_{OX} when O_{2BW} is below ca. 10 µM (Fig. 4.3b). The pronounced peak in DFe centered at $C_{OX} = 2$ mmol m^{-2} d^{-1} originates from high DIR rates close to the sediment surface (c.f. Fig. 4.2d). The subsequent dip in DFe flux when C_{OX} 4 mmol m^{-2} d^{-1} signifies sequestration of iron into sulfide minerals as sulfate reduction rates increase. DFe fluxes then gradually increase again with higher C_{OX} as in Fig. 4.3a. These results demonstrate that C_{OX} is itself an important factor to consider for predicting DFe fluxes, in addition to the total flux of labile particulate iron (see below).

The sensitivity analysis supports observations that C_{OX} acts on DFe flux in an opposite way to O_{2BW} (Elrod et al., 2004; Severmann et al., 2010). Hence, we derived a predictive function for DFe fluxes (in µmol m^{-2} d^{-1}) to reflect this behavior:

$$\text{DFe flux} = \gamma \tanh\left(\frac{C_{ox}}{O_{2BW}}\right) \quad (4.1)$$

where C_{OX} is in mmol m^{-2} d^{-1} and O_{2BW} is in µM. γ is the maximum flux that can escape the sediment for a given Fe content and reactivity. In our simulations, this is predicted to be 170 µmol m^{-2} d^{-1}.

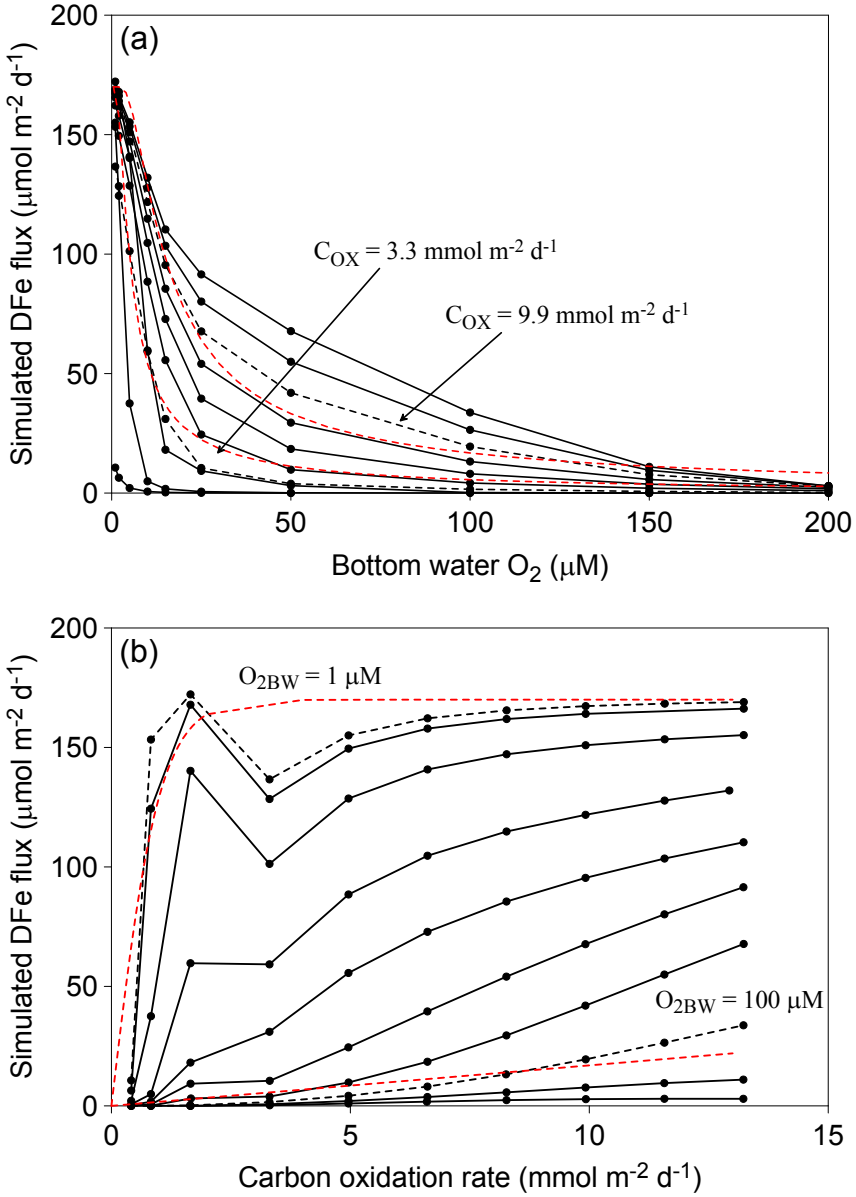

Figure 4.3: Simulated DFe fluxes from the standardized numerical model versus (a) bottom water oxygen concentration and (b) carbon oxidation rate. In (a), the results for a C_{OX} of 9.9 and 3.3 mmol m^{-2} d^{-1} are shown as dashed curves and compared to the predicted fluxes from the new function (Eq. 4.1) in adjacent red dashed curves. In (b), the results for O_{2BW} of 1 and 100 µM are compared to the new function. All other black curves correspond to the O_{2BW} and C_{OX} intervals listed in Table 4.3.

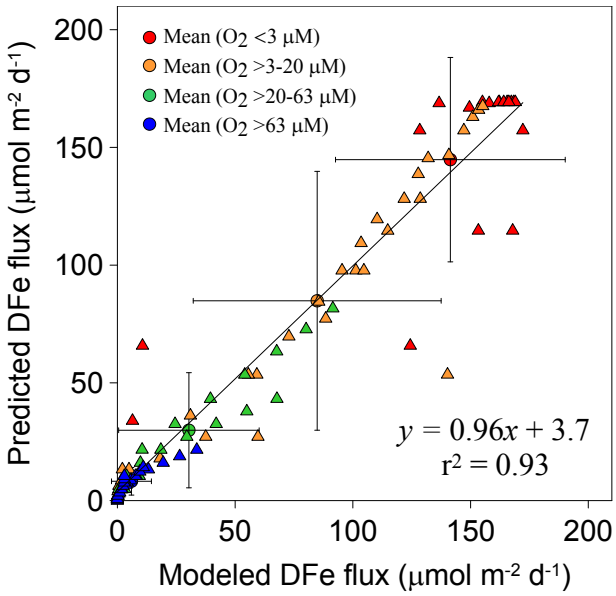

Figure 4.4: Comparison of the DFe fluxes simulated using the standardized numerical model for each paired O_{2BW}–C_{OX} data (black circles in Fig. 4.3) and the DFe fluxes predicted using Eq. 4.1, color-coded according to O_{2BW} (triangles). The large circles represent the mean flux ± s.d. in each O_{2BW} interval. The straight line is the linear regression curve (equation indicated).

The function is an example of a 0-D vertically-integrated sediment model, or Level 3 model following the criteria of Soetaert et al. (2000). Although the function is unable to simulate the local minimum of the DFe flux at low O_{2BW}, it broadly reproduces the hyperbolic trends in the sensitivity analysis results (dashed red curves, Fig. 4.3). A comparison of the new function with each paired C_{OX} and O_{2BW} point on these curves shows that it explains 93% of the variance in the modeled rates, with a standard error of the slope of 0.027 µmol m^{-2} d^{-1} (Fig. 4.4). C_{OX} and O_{2BW} alone each explain less than 20%. More complex functions did not improve the fit significantly.

The extreme DFe fluxes observed on the Peruvian shelf, Californian Borderland Basins and the Eel river mouth are not captured by the new function. One factor to consider may simply be that sediments display a wide range of reactive iron content. In our simulations we used a Fe_{HR}/Fe_T of 0.17, which is within the range of 0.08 – 0.40 for continental margin sediments (Raiswell and Canfield, 1998). Rivers tend to deposit large amounts of terrigenous inorganic material on the shelf which may be more enriched in Fe_{HR} compared to the global average (Poulton and Raiswell, 2002). We tested the sensitivity of DFe fluxes to the Fe_{HR} content by repeating the model simulations for the shelf site with 1 and 100 µM O_{2BW}. In these simulations, the total iron flux was held constant but the fluxes of Fe_{HR} and Fe_U were varied. The results show a quasi-linear dependence of benthic DFe fluxes on the Fe_{HR}/Fe_T ratio with a steeper response when O_{2BW} is in the normal oxic range

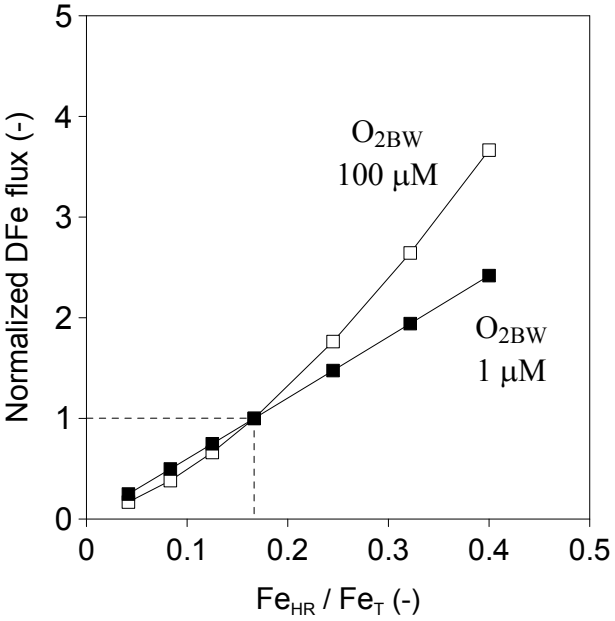

Figure 4.5: Sensitivity of modeled benthic DFe fluxes in shelf sediments to the Fe_{HR}/Fe_T ratio in particulate iron oxide deposited on the sea floor. Results are shown for low (1 µM) and high (100 µM) O_{2BW}. DFe fluxes are normalized to the modeled shelf fluxes in Fig. 4.1a for $O_{2BW} = 1$ and 100 µM, indicated by the dashed lines.

compared to the anoxic range (Fig. 4.5). The model predicts that the observed variability in Fe_{HR}/Fe_T for the Fe_T flux used in the simulations can result in DFe fluxes that vary by an order-of-magnitude. This supports the idea that high DFe fluxes on the Eel River shelf are driven by a higher-than-average Fe_{HR} content (Severmann et al., 2010) and, possibly, seasonal variability too (Severmann et al., 2010; Berelson et al., 2003; Pakhomova et al., 2007). Similarly, low DFe fluxes were calculated from pore water profiles in sediments with a low Fe_{HR} content on the South African margin (Homoky et al., 2013). Clearly, though, the total Fe_{HR} flux is the controlling factor on DFe flux rather than Fe_{HR}/Fe_T, the latter of which is likely to be determined by the weathering regime rather than the overall flux of terrigenous material.

By contrast, terrigenous Fe supply to the California Borderland Basins and the shallow Peruvian shelf is very low, despite Fe_{HR}/Fe_T within the range given by Raiswell and Canfield (1998). Extremely high benthic DFe fluxes in these regions may be caused by the transient occurrence of oxidizing conditions in the bottom water and the focused discharge of DFe after the recurrence of anoxia (Scholz et al., 2011; Noffke et al., 2012). The idea is that during oxic periods, a thin oxidized layer develops on the sediment surface which favors the precipitation of Fe oxides and mitigates DFe flux to the bottom water. Deposition of particulate Fe oxides from the water column would also be enhanced under these conditions. A resurgence of anoxic conditions favors reductive dissolution of the

accumulated oxides, leading to pulsed release of DFe to the bottom water. Moreover, iron fluxes in such temporally-anoxic and occasionally euxinic settings such as the Peruvian shelf may be largely influenced by additional controls such as the availability of sulfide in the pore water and bottom water and benthic boundary layer (Scholz et al., 2014a). These factors cannot be constrained with our benthic model, as we assume a bottom water sulfide concentration of zero in all model runs. More generally, the magnitude of the terrigenous Fe_{HR} flux and/or focused deposition of Fe oxides due to seasonal or other transient effects might play a more important role in generating the observed variability in benthic DFe fluxes than implied by the model.

4.6 A revised estimate for global benthic iron flux

Our new estimate of the global benthic DFe flux is based on spatially-resolved bathymetry, O_{2BW} and C_{OX} data. Maps of bathymetry and O_{2BW} on a 1°×1° resolution were taken from Bohlen et al. (2012) based on data from the World Ocean Atlas (Garcia et al., 2006). Gridded C_{OX} data are unavailable, and instead we used average C_{OX} for several hypsometric intervals (Burdige, 2007). Upscaling using the new function predicts a global DFe flux of 150 ± 75 Gmol yr^{-1} (Table 4.4), of which 109 ± 55 Gmol yr^{-1} is contributed by continental margin sediments and 41 ± 21 Gmol yr^{-1} by the deep sea (> 2000 m). The uncertainties are calculated assuming that variability in Fe_{HR}/Fe_T and Fe_T contribute the largest error in the model predictions (see Table 4.4). This is equivalent to 50% for margin and deep sea sediments. However, it is obvious from the scatter in Fig. 4.1 that there are other sources of variability in DFe fluxes. This is not surprising given the physical and biogeochemical heterogeneity of continental margin sediments, implying that the calculated uncertainty is a conservative estimate (Liu et al., 2010).

Note that the average DFe flux from deep-sea sediments is very low (0.37 µmol m^{-2} d^{-1}), yet globally significant by virtue of the vast expanse of the ocean basins. Nonetheless, this flux is speculative because very few flux measurements have been made in the ocean basins. Sequestration of DFe in deep-sea sediments may be more efficient than predicted, especially if other DFe removal pathways currently ignored in the model are significant, such as precipitation of authigenic carbonates, phosphates or silicates. Consequently, the data currently only support a global DFe flux of 109 Gmol yr^{-1}, but it may be higher, especially if non-reductive iron dissolution contributes significantly to the global Fe budget (Homoky et al., 2013; Conway and John, 2014). In fact, the Biogeochemical Elemental Cycling (BEC) ocean model that is tuned to pelagic DFe distribution does consider a very low DFe flux from the lower slope and deep basins (Moore and Braucher, 2008).

Table 4.4: Dissolved iron fluxes from marine sediments calculated using Eq. 4.1

	Area [a] (10^{12} m^2)	Mean C_{OX} [b] (mmol m^{-2} d^{-1})	Mean DFe flux [c] (µmol m^{-2} d^{-1})	Total DFe flux [d] (Gmol yr^{-1})	Total DFe flux [e] [*Elrod et al*. 2004] (Gmol yr^{-1})
			Continental margin		
Shelf (0-200m)	27.12	9.4	7.3	72.2 ± 36.1	63.3
Upper slope (>200-1000m)	16.01	3.0	3.5	20.5 ± 10.3	11.9
Lower slope (>1000-2000m)	15.84	1.5	2.9	16.6 ± 8.4	5.9
Total margin [f]	58.98 (0.38)	5.5	5.1 (35)	109 ± 55 (5)	81
			Deep sea		
>2000 m	302.5	0.4	0.37	41 ± 21	30
			Global ocean		
Σ				150 ± 75	111

[a] Menard and Smith (1966)

[b] Burdige (2007)

[c] Using the gridded O_{2BW} and bathymetry in combination with Eq. 4.1.

[d] Integrated over the corresponding ocean area. The uncertainties (±) are calculated based on the uncertainty in Fe_{HR} and Fe_T. Standard deviations in Fe_{HR} and Fe_T are reported for a mean marine sediment by (Poulton and Raiswell, 2002) (their Table 7). Using standard error propagation rules, the relative error in the Fe_{HR}/Fe_T ratio using their data is 50%, which is taken as the error in DFe flux.

[e] The flux calculated assuming the regression provided by Elrod et al. (2004) in Fig. 4.1. For consistency with Elrod et al. (2004), we used a flux ratio of 0.68 µmol DFe / mmol carbon oxidized in this calculation, ignoring the intercept DFe flux of 0.5 µmol m^{-2} d^{-1} in their linear regression equation.

[f] Values in parenthesis correspond to sediments underlying oxygen-deficient bottom waters (<20 µM).

Taking the lower global DFe flux of 109 Gmol yr^{-1}, our model suggests that two-thirds (72 Gmol yr^{-1}) is contributed by shelf sediments (Table 4.4). This is similar to 89 Gmol yr^{-1} derived by (Elrod et al., 2004) assuming a mean C_{OX} of 12 mmol m^{-2} d^{-1}. Our lower shelf C_{OX} (9.4 mmol m^{-2} d^{-1}) is derived from a well-constrained empirical relationship between C_{OX} and water depth (Burdige, 2007). Using Burdige's C_{OX} would decrease Elrod et al.'s shelf estimate by around one-third. Importantly, however, we find that continental slope sediments are also major sources of iron to ocean bottom waters (37.1 Gmol yr^{-1}). The implication is that sedimentary DFe release has been grossly underestimated in the marine Fe budget (Jickells et al., 2005; Boyd and Ellwood, 2010).

Our derived global flux is 3 to 14 times higher than most previous estimates (see Introduction). The average DFe flux from continental margins (5.1 µmol m^{-2} d^{-1}; Table 4.4) is also 3 to 5 times higher than the maximum benthic DFe flux of 1-2 µmol m^{-2} d^{-1} imposed as a seafloor boundary condition in some global iron models (e.g. Moore et al. (2004); Aumont and Bopp (2006)). One reason for the lower flux estimates from the global approaches may be an underestimation of organic carbon rain rates (Moore and Braucher, 2008). It would be interesting to compare carbon export fluxes from these models, but this data is unfortunately seldom reported. A more important consideration is that carbon rain rates and tracer distributions are generally poorly resolved over shelf sediments in global models, meaning that the shelf DFe flux (72.2 Gmol yr^{-1}), equivalent to two-thirds of the global sedimentary DFe release, is not properly accounted for. Instead, the models are tuned to the lower DFe fluxes from slope sediments. However, a fraction of the iron released from shelf sediments is not retained in coastal waters but exported offshore in both dissolved and particulate form (Johnson et al., 1999; Lam et al., 2006; Lohan and Bruland, 2008; De Jong et al., 2012). Too little export of coastal iron to the ocean basins may lead to a too strong dependence of surface iron concentrations on atmospheric iron deposition, thus influencing model sensitivity towards this source (Moore and Braucher, 2008; Tagliabue et al., 2014a).

An additional factor to consider that has been highlighted in this study is the role of bottom water oxygen concentration. Comparison of our DFe fluxes with those predicted by Elrod et al. (2004) using the same C_{OX} provides a broad overview of the effect of O_{2BW}. Most notably, we find that our DFe fluxes on the continental slope are 2-3 times higher than predicted by Elrod et al.'s function (Table 4.4). This is partly because oxygen-deficient waters of the eastern boundary upwelling systems tend to impinge on the seafloor at these depths (Helly and Levin, 2004). Sediments underlying bottom waters below the

20 µM threshold are flux hotspots, releasing DFe at an average rate of 35 µmol m^{-2} d^{-1}. They account for 4% of total DFe flux on the margin despite covering <1% of the seafloor. Yet, it should be noted that the relatively coarse 1°×1° resolution does not accurately capture shallow marginal sediments. Taking a more sophisticated approach, Helly and Levin (2004) estimated that around 1.4 × 1012 m^2 of sediments are in contact with bottom water <22 µM, which is equivalent to 3% by area of the shelf and upper slope (0-1000 m). Our DFe flux from oxygen-deficient regions is, therefore, likely to be a minimum estimate, and may be up to a factor of 3 higher.

4.7 Impact of benthic iron release on ocean dissolved iron distributions

The ability of our simple function to reproduce the observed fluxes is encouraging because it can easily be implemented in global biogeochemical models. Most models routinely simulate dissolved oxygen and organic carbon rain rates to the sea floor ($\approx C_{OX}$). Thus, it provides a straightforward tool to test how the spatial distribution of DFe in the ocean is impacted by benthic iron release.

We tested the impact of our predictive function on global iron distributions in the ocean using the University of Victoria Earth System Climate Model (UVic ESCM). This model includes a coupled physical biogeochemical ocean component with a dynamic iron cycle (Nickelsen et al., 2014). Like other global models, shelf processes are not adequately described due to the coarse spatial resolution. The model has two iron pools, dissolved and particulate, and is similar to other global iron models (e.g. Moore and Braucher (2008); Tagliabue et al. (2014a). Scavenging of iron from the water column by organic particles is tuned to provide a good correlation between observed and modeled surface ocean DFe distributions. The model does not include scavenging by resuspended inorganic particles. Sedimentary iron release is proportional to carbon oxidation rate (i.e. Elrod et al.'s function) and the model further uses a simple oxygen-dependent switch threshold of 5 µM. If bottom water O_2 falls below this value, all iron deposited on the seafloor is released back to the water column. Benthic DFe fluxes predicted by the UVic ESCM model are shown in Fig. 4.6a, and tuning of scavenging rates leads to a good fit to observed surface DFe concentrations (Fig. 4.6b). The global benthic DFe flux predicted by the model in this configuration is 19 Gmol yr^{-1} (Nickelsen et al., 2014).

Benthic DFe fluxes increase strongly in the Northern and Eastern Tropical Pacific, the Southern Ocean and the North Atlantic when the model is executed using our function with all other parameters held constant (Fig. 4.6c). The global DFe flux from sediments

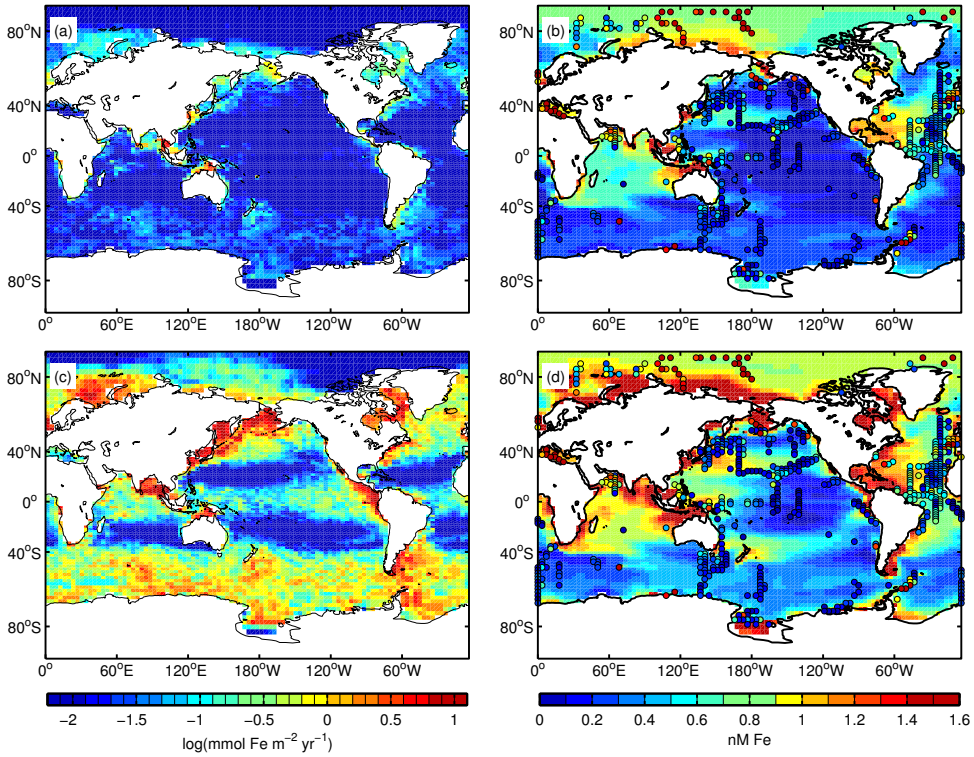

Figure 4.6: (a) Benthic DFe fluxes (mmol m^{-2} yr^{-1}, log-scale) and (b) surface ocean DFe distributions (nM) using the UVic ESCM model (from Nickelsen et al. (2014)). The results show the best model fit to observations (colored circles, Tagliabue et al. (2012)). (c) and (d) show the model results where the new function for benthic DFe flux (Eq. 4.1) is used to parameterize the benthic DFe flux, with all other model parameters held constant.

increases to 333 Gmol yr^{-1}, which is a factor of 2-3 higher than the predicted flux from the gridded data (Table 4.4). The elevated iron flux is caused by a positive feedback with POC rain rate to the seafloor driven by benthic Fe fertilization. Benthic DFe fluxes are thus enhanced in the new function configuration in otherwise iron-limited areas. Although scavenging depletes a fraction of the DFe released from the sediments, surface iron concentrations generally show a poorer agreement with the observations (Fig. 4.6d). DFe concentrations are also elevated in deep waters ($>$ 3000 m) by around 0.3 nM compared to observations (not shown). This model configuration would require much higher scavenging rates in order to bring the model predictions back in line with the observations. They would need to be four times higher to reduce the globally-averaged surface iron concentration from 0.83 nM to 0.48 nM, similar to previous 'best-fit' values of 0.41 nM (Fig. 4.6b).

The sensitivity of surface ocean DFe to benthic iron release suggests that the poorly-constrained scavenging rates are currently too low in state-of-the-art global iron models. DFe removal into organic/inorganic particulates or colloids very likely prevents a large

fraction of sedimentary iron reaching the surface ocean in a bioavailable form (Honeyman et al., 1988; Homoky et al., 2012; John et al., 2012). However, the model cannot currently resolve whether iron scavenging occurs close to the sediments or higher up in the water column. In reality, scavenging by inorganic particles is likely to be exacerbated in intermediate and bottom nepheloid layers on continental margins (Jahnke et al., 1990; Inthorn et al., 2006). In agreement with this, lateral relocation of sediment-derived Fe on the Peruvian margin appears to take place in colloids or nanoparticulates near the seafloor (Scholz et al., 2011). A fraction of iron scavenged within these layers may be exported offshore to distant Fe-limited regions, re-deposited on the seafloor or upwelled into surface waters (Johnson et al., 1999; Lam et al., 2006). Particle settling of inorganically-bound iron in addition to colloidal aggregation and pumping (Honeyman and Santschi, 1991) may be an important yet overlooked component of the marine Fe budget. It is worth noting that organically-bound iron exported from the surface ocean to the sediments would support <5% of the measured DFe flux from the continental margins, given the C_{OX} rate in Table 4.4 and a molar Fe/C_{org} ratio of 20 µmol/mol (Wu and Boyle, 2002; Moore and Braucher, 2008).

We thus propose that there exists a rapid removal of benthic-derived DFe into colloidal or inorganic phases close to the seafloor in particle-rich water layers. This serves as a barrier for sedimentary DFe reaching the surface mixed layer. Given that our benthic DFe fluxes are several-fold higher than those presently used in global iron models tuned to DFe distributions, the fraction of bioavailable iron that arrives at the sunlit ocean is probably much smaller than the fraction that is scavenged. Diagenetic alteration of iron particles and aggregates following deposition on the sediment allows DFe to be returned to the water column and re-scavenged. We believe that this cycle could be an important vector for transporting iron offshore away from the margins. Future studies should try to quantify these sources and sinks with the aim to improve the conceptual iron cycle in Earth system models.

4.8 Conclusions

The main objective of this study was to develop a simple, mathematical tool for predicting the flux of dissolved iron (DFe) from marine sediments and to better quantify its contribution to the global iron cycle. We derived an empirical function that unifies the role of bottom water oxygen concentration (O_{2BW}) and organic carbon oxidation rate in sediments (C_{OX}) as key controls on benthic DFe flux. The new function predicts a global DFe flux that is around five times higher than previous estimates derived using global models. This can be attributed to (i) inadequate treatment of the role of O_2 on benthic

DFe fluxes in global models, and (ii) poorly resolved biogeochemical dynamics on the shelf (for the sake of computational efficiency) where two-thirds of the global sedimentary DFe release occurs.

When the new function is applied to the state-of-the-art intermediate-complexity Earth system climate model UVic ESCM (Nickelsen et al., 2014), simulated surface water DFe concentrations are increased significantly over most of the ocean. This leads us to conclude that iron scavenging rates, mainly as inorganic particulates and colloidal aggregates close to the seafloor, must also be far higher than assumed previously. Otherwise, a strong positive feedback becomes established between primary productivity (hence C_{OX}) and DFe flux. The enhanced benthic DFe source may not have critical consequences for the current generation of ocean models if they correctly simulate the net flux of sediment iron that reaches the surface. However, the excess benthic iron that is scavenged close to the seabed is likely to be poorly represented. This could have important implications for the marine Fe budget as well as for simulating long-range transport of iron to Fe-limited regions. Once the significance of this 'dark' Fe cycle has been evaluated and parameterized more carefully, it would be interesting to test whether simulated atmospheric CO_2 concentrations during the Last Glacial Maximum are greatly diminished in global model simulations that employ our new benthic Fe input function (e.g. Parekh et al. (2006)).

Acknowledgements We thank the editorial team and two anonymous reviewers for their thoughtful comments. This work is a contribution of the Sonderforschungsbereich 754 "Climate - Biogeochemistry Interactions in the Tropical Ocean" (www.sfb754.de) financially supported by the Deutsche Forschungsgemeinschaft (DFG). The 7th Framework Program of the European Union supported the participation of FS (Marie Curie IOF #300648, BICYCLE). All field data used in this manuscript has been published previously and is directly obtainable from the literature cited in Table 4.1.

5 Riverine supply of iron is needed to sustain iron release from marine sediments in a global ocean biogeochemical model

This chapter is a manuscript in preparation by Nickelsen, L., Dale, A., Wallmann, K. and Oschlies, A. (2015).

Abstract Dissolved iron concentrations limit the growth of marine phytoplankton in large areas of the ocean. One major source of dissolved iron to the ocean is the release of iron from marine sediments. The sedimentary iron release does not only enhance coastal iron concentrations but also reaches the open ocean. However, the sources of reactive iron to the sediment are less clear. Observations suggest that lithogenic iron from rivers could be an important supply of iron to shelf sediments in some regions. Here we apply a recently developed transfer function for the release of iron from the sediment to a global ocean biogeochemical model. We can identify regions in which all reactive iron is lost from the sediment and regions in which sediment release is not dependent on the availability of reactive iron. Our results show that a riverine source of iron is neccessary as a source of reactive iron to the sediment to balance the release of dissolved iron from the sediment on a global scale. A sensitivity test reveals a strong sensitivity of export production and oxygen concentrations to the riverine iron source. This strong sensitivity could play an important role in determining the extent of oxygen minimum zones and the strength of the biological pump.

5.1 Introduction

Iron availability limits primary production in large areas of the Ocean (Moore et al., 2013). Multiple mesoscale iron fertilization experiments have shown strong blooming of phytoplankton in response to iron addition to surface waters in the Southern Ocean, equatorial Pacific and North Pacific (Boyd et al., 2000; Martin et al., 1994; Tsuda et al., 2003). The enhanced supply of iron to the Southern Ocean via strong dust deposition is also discussed to contribute to the variability of atmospheric CO_2 concentrations during glacial-interglacial cycles (Petit et al., 1999; Martínez-Garcia et al., 2011). Due to the short residence time of iron in the ocean of around 10-200 years (Moore and Braucher, 2008; Boyd and Ellwood, 2010; Nickelsen et al., 2014), iron concentrations in the ocean are strongly dependent on external supply via dust deposition, sediment release, hydrothermal release, riverine supply and release from ice-meltwater (Raiswell and Canfield, 2012, and references therein). Changes of these external sources can thus potentially strongly

affect primary production in the ocean. However, large uncertainties persist in the magnitude of the external sources as well as in the biogeochemical response to possible changes in the external sources (Tagliabue et al., 2014a).

Due to the iron hypothesis by Martin and Gordon (1990) who proposed that enhanced dust supply to the Southern Ocean could have contributed largely to the glacial CO_2 drawdown, dust deposition has been focused by many observational (e.g. Petit et al. (1999); Martinez-Garcia et al. (2014)) and modeling studies (e.g. Parekh et al. (2008); Tagliabue et al. (2008); Nickelsen and Oschlies (2015)). Over the last ten years, in contrast, sediment release has been recognized to also be a very important source of iron to the ocean (Moore and Braucher, 2008; Scholz et al., 2014a; Nickelsen et al., 2014; Dale et al., 2015), not only for coastal regions but also the open ocean (Elrod et al., 2004). Sediment release of iron was found to be predominantly controlled by the amount of organic carbon that sinks to the sediment and is oxidized therein (C_{ox}) (Elrod et al., 2004). However, the highest sedimentary iron fluxes were observed at very low bottom water oxygen concentrations, e.g. below 5 mmol m^{-3} (Noffke et al., 2012). Very high iron fluxes under low oxygen con centrations were also observed by Severmann et al. (2010) who studied the benthic iron flux at the Oregon-California continental shelf. Severmann et al. (2010) suggest that sediments on the shelf, which are influenced by high riverine iron discharge, are underestimated in their role in supplying iron to the ocean surface. Recently, Dale et al. (2015) examined 82 observations of sedimentary released iron and developed a new simple transfer function describing the sedimentary iron release as a function of oxygen and organic carbon rain rate (C_{ox}). This function can be readily applied to global ocean biogeochemical models that include an iron cycle. However, Dale et al. (2015) also note that the iron flux from the sediment is limited by the amount of reactive iron that is supplied to the sediment from the water column, possibly by rivers.

Global ocean biogeochemical models that include an iron cycle make use of various approaches to model the sediment source of iron. Tagliabue et al. (2014a) assume that C_{ox} is directly proportional to ocean depth and the primary driver of iron release. Hence, the sediment release in their model is only dependent on ocean depth and does not change in response to changes in the amount of C_{ox}. Moore and Braucher (2008) used the ratio of iron release to C_{ox} by Elrod et al. (2004). However, they also did not allow possible changes in C_{ox} to feedback on the iron release. Finally, Galbraith et al. (2010) and Nickelsen et al. (2014) also made the iron release dependent on C_{ox} as suggested by Elrod et al. (2004). In addition, they included a minimum concentration of oxygen, below which all particulate iron supplied to the sediment is released back to the water column. Here, we

apply the newly developed transfer function by Dale et al. (2015), which is based on multiple observations of iron release, and draw conclusions from this new empirical constraint for the oceanic iron cycle.

Although iron concentrations in river waters can be very high (e.g. 120 nM (Wetz et al., 2006)), it is not clear how much of that iron reaches the ocean and how strong the riverine iron influences coastal or maybe also open ocean biogeochemistry. As soon as salinity increases at the river mouth large parts of the iron quickly scavenges but a part may also contribute to the shelf iron inventory (Boyd and Ellwood, 2010). Hence, the role of the riverine source of iron to the ocean has been investigated only marginally so far. da Cunha and Buitenhuis (2013) account for a riverine source of iron in a regional high resolution modelling study in the tropical Atlantic and find that riverine iron supply is particularly important for sustaining nitrogen fixation. In a global modeling study about coastal nutrient supply, Cotrim da Cunha et al. (2007) find a high sensitivity of primary and export production to coastal phosphorus, iron and silicate supply, in particular in upwelling regions with high runoff but also generally in eastern margin seas. In a similar global modeling study Giraud et al. (2008) find that, compared to other nutrients, supply of iron from coastal processes (sediment or riverine supply) has the largest potential impact on open ocean biogeochemistry due to the fast scavenging of internal sources of dissolved iron. In this study we investigate the influence of the riverine supply of iron on iron concentrations in the ocean surface and the role of riverine iron in supplying reactive iron for the sedimentary iron release as suggested by Dale et al. (2015). We find that the sediment release is strongly dependent on the riverine source of iron and that iron concentrations as well as primary production and oxygen concentrations are highly sensitive to changes in riverine iron supply in some regions.

5.2 Methods

The model used is the University of Victoria (UVic 2.9) Earth System Climate Model Weaver et al. (2001) in the configuration described by Keller et al. (2012); Nickelsen et al. (2014) with a few minor adjustments described below. The model consists of three coupled components, 1) an atmospheric component with a simple one-layer energy-moisture balance model, 2) a land component that comprises a terrestrial model of vegetation and carbon cycle based on the Hadley Center model TRIFFID and a model with a heat and water exchange scheme, and 3) a three-dimensional ocean component that is based on the Modular Ocean Model 2 (MOM2) which includes a dynamic-thermodynamic sea-ice model. Prescribed winds are used to calculate momentum transfer to the ocean and sea-ice models as well as to calculate water vapor transport in the atmosphere. The ocean

component has 19 vertical levels with increasing thickness of the model boxes from the surface (50 m) to the deep ocean (500 m). The horizontal resolution of all components is 3.6° in longitudinal direction and 1.8° in latitudinal direction. Heat and water exchange is calculated between all components.

The marine biogeochemical model is described in detail in Keller et al. (2012) and the configuration with a dynamic iron cycle used here is described in Nickelsen et al. (2014). In brief, the model is nitrogen-based and has three dissolved inorganic nutrients: phosphate (PO_4), nitrate (NO_3) and dissolved iron (dFe) (Fig. 5.1). The nutrients are taken up by two different phytoplankton classes, diazotrophic phytoplankton that is capable of nitrogen fixation and a phytoplankton class that represents all other types of phytoplankton. Diazotrophs are not limited by nitrate, as they can fix N_2 from the atmosphere. A part of the phytoplankton biomass is quickly recycled to inorganic nutrients, representing the microbial loop and dissolved organic matter cycling. Zooplankton is represented by one model class and grazes on both phytoplankton classes, detritus, and themselves. Growth and assimilation efficiency terms determine the fraction of prey biomass that is assimilated into zooplankton biomass, respired, excreted or lost to detritus via sloppy feeding, egestion, and fecal pellet production. Detritus is build when phytoplankton is lyzed or dies, zooplankton grazes (sloppy feeding), and zooplankton dies. Detritus primarily sinks in the water column during which remineralization of detritus occurs but is also advected and diffused horizontally. To simulate benthic remineralization, all detritus is instantly converted back to inorganic nutrients and carbon at the seafloor. Oxygen is also a dynamically calculated tracer and is consumed during the remineralization of detritus. Representing the combined effects of denitrification and annamox, anaerobic remineratization sets in at rates 3 times slower than aerobic remineralization when oxygen levels fall below a threshold of 5 mmol m^{-3}. Dissolved inorganic carbon and alkalinity are also included in the model using fixed Redfield ratios between nitrogen and carbon.

A few minor model bugs were detected and corrected for the simulations here so that there are some small differences to the model description in Nickelsen et al. (2014). The bug fixes are 1) a corrected depth variable for the light attenuation calculation 2) double accounting of self-shading of phytoplankton is turned off, 3) the nitrogen fixation and denitrification impacts on alkalinity are now accounted for.

Since the agreement of simulated surface NO_3 and PO_4 concentrations to observations from the World Ocean Atlas (WOA) 2009 (Garcia et al., 2010b) decreased due to the bug fixes, we reduced the iron to carbon uptake ratio from 10 to 7 µmol Fe (mol C)$^{-1}$ which

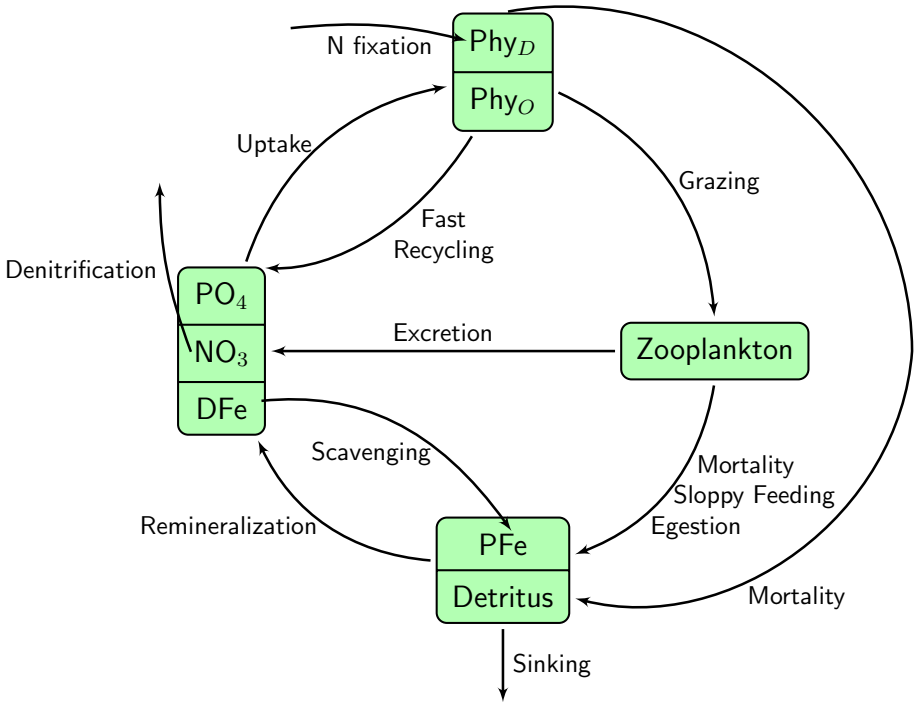

Figure 5.1: Schematic of the marine biogeochemical model used in this study. The abbreviations are: phosphate (PO_4), nitrate(NO_3), dissolved iron (DFe), particulate iron (PFe), ordinary phytoplankton (Phy_O) and diazotrophic phytoplankton (Phy_D).

is more in line with observed uptake ratios of 5 µmol Fe (mol C)$^{-1}$ (Johnson et al., 1997) and other modeling studies (7 µmol Fe (mol C)$^{-1}$ (Aumont et al., 2015)). The globally averaged vertical profiles of the model nutrients and tracers show that the differences of the control run here (CTL) to the version in Nickelsen et al. (2014) are very small (Fig. 5.2). Also the surface concentrations of PO_4 and NO_3 do only show a slight decrease from the Nickelsen et al. (2014) version to the CTL run used here (Fig. 5.3). The agreement to the WOA is very similar. Finally, there are also no noteworthy differences in the surface iron concentrations (Fig. 5.4).

The iron cycle consists of two model tracers, dissolved iron and particulate iron. Dissolved iron is assumed to be bioavailable and sums up free inorganic iron and iron bound to organic ligands. The ligand concentration is a globally fixed parameter of 1 nM and iron-ligand dynamics are calculated assuming an equilibrium between free iron, ligands and complexed iron as in Parekh et al. (2005); Galbraith et al. (2010). Particulate iron comprises iron that is scavenged and iron in organic particles that stems from phytoplankton or zooplankton. Only free iron is assumed to scavenge. The iron concentrations

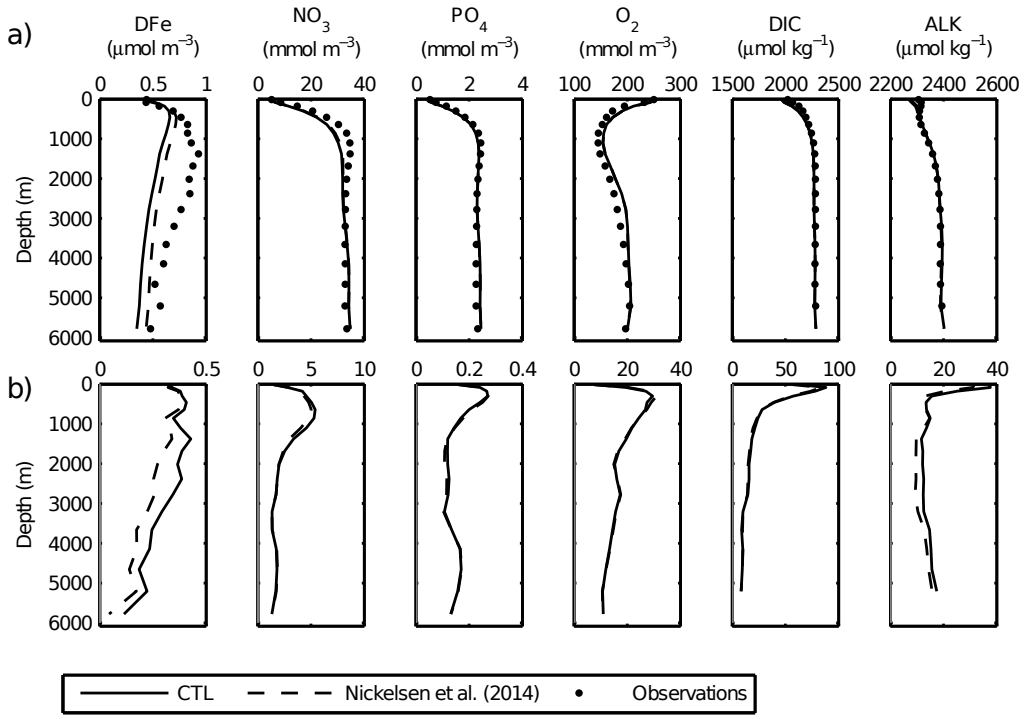

Figure 5.2: Vertical profiles comparing dissolved iron (DFe), nitrate (NO_3), phosphate (PO_4), oxygen (O_2), dissolved inorganic carbon (DIC) and alkalinity (ALK) with observations from Tagliabue et al. (2012), the World Ocean Atlas 2009 (Garcia et al., 2010b,a) and GLODAP (Key et al., 2004) **(a)** and vertical profiles of the horizontally averaged absolute differences between model and the observations **(b)** for the CTL simulation and the simulation in Nickelsen et al. (2014).

in the biological compartments of the model are calculated using a fixed ratio of iron to nitrogen. Dust deposition is accounted for with an atmospheric iron deposition map by Luo et al. (2008) with variable solubility. Fur further details about modeled iron cycle see Nickelsen et al. (2014).

The sediment release of iron in the CTL run of the model is parameterized by a ratio ($Fe\colon P_{sed}$) of iron released to particulate organic phosphorus sinking to the sediment (F_{POP}) and scaled with a temperature dependence ($\exp(T/T_b)$).

$$fe_{sed} = Fe\colon P_{sed} F_{POP} \exp(T/T_b) \qquad (O_2 > O_{2min}), \tag{5.1}$$

$$fe_{sed} = Fe\colon P_{sed} F_{POP} \exp(T/T_b) + F_{Fe_P} \qquad (O_2 \leq O_{2min}). \tag{5.2}$$

The flux of particulate iron to the sediment is denoted by F_{Fe_P}, T_b denotes a reference temperature and T the bottom water temperature. When bottom water oxygen concentrations fall below O_{2min}=5 mmol m^{-3} all particulate iron sinking to the sediment is released back to the water column. All particulate iron is assumed to be reactive iron in the model since we don't account for refractory iron bound for instance in silicate minerals

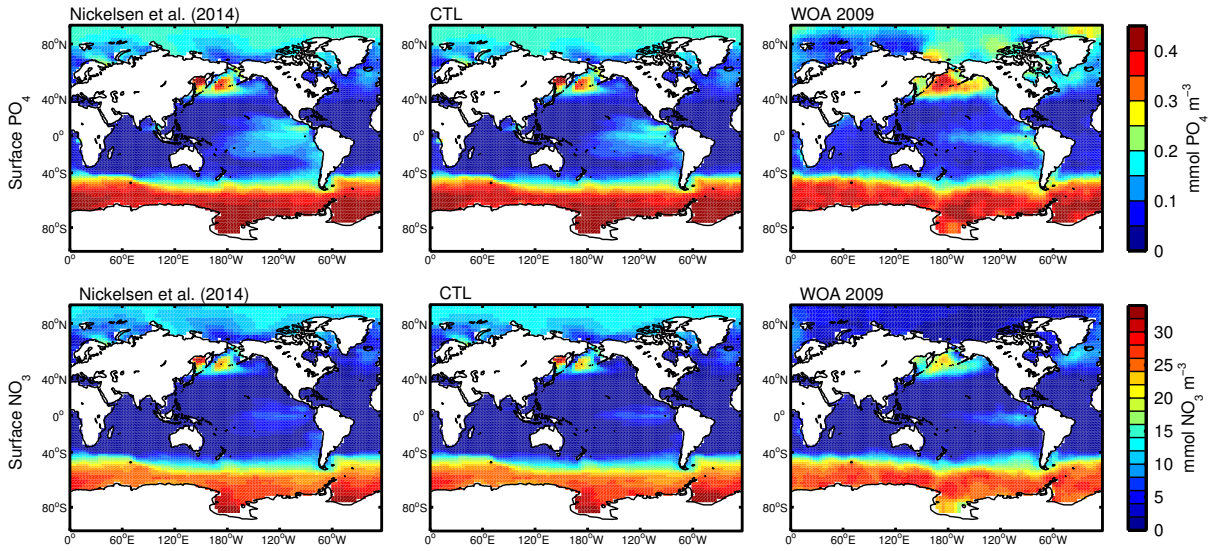

Figure 5.3: Annual mean surface phosphate (first row) and nitrate concentrations (second row) for the model version described in Nickelsen et al. (2014) and the CTL here in comparison to observations from the World Ocean Atlas 2009 (WOA, 2009) (Garcia et al., 2010a).

(Canfield et al., 1992).

The sediment release of iron using the transfer function developed by Dale et al. (2015) reads

$$fe_{sed} = \gamma \tanh(\frac{C_{ox}}{O_{2BW}}). \tag{5.3}$$

The amount of organic carbon that sinks to the sediment and is oxidized therein is denoted by C_{ox} and bottom water oxygen concentrations are denoted by O_{2BW}. The model experiment using this transfer function is denoted TFNOBAL (transfer function with no sediment iron balance) in the following. A further experiment with an assumed instantaneous balance of iron supplied and released from the sediment is denoted TFBAL. The sediment release for this reads

$$fe_{sed} = \min(\gamma \tanh(\frac{C_{ox}}{O_{2BW}}), F_{Fe_P}) \tag{5.4}$$

with the variables defined as before. In this experiment the sediment release is thus not only dependent on C_{ox} and O_{2BW} but also limited by the supply of reactive iron species that sink to the sediment. This particulate iron is generated biologically by incorporation of iron into organic matter and abiotically by scavenging of dissolved iron.

To test the influence by a riverine source of reactive iron to the sediment, we make use of

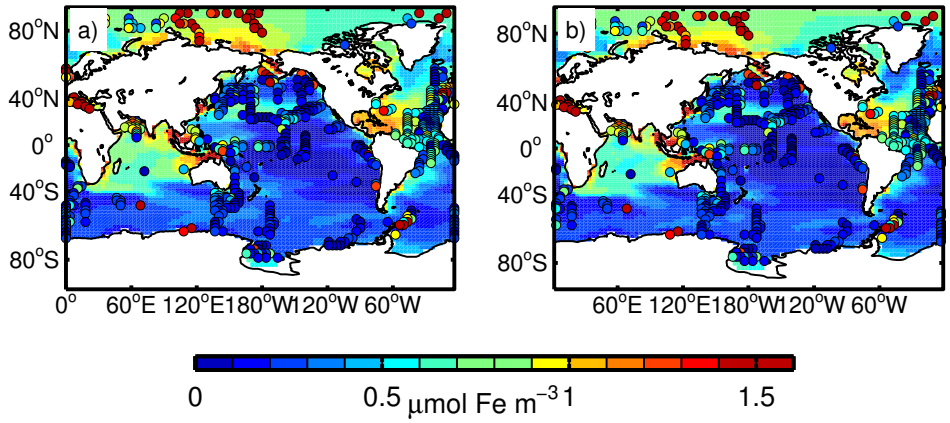

Figure 5.4: Annual mean surface iron concentrations **(a)** as simulated with the in the CTL run here and **(b)** as simulated in Nickelsen et al. (2014). Observations compiled by Tagliabue et al. (2012) are averaged over the first 50 m and plotted as colored circles on top.

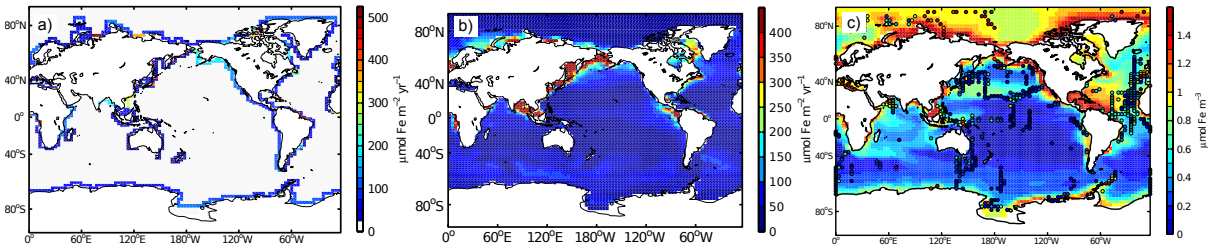

Figure 5.5: Annual means of the riverine iron supply **(a)**, sediment release **(b)** and surface iron concentrations with observations from Tagliabue et al. (2012) averaged over the top 50 m plotted on top **(c)** simulated with the new transfer function, balanced sediment and a riverine source of iron (experiment TFBALRIV).

the simulated fresh water supply to the ocean provided by the model (model experiment TFBALRIV). In the model all precipitation on land is distributed into drainage regions and rivers. This occurs according to a given map of supply regions based on topography (for further details see Weaver et al. (2001)). We assume a globally fixed iron concentration in rivers of 120 nM reported by Wetz et al. (2006) for the coastal ocean off Oregon, USA, during the winter. The resulting supply of iron by rivers to the ocean is shown in Fig. 5.5. In a sensitivity experiment we assume that 90% of the dissolved iron settles in the river before it reaches the ocean (experiment TFBALRIV12). In this experiment we thus apply a riverine iron concentration of 12 nM.

For a list of the model experiments see Table 5.1. All simulations are run for 1000 years which is enough for the iron cycle to equilibrate, given the short residence time of iron in the ocean. The drift in the globally averaged dissolved iron concentration is $<$ 0.01 nM and the drift in the globally averaged O_2 concentration is $<$ 1 mmol m^{-3} over

Table 5.1: Summary of the model experiments conducted, listing the experiment name, the equation used for the sediment release (equation), whether or not the sediment release is restricted to the availability of reactive iron (Balance), the concentration of dissolved iron in rivers (Riverine dFe), the globally integrated organic carbon supplied to the sediment (Int. C_{ox}), the globally averaged bottom water oxygen concentration (Avg. O_{2BW}) and the globally integrated flux of dissolved iron from the sediment (Sed. dFe flux).

Experiment name	Equation	Balance	Riverine dFe (nM)	Int. C_{ox} (Tmol C yr^{-1})	Avg. O_{2BW} (mmol O_2 m^{-3})	Sed. dFe flux (Gmol Fe yr^{-1})
CTL	(5.1)&(5.2)	no	0	112.2	188.4	19.1
TFNOBAL	(5.3)	no	0	109.6	171.8	220.6
TFBAL	(5.4)	yes	0	66.3	218.6	4.8
TFBALRIV	(5.4)	yes	120	104.0	181.9	19.3
TFBALRIV12	(5.4)	yes	12	85.4	210.3	6.0

the last 100 years of each simulation.

5.3 Results

Applying the new iron sediment transfer function leads to a strong overestimation of surface iron concentrations in our TFNOBAL simulation (Fig. 5.6). In particular, shallow regions show iron concentrations that reach concentrations of more than 1.2 nM. The root mean square error to the observations at the surface increases from 0.68 nM in the CTL simulation to 0.88 nM in the TFNOBAL simulation. Even in the Southern Ocean concentrations up to 0.6 nM are simulated. Due to the higher sedimentary iron release which is an order of magnitude higher than in the CTL simulation (Table 5.1) export production increases, which in turn decreases bottom water oxygen concentrations. The decreased O_{2BW} further increases the sedimentary iron release building a feedback mechanism that is partly responsible for the high simulated iron concentrations. However, the global value for C_{ox} decreases slightly in comparison to the CTL simulation (Table 5.1), indicating that the additionally exported organic matter is remineralized in the water column rather than the sediment.

In contrast, when the instantaneous sediment balance in the TFBAL simulation is assumed, iron concentrations are below 0.5 nM basically everywhere. The only exceptions are the dust deposition area in the tropical Atlantic, shallow regions or the high latitudes where light is the limiting factor. In the North Atlantic south of Iceland shallow water depths supply dissolved iron to the surface. However, due to the low surface iron concentrations, the globally integrated amount of organic carbon supplied to the sediment drops to around 50% of the value in the CTL simulation, and the globally integrated sedimentary iron release even drops to only 25% of the value in the CTL simulation (Table 5.1). The RMSE of the surface iron concentrations in the TFBAL simulation is 0.74 nM

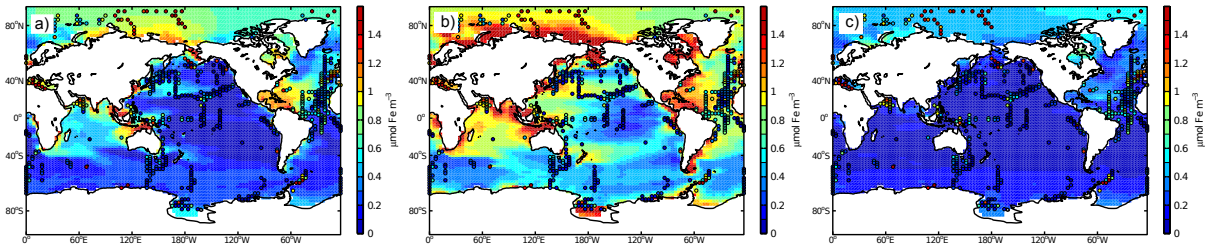

Figure 5.6: Annual mean surface iron concentrations with observations from Tagliabue et al. (2012) averaged over the top 50 m plotted on top. The control simulation (CTL) is shown in **a)**, the simulation with the new transfer function and no iron sediment balance (TFNOBAL) assumed **b)**, the simulation with the new transfer function and iron sediment balance assumed (TFBAL) in **c)**.

and thus also clearly higher than the 0.68 nM of the CTL simulation. Neither of the TFNOBAL and TFBAL simulations can thus simulate iron concentrations in a reasonable agreement to the observations.

The strong influence of assuming a sediment balance indicates that at some regions more iron is released from the sediment than supplied to the sediment in the TFNOBAL simulation. These regions are particular the ones that are located in regions near simulated oxygen minimum zones (OMZ), such as in the eastern tropical Pacific, the eastern tropical south Atlantic and the Bay of Bengal (Fig. 5.7). The wrong allocation of the Arabian Sea OMZ in the Bay of Bengal is a common model error that also exists in our model (Nickelsen et al., 2014). Due to the dependence of the transfer function on bottom water oxygen concentrations, outgoing sediment fluxes in these regions are much higher than the reactive iron supplied to the sediment. A net accumulation of iron in the sediment occurs in the regions that surround the iron source regions near the OMZs. However, also in other coastal and shallow regions sediment release is often larger than the reactive iron supplied to the sediment.

A correct representation of the sedimentary iron release with mass balance thus requires a good description of the particulate iron supply to the coastal regions, particular in the oxygen minimum zones. As mentioned by Boyd and Ellwood (2010) and Severmann et al. (2010) rivers could be an important source of reactive iron to the shelf regions. We test this by assuming an iron concentration in rivers of 120 nM (Wetz et al., 2006) in our model in experiment TFBALRIV. The riverine source of iron is highest at the Amazonas but also along the eastern coast of Asia where large rivers locally supply fresh water to the North Pacific (Fig. 5.5). The sediment release of iron shows similar global patterns than the riverine supply. For instance, iron supplied by the Amazonas seems to be rereleased by the sediment. In the western north Pacific levels of sediment release are high as well.

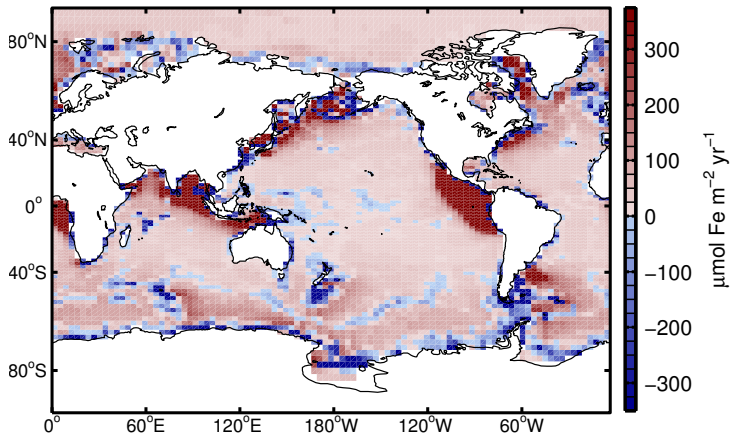

Figure 5.7: Annual mean sediment balance of iron, i.e. particulate iron sinking to the sediment minus iron release from the sediment in the simulation with the new transfer function and no sediment balance assumed (experiment TFNOBAL).

Regions near simulated OMZs in the tropical eastern Pacific, Bay of Bengal and eastern tropical south Atlantic are also regions of high sediment release. Globally, the integrated values of carbon supplied to the sediment and sedimentary iron release are similar to the CTL simulation (Table 5.1). Together, the riverine and sediment sources of iron are large enough to sustain iron concentrations at the surface although the sediment balance is assumed. In the tropical Atlantic and Southern Ocean surface iron concentrations are even a little bit overestimated which could be due to uncertainties in scavenging rates and iron concentrations in rivers. The globally averaged vertical profile of dissolved iron of the TFBALRIV simulation seems to be improved compared to the control simulation (Fig. 5.8). However, the global RMSE only decreases from 0.63 nM in the control simulation to 0.61 nM in TFBALRIV. While below the surface the iron concentrations in the globally vertical profile are too constant, at the surface the averaged concentrations are in line with the observations. It is noteworthy that the scarcity of dissolved iron concentrations implies some uncertainty in the observations. To draw more significant conclusions more observations of dissolved iron concentrations are thus needed. Yet, in general, the riverine supply of iron increases the agreement to the observations largely.

To test the uncertainty that is associated with the riverine iron supply we conduct a simulation (experiment TFBALRIV12) assuming that 90% of the dissolved iron in rivers scavenges already within the river so that instead of 120 nM only 12 nM of iron reach the ocean. The impact of the 90 % reduction in riverine iron supply on the sediment release of iron is highest in the regions, in which sediment release was high in experiment TFBALRIV, namely close to the Amazonas, western north Pacific and the regions near the OMZs (Fig. 5.9). This indicates that the riverine iron supply may put a limit to the

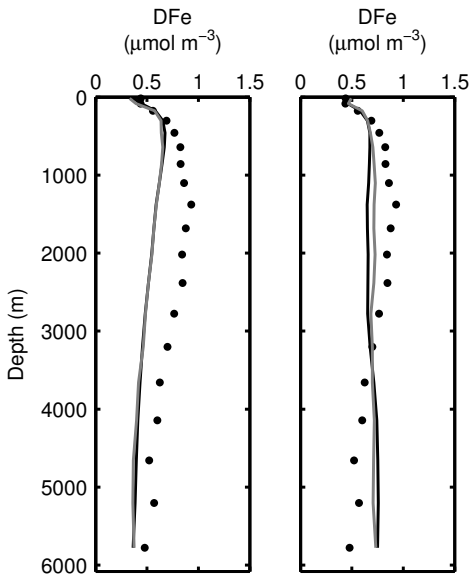

Figure 5.8: Annual mean globally horizontally averaged profiles of dissolved iron. The left panel shows the results of the CTL simulation, the right panel shows the results of the simulation with the new transfer function, balanced sediment and a riverine source of iron (experiment TFBALRIV) . Globally averaged observations are shown as dots. Globally averaged simulated iron concentrations are shown as black solid line while the gray line shows the simulated iron concentrations averaged only at the locations of the observations.

sediment release on a global scale, but in particular in the regions with a strong sediment source. The impact of the 90 % reduction of riverine iron supply on surface iron concentrations is highest in regions where iron is not limiting, i.e. in the tropical Atlantic, along the coast of the eastern Pacific and the coast of China (Fig. 5.10). In contrast, in the iron limited eastern tropical Pacific, Southern Ocean and western subarctic Pacific iron concentration were low already and do thus not change much. Due to the stronger iron limitation, phosphate concentrations show a global increase with a maximum of 1 mmol m^{-3} in the eastern tropical and subtropical Pacific. Accordingly, export production changes the most in the classical High-Nutrient Low-Chlorophyll regions, i.e. the Southern Ocean, tropical Pacific and Subarctic Pacific where macronutrients are available for phytoplankton. This has drastic consequences for the subsurface oxygen concentrations due to the altered amount of oxygen consumption during remineralization of the exported organic matter. The O_2 content of the eastern subtropical south Pacific is most sensitive to the changes in the riverine supply of iron, but also the whole tropical Pacific and Indian Ocean as well as subarctic Pacific show a strong increase in oxygen concentrations due to stronger iron limitation at the surface.

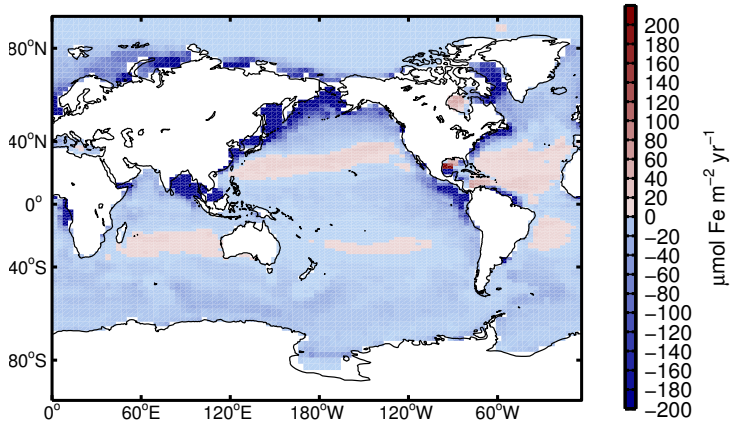

Figure 5.9: Difference of the sedimentary iron release between a simulation with an assumed riverine iron concentration of 12 nM (experiment TFBALRIV12) and a simulation with a riverine iron concentration of 120 nM (experiment TFBALRIV).

5.4 Discussion

5.4.1 Role of rivers in supplying reactive iron to the sediment

Our results indicate that the riverine iron supply is a very important source of reactive iron to the coastal sediment. In our simulations sedimentary iron release is widely dependent on the amount of reactive iron supplied to the sediment. Changes in organic matter or bottom water oxygen concentration could thus not alter the sedimentary iron release in these cases. In a further test simulation (not shown) we tested a four times increase of iron scavenging rates as in Dale et al. (2015). While this can decrease the high iron concentrations in the TFNOBAL simulation, the increase in scavenging does not supply enough reactive iron to sustain the sedimentary iron release in the TFBAL simulation. Instead, dissolved iron concentrations are even lower and the agreement to the observations gets worse. Our results of the role of rivers in supplying reactive iron to the sediment are supported by measurements of iron release from sediments along the Oregon-California continental shelf (Severmann et al., 2010). Severmann et al. (2010) suggest that sediments that are influenced by river discharge are underestimated in their role in supplying iron to the productive ocean surface. In a comparison of benthic iron fluxes to a sediment model, Dale et al. (2015) also find that sedimentary iron release is highly sensitive to the reactive iron supply to the sediment.

The simulated global flux of iron from the sediment is lower than the estimates of 89 and 150 Gmol Fe yr^{-1} from observational studies such as Elrod et al. (2004) and Dale et al. (2015) if the sediment release is dependent on the reactive iron supplied to the sediment (i.e. 19.3 Gmol Fe yr^{-1} in TFBALRIV). Sedimentary iron fluxes of up to 888

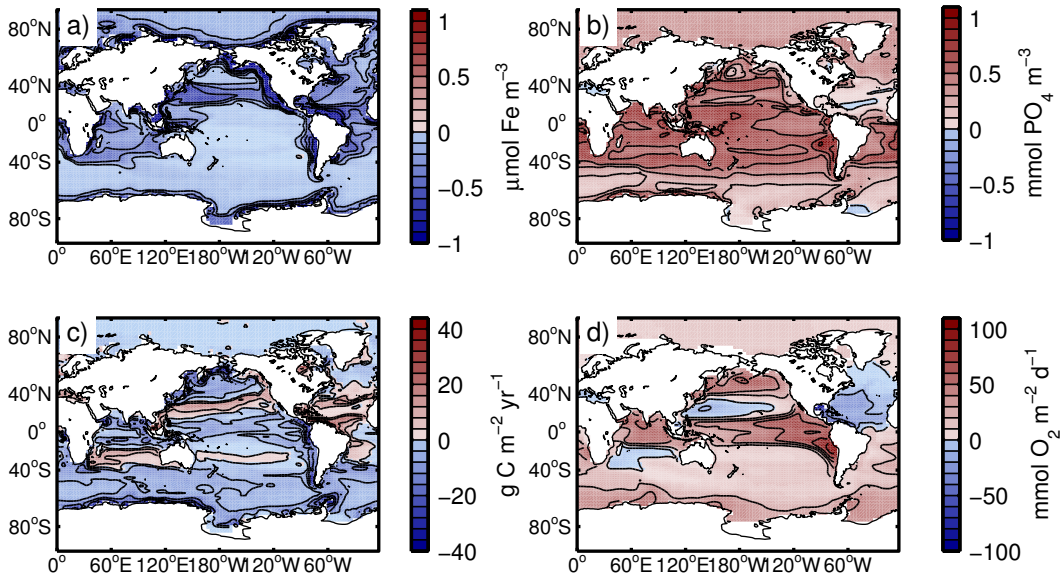

Figure 5.10: Difference of surface iron concentrations **(a)**, surface phosphate concentrations **(b)**, export production at 82.5 m depth **(c)**, oxygen concentrations at 302.5 m depth **(d)** between a simulation with an assumed riverine iron concentration of 12 nM (90 % loss before reaching the ocean) (experiment TFBALRIV12) and a simulation with a riverine iron concentration of 120 nM (experiment TFBALRIV).

µmol Fe m^{-2} d^{-1} at the Peruvian margin (Noffke et al., 2012), or fluxes of up to 568 µmol Fe m^{-2} d^{-1} at the Oregon-California shelf (Severmann et al., 2010) can also not be represented by the model. The maximum simulated fluxes are 7.6 µmol Fe m^{-2} d^{-1} occuring in the northern shelf regions of the Subarctic Pacific in the TFBALRIV simulation. At the Peruvian shelf and Oregon-California shelf sedimentary iron release does not exceed 0.05 µmol Fe m^{-2} d^{-1}. As discussed by Dale et al. (2015), one reason could be that shuttling of dissolved iron between the water column and sediments may take place within particle-rich nepheloid layers which the model does not simulate due to the coarse resolution. A model simulation with an adequate resolution at the shelf would be necessary to test if sedimentary iron fluxes increase with a description of resuspension and a better resolution of nepheloid layers.

While observations show not only high concentrations of dissolved iron but also transport of particulate iron in their river estuary (Wetz et al., 2006), we assume that the particulate iron is not transported far enough out of the estuary but instead settles already to the river or estuary bed. This is supported by observations of particulate iron speciation suggesting that most of the reactive iron species are deposited before reaching the ocean (Poulton and Raiswell, 2002). Even if some of the particulate iron would reach the open ocean, Poulton and Raiswell (2002) observe the fraction of reactive iron in riverine particulate iron to be small. Clearly, stream velocities in rivers decide on whether particulate

iron reaches the ocean or not. In particular, estuaries with their strong streamflow velocities are thus probably major sources of reactive iron to the ocean.

Another factor associated with the riverine supply is the location and magnitude of salt-induced flocculation and scavenging of iron. Boyle et al. (1977) and Sholkovitz (1978) suggest that 90% of the dissolved iron in rivers flocculates with increasing salinity until ocean conditions are reached. Whether the dissolved iron is flocculated already before it reaches the shelf or otherwise builds reactive iron that feeds the sedimentary iron pool is what decides on the role of riverine iron supply. More studies on the speciation and fate of riverine iron are thus necessary to better constrain the impact of riverine iron supply on the shelf sediment. However, it is promising that our simulated global riverine iron supply of 4 Gmol yr^{-1} already lies well within the range of observational estimates of global riverine iron supply of 1.6-6.4 Gmol yr^{-1} (Chester, 2000; Giraud et al., 2008).

Other sources of reactive iron to the shelf sediment could be atmospheric deposition of iron, hydrothermal vent release of iron and groundwater fluxes of dissolved iron. Atmospheric deposition of soluble iron is included in our model but deposition of reactive iron is until now not considered. However, Poulton and Raiswell (2002) compare estimates of reactive iron supply to coastal sediments and find that the riverine supply is one order of magnitude higher than supply by atmospheric deposition and hydrothermal vents. Iron is usually released too deep in the ocean and far enough away from coastal sediment. Groundwater fluxes of dissolved iron are also likely to provide only small fluxes of total iron but there is very little data of groundwater fluxes available (Poulton and Raiswell, 2002). Therefore, rivers are the most likely source of reactive iron to the shelf sediments.

Our results are supported by Chase et al. (2007) who analyze the variability of satellite chlorophyll data at the West Coast of North America and find that the variability can not be explained by river runoff alone. Instead, a combination of river runoff and shelf width can very well explain the variability of chlorophyll. Chase et al. (2007) attribute their results to the role of the shelf as a "capacitor" of iron supplied by rivers. The riverine supply of iron alone seems thus not to have a strong impact on coastal production. The sediment is needed as a reductive environment for the iron from rivers that scavenges at the increasing salinities. Our results show that this mechanism might not only apply to the West Coast of North America but play a role globally.

5.4.2 High sensitivity of upwelling regions and the open ocean

The high sensitivity of surface iron concentrations, export production and oxygen concentrations to riverine iron supply are due to the dependence of the sediment release on reactive iron in our model. As mentioned in the introduction, also other modeling studies find that primary and export production and oxygen concentrations are sensitive to riverine iron supply (Cotrim da Cunha et al., 2007; Giraud et al., 2008; da Cunha and Buitenhuis, 2013). Although these studies do not include a dependence of sedimentary iron release on reactive iron supply, they find a considerable sensitivity of primary and export production to coastal nutrient supply in particular in upwelling regions with high runoff. In upwelling regions the active transport of the sedimentary released iron to the surface increases the sensitivity to the sediment release. The active transport in upwelling regions can also partly explain the high sensitivity of export production and oxygen concentrations in our results. In our results the sensitivity is even higher due to the dependence of the sediment release on oxygen concentrations and organic carbon sinking to the sediment. In response to a decrease in riverine iron supply, a decrease in export production and an increase in oxygen concentrations further decrease the sediment release.

The impact of the lowered riverine iron supply that is not restricted to coastal regions but also influences open ocean iron concentrations in our results is still astonishing. Giraud et al. (2008) also find that coastal supply of iron has the strongest potential to influence open ocean biogeochemical conditions by determining the nutrient content in coastal waters that are transported offshore. We suggest that the strong impact of riverine and sediment iron sources on the open ocean is due to strong recycling of the supplied iron in our results. The rivers supply only 4 Gmol Fe yr^{-1} but the sediment release is increased from 4.5 to 19.3 Gmol Fe yr^{-1} from the TFBAL to the TFBALRIV simulation. This shows that the iron supplied from the rivers is released by the sediment, rescavenged or incorporated into phytoplankton biomass and then again supplied to the sediment multiple times. Similarly, from observing sediment trace metal concentrations and isotopic fractionation, Scholz et al. (2013) suggest that iron released from the shelf under low bottom water oxygen concentrations is quickly rescavenged and shuttled down to sediments further away from the coast. Via this "iron shuttle" not only coastal areas are affected by changes in sediment release but regions nearby as well. In the euphotic zone the strong recycling of iron is performed by bacteria and zooplankton. Roughly half of the uptake of iron is recycled at the surface in our model (Nickelsen et al., 2014). The strong recycling of iron in the euphotic zone was observed very early and is also termed the "ferrous wheel" (Kirchman, 1996; Boyd and Ellwood, 2010). During uptake and recycling the iron has time to be transported into nearby regions and offshore. Together, the "ferrous wheel" in

the euphotic zone and the "iron shuttle" in the sediment, can lead to the strong impact of the riverine supply on open ocean biogeochemistry.

5.4.3 Limitations of the model

The model provides continental runoff fluxes to the ocean calculated from the precipitation simulated by the model (Weaver et al., 2001) which may differ from other estimates of global fresh water supply to the ocean (e.g. Syvitski et al. (2005)). However, by relying on the internally provided runoff, changes in the amount and patterns of precipitation in for example a climate warming simulation could directly feedback on the riverine iron supply and sediment release. The continental runoff is also consistent with the rest of the model.

Sedimentary iron fluxes are dependent on the correct simulation of export production and oxygen concentrations. These are evaluated in Nickelsen et al. (2014) and do not change much to the CTL simulation here. The globally integrated supply of organic carbon to the sediment is 120 mol C yr^{-1} in Nickelsen et al. (2014), 112 mol C yr^{-1} in the CTL simulation and 105 mol C yr^{-1} in the TFBALRIV simulation here (Table 5.1). The oxygen concentrations are also very similar to the concentrations in Nickelsen et al. (2014) and the model does a reasonable job in representing the observations (Fig. 5.2). Yet, a higher resolution modeling study with a better representation of the oxygen minimum zones would be useful to better investigate local processes.

Due to the coarse resolution of the model, coastal regions are not resolved. Iron provided by the rivers is instantly diluted within the huge model boxes. Our results can show the potentially global significance of riverine iron supply as a source of reactive iron the sediment but high resolution models are needed for more precise estimates at single locations. A very interesting approach would be to even resolve the gradients of salinity and salt induced flocculation of iron colloids from a river estuary to the ocean. This would also allow to better quantify the reactive iron supply to the shelf.

Ligand concentrations are set to a global constant value of 1 nM everywhere. Buck et al. (2007) find that ligand concentrations strongly influence the amount of dissolved iron that reaches the ocean from rivers. The globally constant ligand concentration in our model could thus lead to a bias but dynamic ligand representations in global ocean biogeochemical models are still under development (Misumi et al., 2013; Völker and Tagliabue, 2014). The sources and sinks of iron-binding ligands are also still not fully understoond. In particular at river mouths where ligand concentrations decrease strongly due to floccu-

lation, ligand dynamics are further complicated. A better understanding of sources and sinks of ligands are thus necessary before taking spatial variable ligand concentrations into account for the estimation of the role of riverine iron.

Our results are produced assuming an instantaneous balance of the sources and sinks of iron to the sediment. Thus there is no simulated pool of iron in the sediment that could develop over time. With the use of a simple transfer function, only an instantaneous balance of iron in the sediment can be assumed. Iron from rivers are suggested to possibly be retained on the shelf during winter downwelling and support the entire summer bloom via upwelling at the northern California coast (Wetz et al., 2006). In our simulations seasonal variability may thus be too low at such settings because iron is not allowed to build up in the sediment. Scholz et al. (2011) analyzed trace metal distributions in the Peru upwelling area and suggest that interannual changes in bottom water oxygenation could lead to temporal accumulation and subsequent release pulses of iron. Yet, it remains to be tested how this would influence the transport of iron away from the sediment as much of the released iron could be readily rescavenged (Scholz et al., 2014a). Particularly for climate warming simulations, modeling a sediment pool of iron in the sediment could be an important next step for a subsequent study as C_{ox} and bottom water oxygen concentration would shift and lead to different accumulation patterns or rapid release of iron. Furthermore, this would also allow to study the anthropogenic influence on rivers via the construction of damns and rivers that decreases the load of sediment (and possibly iron) of rivers that is transported to the coast (Syvitski et al., 2005).

5.5 Conclusions

We find that applying a better constrained formulation for the sediment iron source leads to over- or underestimation of iron concentrations in the ocean, dependent on whether sediment release is restricted to available reactive iron in the sediment or not. Considering the availability of iron for the sediment release, the supply of reactive iron via rivers proves to be crucial for sustaining the sediment release of iron in our global ocean model. Through it's role in sustaining the sedimentary iron release, the riverine iron supply has a strong influence on coastal but also open ocean biogeochemistry. We suggest that the coastal iron supply influences the open ocean biogeochemistry via the strong recycling by bacteria and zooplankton at the ocean surface and via recycling of iron in the sediment. High resolution modeling and more observational studies are needed to determine whether the dissolved iron supplied by rivers is reaching the shelf in a reactive form and for confirming our results.

Acknowledgments We acknowledge financial support from the Deutsche Forschungsgemeinschaft (SFB 754). We thank Natalie Mahowald (Cornell University, Ithaca, USA) for sharing the dust deposition estimate.

6 Conclusions and Outlook

6.1 Conclusions

Throughout this thesis, the impact of changes in the external supply of iron by dust deposition, sediment release and rivers on marine biogeochemistry is found to be very strong. Although recent modeling studies suggested smaller sensitivities of ±2 µatm (Tagliabue et al., 2014a), in our simulations dust deposition estimates for past and future climate states changed the atmospheric CO_2 concentration by -22 and +28 µatm. The strong impact shows that there are still missing constraints in the rates in the iron cycle. However, the strong impact of dust deposition is also partly due to the representation of iron-light colimitation of phytoplankton growth in the simulations of this thesis. Growth limiting factors can have a huge impact on the outcome of simulations and sensitivity studies, particularly if they influence phytoplankton growth and export production in the Southern Ocean where deep water is formed and a potential long-time storage of nutrients and CO_2 exists.

The sedimentary iron release is shown to strongly influence surface iron concentrations and primary production. By comparison of model results to observations of iron concentrations, this thesis indicates that temperature might have an influence on sedimentary iron release. Prior to this thesis, an influence of temperature on the sedimentary iron release has not been considered in ocean biogeochemical models. However, the role of temperature on the sedimentary iron supply needs still to be confirmed by observations.

The application of a new description of the sedimentary iron release in a global biogeochemical ocean model provides new insights into the role of iron supply from the sediment. Firstly, due to the missing representation of nepheloid layers in coarse resolution models, sedimentary iron release and shuttling of iron between the water column and sediment might have been underestimated so far. Secondly, the riverine iron supply seems to be more important than assumed earlier because of its role in supplying reactive iron to the sediment. Through the supply of reactive iron to the sediment, rivers regulate the sedimentary iron release and strongly impact marine biogeochemistry. Overall, this thesis suggests that the role of the supply of iron from dust, sediment and rivers in marine biogeochemistry might have been underestimated.

The results presented in this thesis rely to a large part on the validation of model simulations by comparison to available observations of dissolved iron concentrations. These

observations are highly valuable for validation purposes, but they are still scarce. In many regions no observations of iron concentrations have been made or only the surface has been sampled. To further increase the performance of models in describing the iron concentrations, more observations are crucial (see also Achterberg (2014)). However, not only observations of iron concentrations are necessary. Observed iron concentrations are always a product of local source, sink and transport processes. For instance, observations of low iron concentrations can not solely be attributed to low sources of iron, but they could also derive from strong sinks. Therefore, it is necessary to measure not only iron concentrations but also rates of source and sink processes. In particular, ligand concentrations, scavenging rates and remineralization rates of iron are of high interest for modelling studies since they are still relatively unconstrained. Given the high sensitivity of marine biogeochemistry to changes in the external supplies of iron, more observations of sediment release rates, dust deposition rats and riverine supply could strongly inform biogeochemical models and the general understanding of the oceanic iron cycle.

6.2 Outlook

Dust deposition is found to correlate well with atmospheric CO_2 concentrations during past glacial-interglacial cycles (Petit et al., 1999). In many models dust deposition is not internally calculated but provided with a static forcing file so that dust and climate can not interact with each other. However, a feedback may emerge when a colder and drier climate increases arid areas on Earth. From the arid areas dust can be eroded and transported to the ocean. The enhanced dust supply could further cool down the climate via fertilizing the Southern Ocean with iron and increasing oceanic CO_2 uptake via the biological pump. To investigate the magnitude and properties of this feedback, a dust module could be implemented in the UVic model. The land surface scheme allows to determine the arid dust source regions and the prescribed winds can be used to simulate the dust transport in the atmosphere. Via the wind anomaly module, even adjustments of the winds to changes in climate could be simulated and would then affect the dust transport in the atmosphere again.

Sediment release of iron is highest at shallow shelf regions that experience high export production, low oxygen concentrations and the supply of reactive iron from rivers. Observations show that elevated iron concentrations at such shelfs can extend far offshore. A high resolution modeling study of the oxygen minimum zone in peruvian waters would thus be ideal to investigate the transport of sedimentary released iron to the open ocean. The role of eddies that trap low oxygen waters in transporting iron offshore could also be investigated.

A further subsequent study could address various theories that exist for the source of elevated Fe(II) concentrations that are observed at the upper boundary layer of the OMZs and in low oxygen waters in the North Pacific (e.g. Moffett et al. (2007); Hopkinson and Barbeau (2007); Schallenberg et al. (2015)). The observed Fe(II) is too far away to stem from the sediment. The theories to explain the Fe(II) concentrations include remineralization of organic matter (Schallenberg et al., 2015) and iron reduction as an acquisition strategy of microbes (Moffett et al., 2007). In a high resolution modeling study that also resolves the small timescales of Fe(II) oxidation, these theories could be tested and evaluated against observations of Fe(II) concentrations to identify which theory provides the most likely explanation for the elevated Fe(II) concentrations.

The results of chapter 5 show that in some regions all iron is lost from the sediment but there are also regions where more iron is supplied to the sediment than is released. In the model used in chapter 5 the sediment is not allowed to build up an iron inventory. Instead, excess iron supplied to the sediment is instantaneously lost to save computational efforts. However, if the sediment contains a pool of iron, this iron could be rapidly released as soon as the conditions change. For instance, a seasonal increase of organic matter rain rate, or a decrease of oxygen concentrations due to ENSO related fluctuations at the peruvian upwelling area (Scholz et al., 2011) could lead to a pulsed iron release from the sediment. Also the expansion of oxygen minimum zone with climate warming could lead to the mobilization of the iron inventory in the sediment. An implementation of a sediment iron inventory to the UVic model would allow to study the effect of such pulsed releases on marine biogeochemistry on the various time scales.

As shown in chapter 5, the supply of iron to the ocean shelf could have a strong impact on macronutrient concentrations and export production. However, the supply of iron via rivers to the ocean shelf is highly uncertain due to missing knowledge of the location of the settling of the flocculated iron. A high resolution study, resolving a well-studied river and its boundary to the ocean, could lead to important insights in the mechanisms and conditions that determine the riverine iron supply. The model could be validated against observed iron concentrations and sensitivities to the forcing conditions could be tested. Applying the resulting sensitivities to conditions at other river-ocean interfaces would allow to better estimate the riverine supply of iron to the ocean.

Although theoretically possible, surprisingly no nonlinear behavior has been found in biogeochemical models that are coupled to ocean models. In the iron cycle, a feedback

could exist between dust deposition and climate as explained earlier in this section. A further feedback could exist between export of organic matter from the surface and iron release from the sediment. An increase of sedimentary iron release could increase surface iron concentrations and stimulate the growth of phytoplankton, which could increase the export of organic matter from the surface to the sediment. The increased amount of organic matter further increases the iron release from the sediment and decreases oxygen concentrations, which would also increase the sediment release. Using a model that contains these feedbacks allows to investigate the existence of multiple steady states that are associated with these feedbacks. A wide range of initial conditions with different climate states could be tested to investigate whether they all equilibrate at the same climate state.

Bibliography

Achterberg EP (2014) Grand challenges in marine biogeochemistry. Frontiers in Marine Science 1(May):7, DOI 10.3389/fmars.2014.00007

Andersson JH (2004) Respiration patterns in the deep ocean. Geophysical Research Letters 31(3):1–4, DOI 10.1029/2003GL018756

Archer D, Johnson K (2000) A model of the iron cycle in the ocean. Global Biogeochemical Cycles 14(1):269–279, URL http://geosci.uchicago.edu/~archer/reprints/archer.2000.Fe_cycle.pdf

Arndt S, Jø rgensen B, LaRowe D, Middelburg J, Pancost R, Regnier P (2013) Quantifying the degradation of organic matter in marine sediments: A review and synthesis. Earth-Science Reviews 123:53–86, URL http://www.sciencedirect.com/science/article/pii/S0012825213000512

Arnosti C, Jø rgensen B, Sagemann J, Thamdrup B (1998) Temperature dependence of microbial degradation of organic matter in marine sediments: polysaccharide hydrolysis, oxygen consumption, and sulfate reduction. Marine Ecology Progress Series 165:59–70, URL http://www.int-res.com/abstracts/meps/v165/p59-70

Aumont O (2003) An ecosystem model of the global ocean including Fe, Si, P colimitations. Global Biogeochemical Cycles 17(2), DOI 10.1029/2001GB001745, URL http://www.agu.org/pubs/crossref/2003/2001GB001745.shtml

Aumont O, Bopp L (2006) Globalizing results from ocean in situ iron fertilization studies. Global Biogeochemical Cycles 20(2):1–15, DOI 10.1029/2005GB002591, URL http://www.agu.org/pubs/crossref/2006/2005GB002591.shtml

Aumont O, Ethé C, Tagliabue A, Bopp L, Gehlen M (2015) PISCES-v2 : an ocean biogeochemical model for carbon and ecosystem studies. Geoscientific Model Development Discussions 8:1375–1509, DOI 10.5194/gmdd-8-1375-2015

de Baar HJW, Boyd PW, Coale KH, Landry MR, Tsuda A, Assmy P, Bakker DCE, Bozec Y, Barber RT, Brzezinski MA, Buesseler KO, Boye M, Croot PL, Gervais F, Gorbunov MY, Harrison PJ, Hiscock WT, Laan P, Lancelot C, Law CS, Levasseur M, Marchetti A, Millero FJ, Nishioka J, Nojiri Y, van Oijen T, Riebesell U, Rijkenberg MJA, Saito H, Takeda S, Timmermans KR, Veldhuis MJW, Waite AM, Wong CS (2005) Synthesis of iron fertilization experiments: From the Iron Age in the Age of Enlightenment. Journal of Geophysical Research 110(C9):1–24, DOI 10.1029/2004JC002601, URL http://www.agu.org/pubs/crossref/2005/2004JC002601.shtml

Baker AR, Croot P (2010) Atmospheric and marine controls on aerosol iron solubility in seawater. Marine Chemistry 120(1-4):4–13, DOI 10.1016/j.marchem.2008.09.003, URL http://linkinghub.elsevier.com/retrieve/pii/S0304420308001461

Barbeau K (2006) Photochemistry of organic iron(III) complexing ligands in oceanic systems. Photochemistry and photobiology 82(6):1505–16, DOI 10.1562/2006-06-16-IR-935, URL http://www.ncbi.nlm.nih.gov/pubmed/16968114

Barber J (2008) Photosynthetic generation of oxygen. Philosophical transactions of the Royal Society of London Series B, Biological sciences 363(May):2665–2674, DOI 10.1098/rstb.2008.0047

Behrenfeld M, Milligan A (2013) Photophysiological expressions of iron stress in phytoplankton. Annual Review of Marine Science 5(January):217–246, DOI 10.1146/annurev-marine-121211-172356, URL http://www.ncbi.nlm.nih.gov/pubmed/22881354http://www.annualreviews.org/doi/abs/10.1146/annurev-marine-121211-172356

Behrenfeld M, Prasil O, Babin M, Bruyant F (2004) In search of a physiological basis for covariations in light-limited and light-saturated photosynthesis. Journal of Phycology 40(1):4–25, DOI 10.1046/j.1529-8817.2004.03083.x, URL http://doi.wiley.com/10.1046/j.1529-8817.2004.03083.xhttp://onlinelibrary.wiley.com/doi/10.1046/j.1529-8817.2004.03083.x/full

Behrenfeld MJ, Falkowski P (1997) Photosynthetic rates derived from satellite-based chlorophyll concentration. Limnology and Oceanography 42:1–20, URL http://terascan.smast.umassd.edu/nasdata/archive/Bisagni_Data/students/abrunner/MyDocuments/Classes/ECOS630/papers/Behrenfeld_andFalkowski_1997.pdf

Berelson W, McManus J, Coale K, Johnson K, Burdige D, Kilgore T, Colodner D, Chavez F, Kudela R, Boucher J (2003) A time series of benthic flux measurements from Monterey Bay, CA. Continental Shelf Research 23(5):457–481, DOI 10.1016/S0278-4343(03)00009-8

Berg P (2003) Dynamic Modeling of Early Diagenesis and Nutrient Cycling. A Case Study in an Artic Marine Sediment. American Journal of Science 303(10):905–955, DOI 10.2475/ajs.303.10.905

Berman-Frank I, Cullen JT, Shaked Y, Sherrell RM, Falkowski PG (2001) Iron availability, cellular iron quotas, and nitrogen fixation in Trichodesmium. Limnology and Oceanography 46(6):1249–1260, DOI 10.4319/lo.2001.46.6.1249, URL http://www.aslo.org/lo/toc/vol_46/issue_6/1249.html

Bhatia MP, Kujawinski EB, Das SB, Breier CF, Henderson PB, Charette Ma (2013) Greenland meltwater as a significant and potentially bioavailable source of iron to the ocean. Nature Geoscience 6(3):1–5, DOI 10.1038/ngeo1746, URL http://www.nature.com/doifinder/10.1038/ngeo1746

Blain S, Quéguiner B, Armand L, Belviso S, Bombled B, Bopp L, Bowie A, Brunet C, Brussaard C, Carlotti F, Christaki U, Corbière A, Durand I, Ebersbach F, Fuda JL, Garcia N, Gerringa L, Griffiths B, Guigue C, Guillerm C, Jacquet S, Jeandel C, Laan P, Lefèvre D, Lo Monaco C, Malits A, Mosseri J, Obernosterer I, Park YH, Picheral M, Pondaven P, Remenyi T, Sandroni V, Sarthou G, Savoye N, Scouarnec L, Souhaut M, Thuiller D, Timmermans K, Trull T, Uitz J, van Beek P, Veldhuis M, Vincent D, Viollier E, Vong L, Wagener T (2007) Effect of natural iron fertilization on carbon sequestration in the Southern Ocean. Nature 446(7139):1070–1074, DOI 10.1038/nature05700

Bohlen L, Dale aW, Sommer S, Mosch T, Hensen C, Noffke A, Scholz F, Wallmann K (2011) Benthic nitrogen cycling traversing the Peruvian oxygen minimum zone. Geochimica et Cosmochimica Acta 75(20):6094–6111, DOI 10.1016/j.gca.2011.08.010, URL http://linkinghub.elsevier.com/retrieve/pii/S0016703711004662http://dx.doi.org/10.1016/j.gca.2011.08.010

Bohlen L, Dale AW, Wallmann K (2012) Simple transfer functions for calculating benthic fixed nitrogen losses and C:N:P regeneration ratios in global biogeochemical models. Global Biogeochemical Cycles 26(3), DOI 10.1029/2011GB004198, URL http://www.agu.org/pubs/crossref/2012/2011GB004198.shtml

Bopp L, Kohfeld K, Le Quéré C, Aumont O (2003) Dust impact on marine biota and atmospheric CO2 during glacial periods. Paleoceanography 18(2), DOI 10.1029/2002PA000810, URL http://rem.sfu.ca/COPElab/Boppetal2003_paleoceanography.pdfhttp://onlinelibrary.wiley.com/doi/10.1029/2002PA000810/full

Boudreau BP (1996) A method-of-lines code for carbon and nutrient diagenesis in aquatic sediments. Comput Geosci 22:479–496

Boudreau BP, Ruddick BR (1991) On a reactive continuum representation of organic matter diagenesis. Am J Sci 291:507–538

Boudreau BP, Arnosti C, Jø rgensen BB, Canfield DE (2008) Comment on "Physical Model for the Decay and Preservation of Marine Organic Carbon". Science 319:1616– 1617

Bowie aR, Maldonado MT, Frew RD, Croot PL, Achterberg EP, Mantoura RFC, Worsfold PJ, Law CS, Boyd PW (2001) The fate of added iron during a mesoscale fertilisation experiment in the Southern Ocean. Deep-Sea Research Part II: Topical Studies in Oceanography 48:2703–2743, DOI 10.1016/S0967-0645(01)00015-7

Boyd PW, Ellwood MJ (2010) The biogeochemical cycle of iron in the ocean. Nature Geoscience 3(10):675–682, DOI 10.1038/ngeo964, URL http://www.nature.com/doifinder/10.1038/ngeo964

Boyd PW, Watson aJ, Law CS, Abraham ER, Trull T, Murdoch R, Bakker DC, Bowie aR, Buesseler KO, Chang H, Charette M, Croot P, Downing K, Frew R, Gall M, Hadfield M, Hall J, Harvey M, Jameson G, LaRoche J, Liddicoat M, Ling R, Maldonado MT, McKay RM, Nodder S, Pickmere S, Pridmore R, Rintoul S, Safi K, Sutton P, Strzepek R, Tanneberger K, Turner S, Waite A, Zeldis J (2000) A mesoscale phytoplankton bloom in the polar Southern Ocean stimulated by iron fertilization. Nature 407(6805):695–702, DOI 10.1038/35037500, URL http://www.ncbi.nlm.nih.gov/pubmed/11048709

Boyd PW, Jickells T, Law CS, Blain S, Boyle Ea, Buesseler KO, Coale KH, Cullen JJ, de Baar HJW, Follows M, Harvey M, Lancelot C, Levasseur M, Owens NPJ, Pollard R, Rivkin RB, Sarmiento J, Schoemann V, Smetacek V, Takeda S, Tsuda A, Turner S, Watson aJ (2007) Mesoscale iron enrichment experiments 1993-2005: synthesis and future directions. Science (New York, NY) 315(5812):612–7, DOI 10.1126/science.1131669, URL http://www.ncbi.nlm.nih.gov/pubmed/17272712

Boyd PW, Ibisanmi E, Sander SG, Hunter Ka, Jackson Ga (2010a) Remineralization of upper ocean particles: Implications for iron biogeochemistry. Limnology and Oceanography 55(3):1271–1288, DOI 10.4319/lo.2010.55.3.1271, URL http://www.aslo.org/lo/toc/vol_55/issue_3/1271.html

Boyd PW, Mackie D, Hunter K (2010b) Aerosol iron deposition to the surface ocean — Modes of iron supply and biological responses. Marine Chemistry 120(1-4):128–143, DOI 10.1016/j.marchem.2009.01.008, URL http://linkinghub.elsevier.com/retrieve/pii/S0304420309000103

Boyle E, Edmond J, Sholkovitz E (1977) The mechanism of iron removal in estuaries. Geochimica et Cosmochimica Acta 41(9):1313–1324, DOI 10.1016/0016-7037(77)90075-8

Breitbarth E, Achterberg EP, Ardelan MV, Baker aR, Bucciarelli E, Chever F, Croot PL, Duggen S, Gledhill M, Hassellöv M, Hassler C, Hoffmann LJ, Hunter Ka, Hutchins Da, Ingri J, Jickells T, Lohan MC, Nielsdóttir MC, Sarthou G, Schoemann V, Trapp JM, Turner DR, Ye Y (2010) Iron biogeochemistry across marine systems – progress from the past decade. Biogeosciences 7(3):1075–1097, DOI 10.5194/bg-7-1075-2010, URL http://www.biogeosciences.net/7/1075/2010/

Brovkin V, Ganopolski A, Archer D, Rahmstorf S (2007) Lowering of glacial atmospheric CO2 in response to changes in oceanic circulation and marine biogeochemistry. Paleoceanography 22(4):1–14, DOI 10.1029/2006PA001380, URL http://www.agu.org/pubs/crossref/2007/2006PA001380.shtmlhttp://onlinelibrary.wiley.com/doi/10.1029/2006PA001380/full

Bruland KW, Rue EL, Smith GJ, DiTullio GR (2005) Iron, macronutrients and diatom blooms in the Peru upwelling regime: brown and blue waters of Peru. Marine Chemistry 93(2-4):81–103, DOI 10.1016/j.marchem.2004.06.011, URL http://linkinghub.elsevier.com/retrieve/pii/S0304420304001859

Buck KN, Lohan MC, Berger CJM, Bruland KW (2007) Dissolved iron speciation in two distinct river plumes and an estuary: Implications for riverine iron supply. Limnology and Oceanography 52(2):843–855, DOI 10.4319/lo.2007.52.2.0843, URL http://www.aslo.org/lo/toc/vol_52/issue_2/0843.html

Buitenhuis ET, Hashioka T, Quéré CL (2013) Combined constraints on global ocean primary production using observations and models. Global Biogeochemical Cycles 2012(September), DOI 10.1002/gbc.20074, URL http://doi.wiley.com/10.1002/gbc.20074

Burdige DJ (2007) Preservation of organic matter in marine sediments: controls, mechanisms, and an imbalance in sediment organic carbon budgets? Chemical reviews 107(2):467–85, DOI 10.1021/cr050347q, URL http://www.ncbi.nlm.nih.gov/pubmed/17249736

Burwicz EB, Rüpke LH, Wallmann K (2011) Estimation of the global amount of submarine gas hydrates formed via microbial methane formation based on numerical reaction-transport modeling and a novel parameterization of Holocene sedimentation. Geochimica et Cosmochimica Acta 75(16):4562–4576, DOI 10.1016/j.gca.2011.05.029

Canfield DE, Raiswell R, Bottrell S (1992) The reactivity of sedimentary iron minerals toward sulfide. DOI 10.2475/ajs.292.9.659

Capone DG, Hutchins Da (2013) Microbial biogeochemistry of coastal upwelling regimes in a changing ocean. Nature Geoscience 6(9):711–717, DOI 10.1038/ngeo1916, URL http://www.nature.com/doifinder/10.1038/ngeo1916

Chase Z, Strutton PG, Hales B (2007) Iron links river runoff and shelf width to phytoplankton biomass along the U.S. West Coast. Geophysical Research Letters 34(4):10–13, DOI 10.1029/2006GL028069

Chester (2000) Marine Geochemistry, 2nd edn. Blackwell Science Ltd., Oxford, UK

Coale KH, Johnson KS, Fitzwater SE, Gordon RM, Tanner S, Chavez FP, Ferioli L, Sakamoto C, Rogers P, Millero F, Steinberg P, Nightingale P, Cooper D, Cochlan WP, Landry MR, Constantinou J, Rollwagen G, Trasvina a, Kudela R (1996) A massive phytoplankton bloom induced by an ecosystem-scale iron fertilization experiment in the equatorial Pacific Ocean. URL http://www.ncbi.nlm.nih.gov/pubmed/18680864

Colbert DL (2004) Geochemical Cycling in a Pacific Northwest Estuary (Tillamook Bay, Oregon, USA). Ph D dissertation, Oregon State University

Conway TM, John SG (2014) Quantification of dissolved iron sources to the North Atlantic Ocean. Nature 511(7508):212–215, DOI 10.1038/nature13482, URL http://www.nature.com/doifinder/10.1038/nature13482

Cornell RM, Schwertmann U (1996) The Iron Oxides: Structure, Properties, Reactions, Occurrences and Uses. Wiley-VCH, Darmstadt, Germany

Cotrim da Cunha L, Buitenhuis ET, Le Quéré C, Giraud X, Ludwig W (2007) Potential impact of changes in river nutrient supply on global ocean biogeochemistry. Global Biogeochemical Cycles 21(4):1–15, DOI 10.1029/2006GB002718

Cox PM (2001) Description of the TRIFFID dynamic global vegetation model. Technical Report Technical Note HCTN24(Hadley Centre):1–16, URL http://www.metoffice.gov.uk/media/pdf/9/h/HCTN_24.pdf

Cullen JT, Chong M, Ianson D (2009) GB4012 British columbian continental shelf as a source of dissolved iron to the subarctic northeast Pacific Ocean. Global Biogeochemical Cycles 23(4):1–12, DOI 10.1029/2008GB003326

da Cunha LC, Buitenhuis ET (2013) Riverine influence on the tropical Atlantic Ocean biogeochemistry. Biogeosciences 10(10):6357–6373, DOI 10.5194/bg-10-6357-2013, URL http://www.biogeosciences.net/10/6357/2013/

Dale AW, Brüchert V, Alperin M, Regnier P (2009) An integrated sulfur isotope model for Namibian shelf sediments. Geochimica et Cosmochimica Acta 73(7):1924–1944, DOI 10.1016/j.gca.2008.12.015

Dale AW, Bertics VJ, Treude T, Sommer S, Wallmann K (2013) Modeling benthic-pelagic nutrient exchange processes and porewater distributions in a seasonally-hypoxic sediment: evidence for massive phosphate release by Beggiatoa? DOI 10.5194/bgd-9-11517-2012

Dale AW, Nickelsen L, Scholz F, Hensen C, Oschlies A, Wallmann K (2015) A revised global estimate of dissolved iron fluxes from marine sediments. Global Biogeochemical Cycles accepted, DOI 10.1002/2014GB005017, URL http://doi.wiley.com/10.1002/2014GB005017

Davey M, Geider RJ (2001) Impact of iron limitation on the Photosynthetic Apparatus of the Diatom Chaetoceros Muelleri (Bacillariophyceae). Journal of Phycology 37(6):987–1000, DOI 10.1046/j.1529-8817.2001.99169.x, URL http://doi.wiley.com/10.1046/j.1529-8817.2001.99169.x

De Jong J, Schoemann V, Lannuzel D, Croot P, De Baar H, Tison JL (2012) Natural iron fertilization of the Atlantic sector of the Southern Ocean by continental shelf sources of the Antarctic Peninsula. Journal of Geophysical Research: Biogeosciences 117(1), DOI 10.1029/2011JG001679

DeVries T, Primeau F, Deutsch C (2012) The sequestration efficiency of the biological pump. Geophysical Research Letters 39(13):1–5, DOI 10.1029/2012GL051963, URL http://www.agu.org/pubs/crossref/2012/2012GL051963.shtml

Diaz RJ, Rosenberg R (1995) Marine benthic hypoxia: A review of its ecological effects and the behavioural responses of benthic macrofauna. Oceanography and Marine Biology - an Annual Review, Vol 33 33:245–303, URL <GotoISI>://A1995BE76V00004$\delimiter"026E30F$nhttp://www.csa.com/partners/viewrecord.php?requester=gs&collection=ENV&recid=4271242

Dietze H, Loeptien U (2013) Revisiting "nutrient trapping" in global coupled biogeochemical ocean circulation models. Global Biogeochemical Cycles 27(2):265–284, DOI 10.1002/gbc.20029, URL http://doi.wiley.com/10.1002/gbc.20029

Dunne JP, Armstrong RA, Gnanadesikan A, Sarmiento JL (2005) Empirical and mechanistic models for the particle export ratio. Global Biogeochemical Cycles 19(4):1–16, DOI 10.1029/2004GB002390, URL http://www.agu.org/pubs/crossref/2005/2004GB002390.shtml

Duteil O, Oschlies A (2011) Sensitivity of simulated extent and future evolution of marine suboxia to mixing intensity. Geophysical Research Letters 38(6):L06,607, DOI 10.1029/2011GL046877, URL http://www.agu.org/pubs/crossref/2011/2011GL046877.shtml

Eby M, Zickfeld K, Montenegro a, Archer D, Meissner KJ, Weaver AJ (2009) Lifetime of Anthropogenic Climate Change: Millennial Time Scales of Potential CO 2 and Surface Temperature Perturbations. Journal of Climate 22(10):2501–2511, DOI 10.1175/2008JCLI2554.1, URL http://journals.ametsoc.org/doi/abs/10.1175/2008JCLI2554.1

Eby M, Weaver AJ, Alexander K, Zickfeld K, Abe-Ouchi A, Cimatoribus AA, Crespin E, Drijfhout SS, Edwards NR, Eliseev AV, Feulner G, Fichefet T, Forest CE, Goosse H, Holden PB, Joos F, Kawamiya M, Kicklighter D, Kienert H, Matsumoto K, Mokhov II, Monier E, Olsen SM, Pedersen JOP, Perrette M, Philippon-Berthier G, Ridgwell A, Schlosser A, Schneider von Deimling T, Shaffer G, Smith RS, Spahni R, Sokolov aP, Steinacher M, Tachiiri K, Tokos K, Yoshimori M, Zeng N, Zhao F (2013) Historical and idealized climate model experiments: an intercomparison of Earth system models of intermediate complexity. Climate of the Past 9(3):1111–1140, DOI 10.5194/cp-9-1111-2013, URL http://www.clim-past.net/9/1111/2013/

Elrod Va, Berelson WM, Coale KH, Johnson K (2004) The flux of iron from continental shelf sediments: A missing source for global budgets. Geophysical Research Letters 31(12):2–5, DOI 10.1029/2004GL020216, URL http://www.agu.org/pubs/crossref/2004/2004GL020216.shtml

Eppley R (1972) Temperature and phytoplankton growth in the sea. Fish Bull 70(4):1063–1085, URL http://lgmacweb.env.uea.ac.uk/green_ocean/publications/Nano/Eppley72.pdf

Falkowski P, Barber R, Smetacek V (1998) Biogeochemical Controls and Feedbacks on Ocean Primary Production. Science (New York, NY) 281(5374):200–7, URL http://www.ncbi.nlm.nih.gov/pubmed/9660741

Feng Y, Hare C, Rose J, Handy S, DiTullio G, Lee P, Smith W, Peloquin J, Tozzi S, Sun J, Zhang Y, Dunbar R, Long M, Sohst B, Lohan M, Hutchins D (2010) Interactive effects of iron, irradiance and CO2 on Ross Sea phytoplankton. Deep Sea Research Part I: Oceanographic Research Papers 57(3):368–383, DOI 10.1016/j.dsr.2009.10.013, URL http://linkinghub.elsevier.com/retrieve/pii/S0967063709002258

Fernandez C, Farías L, Ulloa O (2011) Nitrogen fixation in denitrified marine waters. PloS one 6(6):e20,539, DOI 10.1371/journal.pone.0020539, URL http://www.pubmedcentral.nih.gov/articlerender.fcgi?artid=3110191&tool=pmcentrez&rendertype=abstract

Friedrich J, Dinkel C, Friedl G, Pimenov N, Wijsman J, Gomoiu MT, Cociasu a, Popa L, Wehrli B (2002) Benthic Nutrient Cycling and Diagenetic Pathways in the North-western Black Sea. Estuarine, Coastal and Shelf Science 54(3):369–383, DOI http://dx.doi.org/10.1006/ecss.2000.0653, URL http://www.sciencedirect.com/science/article/pii/S027277140090653X

Galbraith ED, Gnanadesikan A, Dunne JP, Hiscock MR (2010) Regional impacts of iron-light colimitation in a global biogeochemical model. Biogeosciences 7:1043–1064, URL http://adsabs.harvard.edu/abs/2010BGeo....7.1043G

Galbraith ED, Kwon EY, Gnanadesikan A, Rodgers KB, Griffies SM, Bianchi D, Sarmiento JL, Dunne JP, Simeon J, Slater RD, Wittenberg AT, Held IM (2011) Climate Variability and Radiocarbon in the CM2Mc Earth System Model. Journal of Climate 24(16):4230–4254, DOI 10.1175/2011JCLI3919.1, URL http://journals.ametsoc.org/doi/abs/10.1175/2011JCLI3919.1

Garcia HE, Locarnini RA, Boyer TP, Antonov JI (2006) World Ocean Atlas 2005, vol. 3, Dissolved Oxygen, Apparent Oxygen Utilization, and Oxygen Saturation, vol 63. NOAA, Silver Spring, USA

Garcia HE, Locarnini RA, Boyer TP, Antonov JI, Baranova OK, Zweng MM, Johnson DR (2010a) World Ocean Atlas 2009, Volume 3: Dissolved Oxygen, Apparent Oxygen Utilization, and Oxygen Saturation. S Levitus, Ed NOAA Atlas NESDIS 70, US Government Printing Office, Washington, DC p 344

Garcia HE, Locarnini RA, Boyer TP, Antonov JI, Zweng MM, Baranova OK, Johnson DR (2010b) World Ocean Atlas 2009, Volume 4: Nutrients (phosphate, nitrate, silicate). S Levitus, Ed NOAA Atlas NESDIS 71, US Government Printing Office, Washington, DC p 398

Garrels RM, Mackenzie FT (1971) Evolution of Sedimentary Rocks. Norton, New York

Geider RJ, MacIntyre HL, Kana TM (1997) Dynamic model of phytoplankton growth and acclimation : responses of the balanced growth rate and the chlorophyll a : carbon ratio to light, nutrient-limitation and temperature. Mar Ecol Prog Ser 148:187–200, DOI 10.3354/meps148187, URL http://www.int-res.com/abstracts/meps/v148/p187-200/

Gent P, Mcwilliams J (1990) Isopycnal mixing in ocean circulation models. Journal of Physical Oceanography URL http://journals.ametsoc.org/doi/abs/10.1175/1520-0485(1990)020%3C0150%3AIMIOCM%3E2.0.CO%3B2

Getzlaff J, Dietze H (2013) Effects of increased isopycnal diffusivity mimicking the unresolved equatorial intermediate current system in an earth system climate model. Geophysical Research Letters 40(10):2166–2170, DOI 10.1002/grl.50419, URL http://doi.wiley.com/10.1002/grl.50419

Ginoux P, Prospero J, Torres O, Chin M (2004) Long-term simulation of global dust distribution with the GOCART model: correlation with North Atlantic Oscillation. Environmental Modelling & Software 19(2):113–128, DOI 10.1016/S1364-8152(03)00114-2, URL http://linkinghub.elsevier.com/retrieve/pii/S1364815203001142

Giraud X, Le Quéré C, da Cunha LC (2008) Importance of coastal nutrient supply for global ocean biogeochemistry. Global Biogeochemical Cycles 22(2):1–15, DOI 10.1029/2006GB002717

Glasby GP (2006) Manganese: Predominant role of nodules and crusts. In: Zabel HDS, M (eds) Marine Geochemistry 2nd edition, Springer- Verlag, Berlin, Germany, pp 391–427

Gledhill M, Buck K (2012) The organic complexation of iron in the marine environment: a review. Frontiers in Microbiology 3(February):1–17, DOI 10.3389/fmicb.2012.00069, URL http://www.frontiersin.org/Microbiological_Chemistry/10.3389/fmicb.2012.00069/abstract

Greene RM, Geider RJ, Falkowski PG (1991) Effect of iron limitation on photosynthesis in a marine diatom. Limnology and Oceanography 36(8):1772–1782, DOI 10.4319/lo.1991.36.8.1772, URL http://www.aslo.org/lo/toc/vol_36/issue_8/1772.html

Griffies SM, Biastoch A, Böning C, Bryan F, Danabasoglu G, Chassignet EP, England MH, Gerdes R, Haak H, Hallberg RW, Hazeleger W, Jungclaus J, Large WG, Madec G, Pirani A, Samuels BL, Scheinert M, Gupta AS, Severijns CA, Simmons HL, Treguier AM, Winton M, Yeager S, Yin J (2009) Coordinated Ocean-ice Reference Experiments (COREs). Ocean Modelling 26(1-2):1–46, DOI 10.1016/j.ocemod.2008.08.007, URL http://linkinghub.elsevier.com/retrieve/pii/S1463500308001182

Hedges JI, Keil RG (1995) Sedimentary organic matter preservation: an assessment and speculative synthesis. DOI 10.1016/0304-4203(95)00013-H

Helly JJ, Levin La (2004) Global distribution of naturally occurring marine hypoxia on continental margins. Deep-Sea Research Part I: Oceanographic Research Papers 51(9):1159–1168, DOI 10.1016/j.dsr.2004.03.009

Herndl GJ, Reinthaler T (2013) Microbial control of the dark end of the biological pump. Nature geoscience 6(9):718–724, DOI 10.1038/ngeo1921, URL http://www.pubmedcentral.nih.gov/articlerender.fcgi?artid=3972885&tool=pmcentrez&rendertype=abstract

Homoky WB, Severmann S, McManus J, Berelson WM, Riedel TE, Statham PJ, Mills Ra (2012) Dissolved oxygen and suspended particles regulate the benthic flux of iron from continental margins. Marine Chemistry 134-135:59–70, DOI 10.1016/j.marchem.2012.03.003, URL http://dx.doi.org/10.1016/j.marchem.2012.03.003

Homoky WB, John SG, Conway TM, Mills Ra (2013) Distinct iron isotopic signatures and supply from marine sediment dissolution. Nature communications 4:2143, DOI 10.1038/ncomms3143, URL http://www.pubmedcentral.nih.gov/articlerender.fcgi?artid=3759054&tool=pmcentrez&rendertype=abstract

Honeyman BD, Santschi PH (1991) Coupling adsorption and particle aggregation: laboratory studies of "colloidal pumping" using iron-59-labeled hematite. Environmental Science & Technology 25(10):1739–1747, DOI 10.1021/es00022a010, URL http://pubs.acs.org/doi/abs/10.1021/es00022a010

Honeyman BD, Balistrieri L, Murray J (1988) Oceanic trace metal scavenging: the importance of particle concentration. Deep Sea Research Part A Oceanographic Research Papers 35(2):227–246, DOI 10.1016/0198-0149(88)90038-6, URL http://linkinghub.elsevier.com/retrieve/pii/0198014988900386

Honjo S, Manganini SJ, Krishfield RA, Francois R (2008) Particulate organic carbon fluxes to the ocean interior and factors controlling the biological pump : A synthesis of global sediment trap programs since 1983. Progress in Oceanography 76:217–285, DOI 10.1016/j.pocean.2007.11.003

Hopkinson B, Barbeau K (2007) Organic and redox speciation of iron in the eastern tropical North Pacific suboxic zone. Marine Chemistry 106(1-2):2–17, DOI 10.1016/j.marchem.2006.02.008, URL http://linkinghub.elsevier.com/retrieve/pii/S0304420306000430

Hopkinson B, Barbeau KA (2008) Interactive influences of iron and light limitation on phytoplankton at subsurface chlorophyll maxima in the eastern North Pacific. Limnology and Oceanography 53(4):1303–1318, URL http://www.jstor.org/stable/10.2307/40058253

Hopkinson B, Mitchell B, Reynolds R, Wang H, Selph K, Measures CI, Hewes C, Holm-Hansen O, Barbeau K (2007) Iron limitation across chlorophyll gradients in the southern Drake Passage: Phytoplankton responses to iron addition and photosynthetic indicators of iron stress. Limnology and Oceanography 52(6):2540–2554, URL http://www.jstor.org/stable/4502401

Inthorn M, Wagner T, Scheeder G, Zabel M (2006) Lateral transport controls distribution, quality, and burial of organic matter along continental slopes in high-productivity areas. Geology 34(3):205–208, DOI 10.1130/G22153.1

IPCC (2013) Working Group I Contribution to the IPCC Fifth Assessment Report, Climate Change 2013: The Physical Science Basis, vol AR5. Cambridge University Press

Jahnke RA, Reimers C, Craven DB (1990) Intensification of recycling of organic matter at the sea floor near ocean margins. DOI 10.1038/348050a0

Jeandel C, Peucker- Ehrenbrink BMTJ, Pearce CR, Oelkers EH, Godderis Y, Lacan F, Aumont O, Arsouze T (2011) Ocean Margins: The Missing Term in Oceanic Element Budgets? Eos 92(26):26–28, DOI 10.5194/bgd-

Jickells TD, An ZS, Andersen KK, Baker AR, Bergametti G, Brooks N, Cao JJ, Boyd PW, Duce RA, Hunter KA, Kawahata H, Kubilay N, LaRoche J, Liss PS, Mahowald N, Prospero JM, Ridgwell AJ, Tegen I, Torres R (2005) Global iron connections between desert dust, ocean biogeochemistry, and climate. Science (New York, NY) 308(5718):67–71, DOI 10.1126/science.1105959, URL http://www.ncbi.nlm.nih.gov/pubmed/15802595

John SG, Mendez J, Moffett J, Adkins J (2012) The flux of iron and iron isotopes from San Pedro Basin sediments. Geochimica et Cosmochimica Acta 93:14–29, DOI 10.1016/j.gca.2012.06.003, URL http://dx.doi.org/10.1016/j.gca.2012.06.003

Johnson K, Gordon R, Coale KH (1997) What controls dissolved iron concentrations in the world ocean? Marine Chemistry 57(3-4):181–186, DOI 10.1016/S0304-4203(97)00047-9, URL http://linkinghub.elsevier.com/retrieve/pii/S0304420397000431

Johnson KS, Chavez FP, Friederich GE (1999) Continental-shelf sediment as a primary source of iron for coastal phytoplankton. Nature 398(6729):697–700, DOI 10.1038/19511, URL <GotoISI>://WOS:000079920100047

Jones ME, Beckler JS, Taillefert M (2011) The flux of soluble organic-iron(III) complexes from sediments represents a source of stable iron(III) to estuarine waters and to the continental shelf. Limnology and Oceanography 56(5):1811–1823, DOI 10.4319/lo.2011.56.5.1811, URL http://www.aslo.org/lo/toc/vol_56/issue_5/1811.html

Keller D, Oschlies A, Eby M (2012) A new marine ecosystem model for the University of Victoria Earth system climate model. Geoscientific Model Development 5, URL http://eprints.ifm-geomar.de/14333/

Keller DP, Feng EY, Oschlies A (2014) Potential climate engineering effectiveness and side effects during a high carbon dioxide-emission scenario. Nature Communications 5, DOI 10.1038/ncomms4304, URL http://www.nature.com/doifinder/10.1038/ncomms4304

Key RM, Kozyr a, Sabine CL, Lee K, Wanninkhof R, Bullister JL, Feely Ra, Millero FJ, Mordy C, Peng TH (2004) A global ocean carbon climatology: Results from Global Data Analysis Project (GLODAP). Global Biogeochemical Cycles 18(4):n/a–n/a, DOI 10.1029/2004GB002247, URL http://doi.wiley.com/10.1029/2004GB002247

Kirchman DL (1996) Microbial ferrous wheel. DOI 10.1038/383303a0

Kraal P, Slomp C, Reed D (2012) Sedimentary phosphorus and iron cycling in and below the oxygen minimum zone of the northern Arabian Sea. Biogeosciences 9:3829–3880, DOI 10.5194/bgd-9-3829-2012, URL http://biogeosciences-discuss.net/9/3829/2012/bgd-9-3829-2012.pdf

Kriest I, Oschlies A (2008) On the treatment of particulate organic matter sinking in large-scale models of marine biogeochemical cycles. Biogeosciences Discussions 5(1):55–72, DOI 10.5194/bg-5-55-2008

Laglera LM, van den Berg CMG (2009) Evidence for geochemical control of iron by humic substances in seawater. Limnology and Oceanography 54(2):610–619, DOI 10.4319/lo.2009.54.2.0610

Lam PJ, Bishop JKB, Henning CC, Marcus Ma, Waychunas Ga, Fung IY (2006) Wintertime phytoplankton bloom in the subarctic Pacific supported by continental margin iron. Global Biogeochemical Cycles 20(1):1–12, DOI 10.1029/2005GB002557, URL http://www.agu.org/pubs/crossref/2006/2005GB002557.shtml

Landolfi A, Dietze H, Koeve W, Oschlies A (2013) Overlooked runaway feedback in the marine nitrogen cycle: the vicious cycle. Biogeosciences 10(3):1351–1363, DOI 10.5194/bg-10-1351-2013, URL http://www.biogeosciences.net/10/1351/2013/

Large WG, Danabasoglu G, McWilliams JC, Gent PR, Bryan FO (2001) Equatorial circulation of a global ocean climate model with anisotropic horizontal viscosity. Journal of Physical Oceanography 31:518–536, URL http://journals.ametsoc.org/doi/abs/10.1175/1520-0485(2001)031%3C0518:ECOAGO%3E2.0.CO;2

Levin LA, Gage JD (1998) Relationships between oxygen, organic matter and diversity of bathyal macrofauna. Deep-Sea Research Part II 45:129–163, URL papers://27281f87-3b7a-4de6-820c-ad3b64393d15/Paper/p3361

Lewandowski J, Laskov C, Hupfer M (2007) The relationship between Chironomus plumosus burrows and the spatial distribution of pore-water phosphate, iron and ammonium in lake sediments. Freshwater Biology 52(2):331–343

Liu KK, Atkinson L, Quinones R, Talaue-McManus L (2010) Carbon and Nutrient Fluxes in Continental Margins. A Global Synthesis. Springer-Verlag, Berlin, Heidelberg, Germany

Liu X, Millero F (2002) The solubility of iron in seawater. Marine Chemistry 77(1):43–54, DOI 10.1016/S0304-4203(01)00074-3, URL http://linkinghub.elsevier.com/retrieve/pii/S0304420301000743http://www.sciencedirect.com/science/article/pii/S0304420301000743

Lohan MC, Bruland KW (2008) Elevated Fe(II) and dissolved Fe in hypoxic shelf waters off Oregon and Washington: an enhanced source of iron to coastal upwelling regimes. Environmental science & technology 42(17):6462–8, URL http://www.ncbi.nlm.nih.gov/pubmed/18800515

Luo C, Mahowald NM, Bond T, Chuang PY, Artaxo P, Siefert RL, Chen Y, Schauer J (2008) Combustion iron distribution and deposition. Global Biogeochemical Cycles 22(1):1–17, DOI 10.1029/2007GB002964, URL http://www.agu.org/pubs/crossref/2008/2007GB002964.shtml

Maher B, Prospero J, Mackie D, Gaiero D, Hesse P, Balkanski Y (2010) Global connections between aeolian dust, climate and ocean biogeochemistry at the present day and at the last glacial maximum. Earth-Science Reviews 99(1-2):61–97, DOI 10.1016/j.earscirev.2009.12.001, URL http://linkinghub.elsevier.com/retrieve/pii/S0012825210000024

Mahowald NM, Baker AR, Bergametti G, Brooks N, Duce Ra, Jickells TD, Kubilay N, Prospero JM, Tegen I (2005) Atmospheric global dust cycle and iron inputs to the ocean. Global Biogeochemical Cycles 19(4), DOI 10.1029/2004GB002402, URL http://www.agu.org/pubs/crossref/2005/2004GB002402.shtml

Mahowald NM, Muhs DR, Levis S, Rasch PJ, Yoshioka M, Zender CS, Luo C (2006) Change in atmospheric mineral aerosols in response to climate: Last glacial period, preindustrial, modern, and doubled carbon dioxide climates. Journal of Geophysical Research 111(D10), DOI 10.1029/2005JD006653, URL http://www.agu.org/pubs/crossref/2006/2005JD006653.shtml

Mahowald NM, Engelstaedter S, Luo C, Sealy A, Artaxo P, Benitez-Nelson C, Bonnet S, Chen Y, Chuang PY, Cohen DD, Dulac F, Herut B, Johansen AM, Kubilay N, Losno R, Maenhaut W, Paytan A, Prospero JM, Shank LM, Siefert RL (2009) Atmospheric Iron Deposition: Global Distribution, Variability, and Human Perturbations. Annual Review of Marine Science 1(1):245–278, DOI 10.1146/annurev.marine.010908.163727, URL http://www.annualreviews.org/doi/abs/10.1146/annurev.marine.010908.163727

Mahowald NM, Kloster S, Engelstaedter S, Moore JK, Mukhopadhyay S, McConnell JR, Albani S, Doney SC, Bhattacharya A, Curran MAJ, Flanner MG, Hoffman FM, Lawrence DM, Lindsay K, Mayewski PA, Neff J, Rothenberg D, Thomas E, Thornton PE, Zender CS (2010) Observed 20th century desert dust variability: impact on climate and biogeochemistry. Atmospheric Chemistry and Physics 10(22):10,875–10,893, DOI 10.5194/acp-10-10875-2010, URL http://www.atmos-chem-phys.net/10/10875/2010/

Martin J, Gordon R (1990) Iron in Antarctic waters. Nature 345:156–158, URL http://www.nature.com/nature/journal/v345/n6271/abs/345156a0.html

Martin J, Coale K, Johnson K, Fitzwater S, Gordon R, Tanner S, Hunter C, Elrod V, Nowicki J, Coley T, Others (1994) Testing the iron hypothesis in ecosystems of the equatorial Pacific Ocean. Nature 371(6493):123–129, URL http://www.nature.com/nature/journal/v371/n6493/abs/371123a0.html

Martin JH (1990) Glacial-Interglacial CO2 change: the iron hypothesis. Paleoceanography 5(1):1–13, URL http://ocean.stanford.edu/bomc/Martin_1990.pdf

Martin JH, Fitzwater SE (1988) Iron deficiency limits phytoplankton growth in the north-east Pacific subarctic. Nature 331(6154):341–343, DOI 10.1038/331341a0, URL http://dx.doi.org/10.1038/331341a0

Martínez-Garcia A, Rosell-Melé A, Jaccard SL, Geibert W, Sigman DM, Haug GH (2011) Southern Ocean dust–climate coupling over the past four million years. Nature pp 1–5, DOI 10.1038/nature10310, URL http://www.nature.com/doifinder/10.1038/nature10310

Martinez-Garcia A, Sigman DM, Ren H, Anderson RF, Straub M, Hodell DA, Jaccard SL, Eglinton TI, Haug GH (2014) Iron Fertilization of the Subantarctic Ocean During the Last Ice Age. Science 343(6177):1347–1350, DOI 10.1126/science.1246848, URL http://www.sciencemag.org/cgi/doi/10.1126/science.1246848

McManus J, Berelson WM, Coale KH, Johnson KS, Kilgore T (1997) Phosphorus regeneration in continental margin sediments. Geochimica et Cosmochimica Acta 61(14):2891–2907, DOI 10.1016/S0016-7037(97)00138-5

Meile C, Van Cappellen P (2003) Global estimates of enhanced solute transport in marine sediments. Limnology and Oceanography 48(2):777–786, DOI 10.4319/lo.2003.48.2.0777

Meile C, Berg P, Van Cappellen P, Tuncay K (2005) Solute-specific pore water irrigation: Implications for chemical cycling in early diagenesis. Journal of Marine Research 63(3):601–621, DOI 10.1357/0022240054307885

Meinshausen M, Smith SJ, Calvin K, Daniel JS, Kainuma MLT, Lamarque JF, Matsumoto K, Montzka Sa, Raper SCB, Riahi K, Thomson a, Velders GJM, Vuuren DP (2011) The RCP greenhouse gas concentrations and their extensions from 1765 to 2300. Climatic Change 109(1-2):213–241, DOI 10.1007/s10584-011-0156-z, URL http://link.springer.com/10.1007/s10584-011-0156-z

Meissner KJ, Weaver AJ, Matthews HD, Cox PM (2003) The role of land surface dynamics in glacial inception: a study with the UVic Earth System Model. Climate Dynamics 21(7-8):515–537, DOI 10.1007/s00382-003-0352-2, URL http://link.springer.com/10.1007/s00382-003-0352-2

Menard HW, Smith SM (1966) Hypsometry of ocean basin provinces. Journal of Geophysical Research 71(18):4305–4325, DOI 10.1029/JZ071i018p04305, URL http://doi.wiley.com/10.1029/JZ071i018p04305

Middelburg JJ (1989) A simple rate model for organic matter decomposition in marine sediments. Geochimica et Cosmochimica Acta 53(7):1577–1581, DOI 10.1016/0016-7037(89)90239-1

Middelburg JJ, Levin La (2009) Coastal hypoxia and sediment biogeochemistry. Biogeosciences Discussions 6(2):3655–3706, DOI 10.5194/bgd-6-3655-2009

Middelburg JJ, Soetaert K, Herman PMJ (1997) Empirical relationships for use in global diagenetic models. DOI 10.1016/S0967-0637(96)00101-X

Mills M, Ridame C, Davey M, Roche JL, Geider RJ (2004) Iron and phosphorus co-limit nitrogen fixation in the eastern tropical North Atlantic. Nature 429(6989):292–294, URL http://cat.inist.fr/?aModele=afficheN&cpsidt=15783475http://www.nature.com/nature/journal/v429/n6989/abs/nature02550.html

Misumi K, Lindsay K, Moore JK, Doney SC, Tsumune D, Yoshida Y (2013) Humic substances may control dissolved iron distributions in the global ocean: Implications from numerical simulations. Global Biogeochemical Cycles 27(2):450–462, DOI 10.1002/gbc.20039, URL http://doi.wiley.com/10.1002/gbc.20039

Misumi K, Lindsay K, Moore JK, Doney SC, Bryan FO, Tsumune D, Yoshida Y (2014) The iron budget in ocean surface waters in the 20th and 21st centuries: projections by the Community Earth System Model version 1. Biogeosciences pp 33–55, DOI 10.5194/bg-11-33-2014, URL http://scholar.google.com/scholar?hl=en&btnG=Search&q=intitle:The+iron+budget+in+ocean+surface+waters+in+the+20th+and+21st+centuries+:+projections+by+the+Community+Earth+System+Model+version+1#0

Moffett JW, Goepfert TJ, Naqvi SWa (2007) Reduced iron associated with secondary nitrite maxima in the Arabian Sea. Deep Sea Research Part I: Oceanographic Research Papers 54(8):1341–1349, DOI 10.1016/j.dsr.2007.04.004, URL http://linkinghub.elsevier.com/retrieve/pii/S0967063707000969

Moore C, Seeyave S, Hickman A, Allen J, Lucas M, Planquette H, Pollard R, Poulton A (2007) Iron–light interactions during the CROZet natural iron bloom and EXport experiment (CROZEX) I: Phytoplankton growth and photophysiology. Deep Sea Research Part II: Topical Studies in Oceanography 54(18-20):2045–2065, DOI 10.1016/j.dsr2.2007.06.011, URL http://linkinghub.elsevier.com/retrieve/pii/S0967064507001488

Moore CM, Mills MM, Arrigo KR, Berman-Frank I, Bopp L, Boyd PW, Galbraith ED, Geider RJ, Guieu C, Jaccard SL, Jickells TD, La Roche J, Lenton TM, Mahowald NM, Marañón E, Marinov I, Moore JK, Nakatsuka T, Oschlies A, Saito Ma, Thingstad TF, Tsuda A, Ulloa O (2013) Processes and patterns of oceanic nutrient limitation. Nature Geoscience 6(March):1–10, DOI 10.1038/ngeo1765, URL http://www.nature.com/doifinder/10.1038/ngeo1765

Moore J, Doney S, Glover D, Fung I (2001) Iron cycling and nutrient-limitation patterns in surface waters of the World Ocean. Deep Sea Research Part II: Topical Studies in Oceanography 49(1-3):463–507, DOI 10.1016/S0967-0645(01)00109-6, URL http://linkinghub.elsevier.com/retrieve/pii/S0967064501001096

Moore JK, Braucher O (2008) Sedimentary and mineral dust sources of dissolved iron to the world ocean. Biogeosciences 5(3):631–656, DOI 10.5194/bg-5-631-2008, URL http://www.biogeosciences.net/5/631/2008/

Moore JK, Doney SC (2007) Iron availability limits the ocean nitrogen inventory stabilizing feedbacks between marine denitrification and nitrogen fixation. Global Biogeochemical Cycles 21(2):1–12, DOI 10.1029/2006GB002762, URL http://www.agu.org/pubs/crossref/2007/2006GB002762.shtml

Moore JK, Doney SC, Lindsay K (2004) Upper ocean ecosystem dynamics and iron cycling in a global three-dimensional model. Global Biogeochemical Cycles 18(4):n/a–n/a, DOI 10.1029/2004GB002220, URL http://doi.wiley.com/10.1029/2004GB002220

Najjar R, Sarmiento JL, Toggweiler JR (1992) Downward transport and fate of organic matter in the ocean: SImulations with a general circulation mdoel. Global Biogeochemical Cycles 6(1):45–76, URL http://onlinelibrary.wiley.com/doi/10.1029/91GB02718/full

Nickelsen L (2011) A model-based investigation of iron limitation of marine phytoplankton in High-Nutrient Low-Chlorophyll regions. Master thesis, Carl von Ossietzky-Universität Oldenburg, URL http://oceanrep.geomar.de/id/eprint/13965

Nickelsen L, Oschlies A (2015) Enhanced sensitivity of oceanic CO2 uptake to dust deposition by iron-light colimitation. Geophysical Research Letters 42:492–499, DOI 10.1002/2014GL062969, URL http://doi.wiley.com/10.1002/2014GL062969

Nickelsen L, Keller D, Oschlies A (2014) A dynamic marine iron cycle module coupled to the University of Victoria Earth System Model: the Kiel Marine Biogeochemical Model 2 (KMBM2) for UVic 2.9. Geoscientific Model Development Discussions 7(6):8505–8563, DOI 10.5194/gmdd-7-8505-2014, URL http://www.geosci-model-dev-discuss.net/7/8505/2014/

Noffke A, Hensen C, Sommer S, Scholz F, Bohlen L, Mosch T, Graco M, Wallmann K (2012) Benthic iron and phosphorus fluxes across the Peruvian oxygen minimum zone. Limnology and Oceanography 57(3):851–867, URL http://cat.inist.fr/?aModele=afficheN&cpsidt=26002210http://www.aslo.org/lo/pdf/vol_57/issue_3/0851.pdf

Oka A, Abe-Ouchi A, Chikamoto MO, Ide T (2011) Mechanisms controlling export production at the LGM: Effects of changes in oceanic physical fields and atmospheric dust deposition. Global Biogeochemical Cycles 25(2):1–12, DOI 10.1029/2009GB003628, URL http://www.agu.org/pubs/crossref/2011/2009GB003628.shtml

Oschlies A, Garçon V (1999) An eddy-permitting coupled physical-biological model of the North Atlantic: 1. Sensitivity to advection numerics and mixed layer physics. Global Biogeochemical Cycles 13(1):135–160, URL http://onlinelibrary.wiley.com/doi/10.1029/98GB02811/full

Pakhomova SV, Hall POJ, Kononets MY, Rozanov AG, Tengberg A, Vershinin AV (2007) Fluxes of iron and manganese across the sediment-water interface under various redox conditions. Marine Chemistry 107(3):319–331, DOI 10.1016/j.marchem.2007.06.001

Palastanga V, Slomp CP, Heinze C (2013) Glacial-interglacial variability in ocean oxygen and phosphorus in a global biogeochemical model. Biogeosciences 10(October):945–958, DOI 10.5194/bg-10-945-2013, URL http://adsabs.harvard.edu/abs/2013BGeo...10..945P

Parekh P, Follows MJ, Boyle EA (2004) Modeling the global ocean iron cycle. Global Biogeochemical Cycles 18(1):GB1002, DOI 10.1029/2003GB002061, URL http://www.agu.org/pubs/crossref/2004/2003GB002061.shtml

Parekh P, Follows MJ, Boyle EA (2005) Decoupling of iron and phosphate in the global ocean. Global Biogeochemical Cycles 19(2):GB2020, DOI 10.1029/2004GB002280, URL http://www.agu.org/pubs/crossref/2005/2004GB002280.shtml

Parekh P, Dutkiewicz S, Follows MJ, Ito T (2006) Atmospheric carbon dioxide in a less dusty world. Geophysical Research Letters 33(3):2–5, DOI 10.1029/2005GL025098, URL http://www.agu.org/pubs/crossref/2006/2005GL025098.shtml

Parekh P, Joos F, Müller SA (2008) A modeling assessment of the interplay between aeolian iron fluxes and iron-binding ligands in controlling carbon dioxide fluctuations during Antarctic warm events. Paleoceanography 23(4):1–14, DOI 10.1029/2007PA001531, URL http://192.102.233.13/journals/pa/pa0804/2007PA001531/2007PA001531.pdfhttp://www.agu.org/pubs/crossref/2008/2007PA001531.shtml

Petit J, Jouzel J, Raynaud D, Barkov N (1999) Climate and atmospheric history of the past 420,000 years from the Vostok ice core, Antarctica. Nature 399:429–436, URL http://www.daycreek.com/dc/images/1999.pdf

Poulton SW, Raiswell R (2002) The low-temperature geochemical cycle of iron: From continental fluxes to marine sediment deposition. American Journal of Science 302:774–805

Poulton SW, Krom MD, Raiswell R (2004) A revised scheme for the reactivity of iron (oxyhydr)oxide minerals towards dissolved sulfide. Geochimica et Cosmochimica Acta 68(18):3703–3715, DOI 10.1016/j.gca.2004.03.012

Price N (2005) The elemental stoichiometry and composition of an iron-limited diatom. Limnology and oceanography 50(4):1159–1171, URL http://www.jstor.org/stable/10.2307/3597395http://www.nospam.aslo.org/lo/toc/vol_50/issue_4/1159.pdf

Price N, Ahner B, Morel F (1994) The equatorial Pacific Ocean: Grazer-controlled phytoplankton populations in an iron-limited ecosystem. Limnology and Oceanography 39(3):520–534, URL http://www.jstor.org/stable/2838107http://www.princeton.edu/morel/publications/pdfs/priceLO1994.pdf

Radic A, Lacan F, Murray J (2011) Iron isotopes in the seawater of the equatorial Pacific Ocean: New constraints for the oceanic iron cycle. Earth and Planetary Science Letters DOI 10.1016/j.epsl.2011.03.015, URL http://linkinghub.elsevier.com/retrieve/pii/S0012821X11001592

Raiswell R, Canfield D (2012) The iron biogeochemical cycle past and present. Geochemical Perspectives 1(1), URL http://scholar.google.com/scholar?hl=en&btnG=Search&q=intitle:The+Iron+Biogeochemical+Cycle+Past+and+Present#0

Raiswell R, Canfield DE (1998) Sources of iron for pyrite formation in marine sediments. American Journal of Science 298(3):219–245, DOI 10.2475/ajs.298.3.219

Rickard D, Luther GW (2007) Chemistry of iron sulfides. Chemical Reviews 107(2):514–562, DOI 10.1021/cr0503658

Rijkenberg MJa, Steigenberger S, Powell CF, van Haren H, Patey MD, Baker AR, Achterberg EP (2012) Fluxes and distribution of dissolved iron in the eastern (sub-) tropical North Atlantic Ocean. Global Biogeochemical Cycles 26(3), DOI 10.1029/2011GB004264, URL http://www.agu.org/pubs/crossref/2012/2011GB004264.shtml

Rose AL, Waite TD (2003) Kinetics of hydrolysis and precipitation of ferric iron in seawater. Environmental Science and Technology 37(17):3897–3903, DOI 10.1021/es034102b

Rue E, Bruland K (1995) Complexation of iron (III) by natural organic ligands in the Central North Pacific as determined by a new competitive ligand equilibration/adsorptive cathodic stripping voltammetric method. Marine Chemistry 50(1-4):117–138, URL http://www.sciencedirect.com/science/article/pii/030442039500031L

Sabine CL, Feely R, Gruber N, Key RM, Lee K, Bullister JL, Wanninkhof R, Wong CS, Wallace DWR, Tilbrook B, Millero FJ, Peng TH, Kozyr A, Ono T, Rios AF (2004) The oceanic sink for anthropogenic CO2. Science 305(July):367–371, URL http://www.sciencemag.org/content/305/5682/367.short

Saito M, Goepfert T, Ritt J (2008) Some thoughts on the concept of colimitation: Three definitions and the importance of bioavailability. Limnology and Oceanography 53(1):276–290, URL http://222.aslo.org/lo/toc/vol_53/issue_1/0276.pdf

Saito Ma, Noble AE, Tagliabue A, Goepfert TJ, Lamborg CH, Jenkins WJ (2013) Slow-spreading submarine ridges in the South Atlantic as a significant oceanic iron source. Nature Geoscience 6(8):1–5, DOI 10.1038/ngeo1893, URL http://www.nature.com/doifinder/10.1038/ngeo1893

Sanz-Lázaro C, Valdemarsen T, Marín A, Holmer M (2011) Effect of temperature on biogeochemistry of marine organic-enriched systems: implications in a global warming scenario. Ecological Applications 21(7):2664–77, URL http://www.ncbi.nlm.nih.gov/pubmed/22073651

Sarmiento J, Gruber N (2002) Sinks for anthropgenic carbon. Physics Today 55:30–36, URL http://www.gfdl.gov/bibliography/related_files/jls0202.pdf

Sarmiento J, Gruber N (2006) Ocean biogeochemical dynamics. Princeton University Press, Princeton, USA, URL http://press.princeton.edu/titles/8223.html

Sarmiento JL, Orr JC (1991) Three-dimensional simulations of the impact of Southern Ocean nutrient depletion on atmospheric CO2 and ocean chemistry. Limnology and Oceanography 36(8):1928–1950, DOI 10.4319/lo.1991.36.8.1928

Schallenberg C, Davidson AB, Simpson KG, Miller La, Cullen JT (2015) Iron(II) variability in the northeast subarctic Pacific Ocean. Marine Chemistry accepted, DOI 10.1016/j.marchem.2015.04.004, URL http://linkinghub.elsevier.com/retrieve/pii/S0304420315000985

Schmittner A, Oschlies A, Giraud X, Eby M, Simmons HL (2005) A global model of the marine ecosystem for long-term simulations: Sensitivity to ocean mixing, buoyancy forcing, particle sinking, and dissolved organic matter cycling. Global Biogeochemical Cycles 19(3):1–17, DOI 10.1029/2004GB002283, URL http://www.agu.org/pubs/crossref/2005/2004GB002283.shtmlhttp://www.agu.org/journals/gb/gb0503/2004GB002283/2004gb002283-t02.txt

Schmittner A, Oschlies A, Matthews HD, Galbraith ED (2008) Future changes in climate, ocean circulation, ecosystems, and biogeochemical cycling simulated for a business-as-usual CO 2 emission scenario until year 4000 AD. Global Biogeochemical Cycles 22(1):1–21, DOI 10.1029/2007GB002953, URL http://www.agu.org/pubs/crossref/2008/2007GB002953.shtml

Schmittner A, Oschlies A, Damon Matthews H, Galbraith ED (2009) Correction to "Future changes in climate, ocean circulation, ecosystems, and biogeochemical cycling simulated for a business-as-usual CO 2 emission scenario until year 4000 AD". Global Biogeochemical Cycles 23(3):1–1, DOI 10.1029/2009GB003577, URL http://doi.wiley.com/10.1029/2009GB003577

Scholz F, Hensen C, Noffke A, Rohde A, Liebetrau V, Wallmann K (2011) Early diagenesis of redox-sensitive trace metals in the Peru upwelling area – response to ENSO-related oxygen fluctuations in the water column. Geochimica et Cosmochimica Acta 75(22):7257–7276, DOI 10.1016/j.gca.2011.08.007, URL http://linkinghub.elsevier.com/retrieve/pii/S0016703711004637

Scholz F, Severmann S, McManus J, Hensen C (2013) Beyond the Black Sea paradigm: The sedimentary fingerprint of an open-marine iron shuttle. Geochimica et Cosmochimica Acta DOI 10.1016/j.gca.2013.11.041, URL http://linkinghub.elsevier.com/retrieve/pii/S0016703713006807

Scholz F, McManus J, Mix A, Hensen C, Schneider RR (2014a) The impact of ocean deoxygenation on iron release from continental margin sediments. Nature Geoscience 7:433–437, DOI 10.1038/NGEO2162, URL http://www.nature.com/ngeo/journal/vaop/ncurrent/full/ngeo2162.html?WT.mc_id=TWT_NatureGeosci

Scholz F, Severmann S, McManus J, Noffke A, Lomnitz U, Hensen C (2014b) On the isotope composition of reactive iron in marine sediments: Redox-shuttle versus early diagenesis. Chemical Geology DOI 10.1016/j.chemgeo.2014.09.009, URL http://linkinghub.elsevier.com/retrieve/pii/S0009254114004264

Sedwick PN, DiTullio GR (1997) Regulation of algal blooms in Antarctic Shelf Waters by the release of iron from melting sea ice. Geophysical Research Letters 24(20):2515, DOI 10.1029/97GL02596

Severmann S, Mcmanus J, Berelson WM, Hammond DE (2010) The continental shelf benthic iron flux and its isotope composition. Geochimica et Cosmochimica Acta 74(14):3984–4004, DOI 10.1016/j.gca.2010.04.022, URL http://linkinghub.elsevier.com/retrieve/pii/S0016703710002073http://dx.doi.org/10.1016/j.gca.2010.04.022

Shaked Y, Kustka AB, Morel FMM (2005) A general kinetic model for iron acquisition by eukaryotic phytoplankton. Limnology and Oceanography 50(3):872–882, DOI 10.4319/lo.2005.50.3.0872, URL http://www.aslo.org/lo/toc/vol_50/issue_3/0872.html

Sholkovitz ER (1978) The flocculation of dissolved Fe, Mn, Al, Cu, Ni, Co and Cd during estuarine mixing. Earth and Planetary Science Letters 41(1):77–86, DOI 10.1016/0012-821X(78)90043-2

Siedlecki Sa, Mahadevan a, Archer DE (2012) Mechanism for export of sediment-derived iron in an upwelling regime. Geophysical Research Letters 39(November 2011):2–7, DOI 10.1029/2011GL050366

Sigman DM, Boyle EA (2000) Glacial/interglacial variations in atmospheric carbon dioxide. Nature 407(6806):859–869, DOI 10.1038/35038000

Simmons HL, Jayne SR, Laurent LCS, Weaver AJ (2004) Tidally driven mixing in a numerical model of the ocean general circulation. Ocean Modelling 6(3-4):245–263, DOI 10.1016/S1463-5003(03)00011-8, URL http://linkinghub.elsevier.com/retrieve/pii/S1463500303000118

Soetaert K, Middelburg JJ, Herman PMJ, Buis K (2000) On the coupling of benthic and pelagic biogeochemical models. Earth-Science Reviews

Somes C, Oschlies A, Schmittner A (2013) Isotopic constraints on the pre-industrial oceanic nitrogen budget. Biogeosciences 10(2):3121–3175, DOI 10.5194/bgd-10-3121-2013, URL http://www.biogeosciences-discuss.net/10/3121/2013/http://biogeosciences-discuss.net/10/3121/2013/bgd-10-3121-2013.pdf

Somes CJ, Schmittner A, Altabet Ma (2010) Nitrogen isotope simulations show the importance of atmospheric iron deposition for nitrogen fixation across the Pacific Ocean. Geophysical Research Letters 37(23):1–6, DOI 10.1029/2010GL044537, URL http://www.agu.org/pubs/crossref/2010/2010GL044537.shtml

Strzepek RF, Maldonado MT, Hunter Ka, Frew RD, Boyd PW (2011) Adaptive strategies by Southern Ocean phytoplankton to lessen iron limitation: Uptake of organically complexed iron and reduced cellular iron requirements. Limnology and Oceanography 56(6):1983–2002, DOI 10.4319/lo.2011.56.6.1983, URL http://www.aslo.org/lo/toc/vol_56/issue_6/1983.html

Strzepek RF, Hunter Ka, Frew RD, Harrison PJ, Boyd PW (2012) Iron-light interactions differ in Southern Ocean phytoplankton. Limnology and Oceanography 57(4):1182–1200, DOI 10.4319/lo.2012.57.4.1182, URL http://www.aslo.org/lo/toc/vol_57/issue_4/1182.html

Sunda WG, Huntsman SA (1997) Interrelated influence of iron, light and cell size on marine phytoplankton growth. Nature 2051(1977):1193–1197, URL http://lgmacweb.env.uea.ac.uk/green_ocean/publications/Colim/SundaHuntsman97.pdf

Syvitski JPM, Vörösmarty CJ, Kettner AJ, Green P (2005) Impact of humans on the flux of terrestrial sediment to the global coastal ocean. Science (New York, NY) 308(5720):376–380, DOI 10.1126/science.1109454

Tagliabue A, Völker C (2011) Towards accounting for dissolved iron speciation in global ocean models. Biogeosciences 8(2):3025–3039, DOI 10.5194/bg-8-3025-2011, URL http://www.biogeosciences-discuss.net/8/2775/2011/

Tagliabue A, Bopp L, Aumont O (2008) Ocean biogeochemistry exhibits contrasting responses to a large scale reduction in dust deposition. Biogeosciences 5(C):11–24, URL http://adsabs.harvard.edu/abs/2008BGeo....5...11Thttp://hal.archives-ouvertes.fr/hal-00330335/

Tagliabue A, Bopp L, Aumont O (2009a) Evaluating the importance of atmospheric and sedimentary iron sources to Southern Ocean biogeochemistry. Geophysical Research Letters 36(June):1–5, DOI 10.1029/2009GL038914

Tagliabue A, Bopp L, Aumont O, Arrigo KR (2009b) Influence of light and temperature on the marine iron cycle: From theoretical to global modeling. Global Biogeochemical Cycles 23(2):1–12, DOI 10.1029/2008GB003214, URL http://www.agu.org/pubs/crossref/2009/2008GB003214.shtml

Tagliabue A, Bopp L, Roche D, Bouttes N, Dutay JC, Alkama R, Kageyama M, Michel E, Paillard D (2009c) Quantifying the roles of ocean circulation and biogeochemistry in governing ocean carbon-13 and atmospheric carbon dioxide at the last glacial maximum. Climate of the Past 5:695–706, URL http://www.clim-past.net/5/695/2009/cp-5-695-2009.pdfhttp://www.clim-past.net/5/695/2009/cp-5-695-2009.html

Tagliabue A, Bopp L, Dutay JC, Bowie AR, Chever F, Jean-Baptiste P, Bucciarelli E, Lannuzel D, Remenyi T, Sarthou G, Aumont O, Gehlen M, Jeandel C (2010) Hydrothermal contribution to the oceanic dissolved iron inventory. Nature Geoscience 3(4):252–256, DOI 10.1038/ngeo818, URL http://www.nature.com/doifinder/10.1038/ngeo818

Tagliabue A, Mtshali T, Aumont O, Bowie AR, Klunder MB, Roychoudhury AN, Swart S (2012) A global compilation of dissolved iron measurements: focus on distributions and processes in the Southern Ocean. Biogeosciences 9(6):2333–2349, DOI 10.5194/bg-9-2333-2012, URL http://www.biogeosciences.net/9/2333/2012/

Tagliabue A, Aumont O, Bopp L (2014a) The impact of different external sources of iron on the global carbon cycle. Geophysical Research Letters 41:920–926, DOI 10.1002/2013GL059059, URL http://doi.wiley.com/10.1002/2013GL059059

Tagliabue A, Sallée J, Bowie A, Lévy M, Swart S, Boyd PW (2014b) Surface-water iron supplies in the Southern Ocean sustained by deep winter mixing. Nature Geoscience 7(March):1–7, DOI 10.1038/NGEO2101, URL http://www.nature.com/ngeo/journal/vaop/ncurrent/full/ngeo2101.html?WT.mc_id=TWT_NatureGeosci

Thullner M, Dale AW, Regnier P (2009) Global-scale quantification of mineralization pathways in marine sediments: A reaction-transport modeling approach. Geochemistry, Geophysics, Geosystems 10(10), DOI 10.1029/2009GC002484

Timmermans KR, Wagt BVD, de Baar HJW (2004) Growth rates, half saturation constants, and silicate, nitrate, and phosphate depletion in relation to iron availability of four large open-ocean diatoms from the Southern Ocean. Limnology and Oceanography 49(6):2141–2151, DOI 10.4319/lo.2004.49.6.2141, URL http://www.aslo.org/lo/toc/vol_49/issue_6/2141.html

Tsuda A, Takeda S, Saito H, Nishioka J, Nojiri Y, Kudo I, Kiyosawa H, Shiomoto A, Imai K, Ono T, Shimamoto A, Tsumune D, Yoshimura T, Aono T, Hinuma A, Kinugasa M, Suzuki K, Sohrin Y, Noiri Y, Tani H, Deguchi Y, Tsurushima N, Ogawa H, Fukami K, Kuma K, Saino T (2003) A mesoscale iron enrichment in the western subarctic Pacific induces a large centric diatom bloom. Science (New York, NY) 300(5621):958–61, DOI 10.1126/science.1082000, URL http://www.ncbi.nlm.nih.gov/pubmed/12738858

Twining BS, Baines SB (2013) The trace metal composition of marine phytoplankton. Annual review of marine science 5:191–215, DOI 10.1146/annurev-marine-121211-172322, URL http://www.ncbi.nlm.nih.gov/pubmed/22809181

US Dept of Commerce, National Oceanic and Atmospheric Administration, National Geophysical Data Center (2006) 2-minute Gridded Global Relief Data (ETOPO2v2). URL http://www.ngdc.noaa.gov/mgg/global/etopo2.html

VanCappellen P, Wang YF (1996) Cycling of iron and manganese in surface sediments: A general theory for the coupled transport and reaction of carbon, oxygen, nitrogen, sulfur, iron, and manganese. DOI 10.2475/ajs.296.3.197, URL <GotoISI>://A1996UC02400001

Vedamati J, Goepfert T, Moffett JW (2014) Iron speciation in the eastern tropical South Pacific oxygen minimum zone off Peru. Limnology and Oceanography 59(6):1945–1957, DOI 10.4319/lo.2014.59.6.1945, URL http://www.aslo.org/lo/toc/vol_59/issue_6/1945.html

Völker C, Tagliabue A (2014) Modeling organic iron-binding ligands in a three-dimensional biogeochemical ocean model. Marine Chemistry DOI 10.1016/j.marchem.2014.11.008, URL http://linkinghub.elsevier.com/retrieve/pii/S0304420314002229

Wallmann K (2010) Phosphorus imbalance in the global ocean? Global Biogeochemical Cycles 24(4):1–12, DOI 10.1029/2009GB003643, URL http://doi.wiley.com/10.1029/2009GB003643

Wang S, Bailey D, Lindsay K, Moore JK, Holland M (2014) Impact of sea ice on the marine iron cycle and phytoplankton productivity. Biogeosciences 11(17):4713–4731, DOI 10.5194/bg-11-4713-2014, URL http://www.biogeosciences.net/11/4713/2014/

Wang Y, Van Cappellen P (1996) A multicomponent reactive transport model of early diagenesis: Application to redox cycling in coastal marine sediments. Geochimica et Cosmochimica Acta 60(16):2993–3014, DOI 10.1016/0016-7037(96)00140-8

Weaver AJ, Eby M, Wiebe EC, Bitz CM, Duffy PB, Ewen TL, Fanning AF, Holland MM, MacFayden A, Damon Matthews H, Meissner KJ, Saenko O, Schmittner A, Wang H, Yoshimori M (2001) The UVic Earth System Climate Model: Model description, climatology, and applications to past, present and future climates. Atmosphere-Ocean 39(4):16, URL http://www.informaworld.com/index/929977676.pdfhttp://www.tandfonline.com/doi/full/10.1080/07055900.2001.9649686

Weber L (2006) Modelling the Speciation and Biogeochemistry of Iron in Oceanic Surface Waters at the Bermuda Atlantic Time-series Study site. PhD thesis, University of Southampton, URL http://eprints.soton.ac.uk/46002

Weber L, Völker C, Oschlies A, Burchard H (2007) Iron profiles and speciation of the upper water column at the Bermuda Atlantic Time-series Study site: a model based sensitivity study. Biogeosciences 4(4):689–706, DOI 10.5194/bg-4-689-2007, URL http://www.biogeosciences.net/4/689/2007/

Westberry T, Behrenfeld MJ, Siegel Da, Boss E (2008) Carbon-based primary productivity modeling with vertically resolved photoacclimation. Global Biogeochemical Cycles 22(2):n/a–n/a, DOI 10.1029/2007GB003078, URL http://doi.wiley.com/10.1029/2007GB003078

Westrich JT, Berner Ra (1984) The role of sedimentary organic matter in bacterial sulfate reduction: The G model tested. Limnology and Oceanography 29(2):236–249, DOI 10.4319/lo.1984.29.2.0236

Wetz M, Hales B, Chase Z, Wheeler P, Whitney M (2006) Riverine input of macronutrients, iron, and organic matter to the coastal ocean off Oregon, USA, during the winter. Limnol Oceanogr 51(5):2221–2231, URL http://ir.library.oregonstate.edu/xmlui/handle/1957/15021

Wu J, Boyle EA (2002) Iron in the Sargasso Sea: Implications for the processes controlling dissolved Fe distribution in the ocean. Global Biogeochemical Cycles 16(4):1–8, DOI 10.1029/2001GB001453

Wu J, Boyle E, Sunda W, Wen L (2001) Soluble and colloidal iron in the oligotrophic North Atlantic and North Pacific. Science 293(5531):847, URL http://www.sciencemag.org/content/293/5531/847.short

Zickfeld K, Eby M, Weaver AJ, Alexander K, Crespin E, Edwards NR, Eliseev AV, Feulner G, Fichefet T, Forest CE, Friedlingstein P, Goosse H, Holden PB, Joos F, Kawamiya M, Kicklighter D, Kienert H, Matsumoto K, Mokhov II, Monier E, Olsen SM, Pedersen JOP, Perrette M, Philippon-Berthier G, Ridgwell A, Schlosser A, Schneider Von Deimling T, Shaffer G, Sokolov A, Spahni R, Steinacher M, Tachiiri K, Tokos KS, Yoshimori M, Zeng N, Zhao F (2013) Long-Term Climate Change Commitment and Reversibility: An EMIC Intercomparison. Journal of Climate 26(16):5782–5809, DOI 10.1175/JCLI-D-12-00584.1, URL http://journals.ametsoc.org/doi/abs/10.1175/JCLI-D-12-00584.1

List of Figures

List of Tables

Acknowledgements - Danksagung

First of all I want to thank Andreas Oschlies for making this thesis with such an interesting topic possible, for the constant support, supervision, discussions and help, for giving me a lot of trust and freedom in my research, for making trips to conferences and summerschools possible and for being a very friendly chief.

I want to thank the whole working group "Biogeochemical Modeling" for the nice working atmosphere and being there when I had questions. In particular I would like to thank Julia Getzlaff and Lauren Zamora for being so friendly office mates, Wolfgang Köve for proofreading and Heiner Dietze for the technical help.

I also want to thank all the SFB PhD students and Postdocs for being such a nice group, Chris Schelten for organizing the SFB retreats and summerschool so perfectly and Monika Peschke for being so ready to help.

A special thanks goes to Yury Zablotski, Fabian Reith and Nadine Mengis for the nice lunch and coffee breaks, encouragement and the very good conversations.

I am very grateful for the enduring interest, support and proofreading of my girlfriend, my whole family and my friends.

Finally, I would simply like to thank everyone who supported me in writing this thesis.

Eidesstattliche Erklärung

Hiermit erkläre ich, dass die vorliegende Arbeit mit dem Titel: "*Modelling the marine biogeochemical implications of aeolian, sedimentary and riverine iron supply*" von mir selbstständig angefertigt wurde. Bis auf zitierte Referenzen und Beratung meiner Betreuer wurden keine weiteren Quellen verwendet. Diese Arbeit ist unter Einhaltung der Regeln guter wissenschaftlicher Praxis der Deutschen Forschungsgemeinschaft entstanden. Sie wurde weder im Rahmen eines Prüfungsverfahrens an anderer Stelle vorgelegt noch veröffentlicht. Ich erkläre mich einverstanden, dass diese Arbeit an die Bibliothek des GEOMAR und die Universitätsbibliothek der CAU weitergeleitet wird.

Kiel, den 09. Juni 2015

Levin Nickelsen